

**Ultrafast non-linear time-resolved spectroscopy:
Application to the structural study of polyatomic
molecules and clusters**

Dissertation
zur Erlangung des Doktorgrades der Naturwissenschaften

vorgelegt beim Fachbereich Chemie
der Johann Wolfgang Goethe – Universität
in Frankfurt am Main

von
Victor V. Matylitsky
aus Gresk

Frankfurt am Main 2004
(DF1)

Vom Fachbereich Chemische und Pharmazeutische Wissenschaften
der Johann Wolfgang Goethe-Universität als Dissertation angenommen.

Dekan: Prof. Dr. H. Schwalbe
Gutachter: PD. Dr. C. Riehn
Prof. Dr. B. Brutschy

Datum der Disputation: 23.09.2004

Маїм бацькам і сям'і
(To my Parents and Family)

Foreword

The work of this thesis has been carried out from December 2000 to July 2004 at the Institute of Physical and Theoretical Chemistry of the Johann Wolfgang Goethe University Frankfurt am Main in the research group of *Prof. B. Brutschy*.

I would like to thank everyone who contributed to this work.

To *PD Dr. Christoph Riehn* for being my *Doktorvater*, for his remarkable supervising and invaluable help in every stage of my PhD studies.

To *Prof. Dr. Bernhard Brutschy* for giving me the opportunity to work in his excellent research group. I gratefully acknowledge his contribution to and support of this work. His ideas gave inspiration to explore new aspects and applications of fs DFWM spectroscopy.

I thank my dear friend *Dr. Maxim Gelin* (Minsk, Belarus) for his excellent cooperation in various projects, continuous support in the spectral simulation theory and his optimism.

I am grateful to *Prof. Dr Włodzimierz Jarzēba* † (Krakow, Poland), for his help in the setting up the fs DFWM experiments. I grieve deeply for his sudden death from cancer.

I thank *Dr. Daniil Kosov* for our many discussion, which provided me with help and motivation, and for his worldly wisdom.

I am grateful to *Prof. Dr. Peter Hering* (Universität Düsseldorf) for lending a gas cell and introducing to the technology of heat pipes.

I am thankful for significant contributions to the development of the laser system, electronic and vacuum setup by the following people: *Dr. Andreas Weichert* for optimizing the laser system, *Dr. Alfred Steiger* and *Martin Engels* for their help with electronic devices of the experimental setup.

I am obliged to *Prof. Pavel Hobza* (Prague, Czech Republic), *Dr. P. Tarakeshwar* and *Prof. Kwang S. Kim* (Pohang, Korea) for support with *ab-initio* calculations, to *Prof. P. M. Felker* (UCLA, USA) for providing his RCS computer code.

Many thanks to the former and present members of the research group of prof. B. Brutschy for their help, advice and good working atmosphere. In particular, *Dr. Hans-Dieter Barth, Dr. Bernd Reimann, Dr. Michail Lebedev, Dr. Oliver Krauss, Nina Morgner, Sascha Vaupel, Michael Barashkov, Fuat Altunsu, Barbara Kirchner, Peter Richter.*

Finally, I would like to acknowledge my wife *Olga* and my son *Zhenya* for their love, care and support during these years.

Publications

Parts of this thesis have been or will be published in due course:

The structure of carboxylic acid dimers: results by time-resolved femtosecond degenerate four-wave mixing spectroscopy.

Matylitsky V. V., Gelin M. F., Riehn C. and Brutschy B.

In **“Femtochemistry and Femtobiology”** M. M. Martin and J. T. Hynes (Eds.), Elsevier, Amsterdam, (2004), 65-68.

The formic acid dimer (HCOOH)₂ probed by time-resolved structure selective spectroscopy.

Matylitsky V. V., Riehn C., Gelin M. F. and Brutschy B.

Journal of Chemical Physics (2003) 119(20), 10553-10562.

Cyclohexane Structure probed by Femtosecond Degenerate Four-Wave Mixing and Ab Initio Calculations.

Riehn C.; Matylitsky V. V.; Jarzeba W.; Brutschy B.; Tarakeshwar P.; Kim K. S.

Journal of American Chemical Society (2003) 125(52), 16455-16462.

The time domain fingerprints of a “perpendicular” rotational Raman band: Formic acid studied by femtosecond degenerate four-wave mixing.

Riehn C.; Matylitsky V. V.; Gelin M. F.

Journal of Raman Spectroscopy (2003), 34(12), 1045-1050.

Rotational recurrences in thermal ensembles of nonrigid molecules.

Gelin, M. F.; Riehn, C.; Matylitsky, V. V.; Brutschy, B.

Chemical Physics (2003), 290(2-3), 307-318.

Rotational coherence spectroscopy of jet-cooled molecules by femtosecond degenerate four-wave mixing: non-rigid symmetric and asymmetric tops.

Jarzeba, W.; Matylitsky, V. V.; Riehn, C.; Brutschy, B.

Chemical Physics Letters (2003), 368(5,6), 680-689.

Femtosecond degenerate four-wave mixing study of benzene in the gas phase.

Matylitsky, V. V.; Jarzeba, W.; Riehn, C.; Brutschy, B.

Journal of Raman Spectroscopy (2002), 33(11/12), 877-883.

Time-resolved rotational spectroscopy of para-difluorobenzene •Ar.
Weichert, A.; Riehn, C.; Matylitsky, V. V.; Jarzeba, W.; Brutschy, B.
Journal of Molecular Structure (2002), 612(2-3), 325-337.

Rotational coherence spectroscopy of benzene by femtosecond degenerate four-wave mixing.
Jarzeba, W.; Matylitsky, V. V.; Weichert, A.; Riehn, C.
Physical Chemistry Chemical Physics (2002), 4(3), 451-454.

Other publications:

New schemes and recent results for high-resolution rotational coherence spectroscopy with picosecond and femtosecond laser pulses.
Riehn C., Matylitsky V. V., Weichert A., Gelin M. F., Jarzeba W. and Brutschy B..
In “**Femtochemistry and Femtobiology**” M. M. Martin and J. T. Hynes (Eds.), Elsevier, Amsterdam, (2004), 73-76.

Depolarization of Luminescence of Polyatomic Molecules in the Gas Phase as a Method of Determining the Efficiency of Collisional Transfer of Angular Momentum.
Blokhin, A. P.; Gelin, M. F.; Kalosha, I. I.; Matylitskii, V. V.; Tolkachev, V. A.
Optics and Spectroscopy (Translation of Optika i Spektroskopiya) (2003), 95(1), 35-41.

Depolarization of fluorescence of polyatomic molecules in noble gas solvents.
Blokhin, A. P.; Gelin, M. F.; Kalosha, I. I.; Matylitsky, V. V.; Erohin, N. P.; Barashkov, M. V.; Tolkachev, V. A.
Chemical Physics (2001), 272(1), 69-76.

Presentations on Conferences

Conferences Talks

103. Bunsen-Tagung, May 2004, Dresden, Germany

Structural analysis of the equatorial and axial conformers of pyrrolidine from femtosecond degenerate four wave mixing spectroscopy

V. V. Matylitsky and C. Riehn

68. Physikertagung und AMOP – Frühjahrstagung, March 2004, Munich, Germany.

Study of the conformations of two-ring molecules in the gas phase - results by time-resolved femtosecond degenerate four-wave mixing

V. V. Matylitsky, C. Riehn, B. Brutschy

European Conference on Nonlinear Optical Spectroscopy (ECONOS 2003), April 2003, Besancon, France.

Rotational coherence spectroscopy by femtosecond degenerate four-wave mixing: non-rigid asymmetric top

V. V. Matylitsky, M. F. Gelin, W. Jarzeba, C. Riehn, B. Brutschy

European Conference on Nonlinear Optical Spectroscopy (ECONOS 2002), March 2002, Villigen, Switzerland.

Femtosecond Degenerate Four-Wave Mixing study of Benzene in the gas phase

V. V. Matylitsky, W. Jarzeba and C. Riehn

Poster Presentations

International Conference Femtochemistry VI, July 2003, Paris, France.

International Conference on Polarization Effects in Laser Spectroscopy and Optoelectronics. "PELS 2000", September 2000, Southampton, UK.

International Conference on Laser Optics for Young Scientists "LOYS-2000", July 2000, St. Petersburg, Russia.

International Conference on Optics "Optics' 99", October 1999, St. Petersburg, Russia.

Contents

CONTENTS	1
1 INTRODUCTION	4
2 THEORETICAL BACKGROUND	8
2.1 Rotation and rotational spectra	8
2.1.1 Diatomic and polyatomic linear molecules	9
2.1.2 Symmetric top molecules.....	10
2.1.3 Spherical top molecules	12
2.1.4 Asymmetric top molecules	12
2.1.5 Thermal population of rotational levels.....	13
2.1.6 Nuclear spin statistics	14
2.2 Rotational Coherence Effects	16
2.2.1 Quantum beats	17
2.2.2 Thermal averaging of rotational quantum beats	20
2.2.3 Characteristics of rotational coherence effects	21
2.2.4 Correction factors for asymmetric top molecules.....	26
2.2.5 Centrifugal distortion induced shifts of RRs periods.....	28
2.3 Experimental implementations	31
2.3.1 Pump-probe fluorescence depletion methods: TRFD, TRSEP, TRSRFD.....	32
2.3.2 Multiphoton ionization methods: (1+1') and (1+2') PPI, TRID	33
2.4 Coherent nonlinear methods	36
2.4.1 Raman-induced polarization spectroscopy (RIPS)	37
2.4.2 Time-resolved coherent anti-Stokes Raman scattering (CARS)	38
2.4.3 The degenerate four-wave mixing process	39
2.4.4 Simulation of the fs DFWM spectra	43
2.4.5 Characteristics of the rotational coherence recurrences obtained by fs DFWM ..	45
3 EXPERIMENTAL SETUP	49
3.1 Laser system	49
3.1.1 Femtosecond setup.....	50
3.1.2 Picosecond setup.....	51
3.2 Optical setups	52

3.3	Vacuum systems and signal detection.....	54
3.3.1	Molecular beam vacuum system.....	55
3.3.2	Vapor cell and heat-pipe	56
3.4	Timing, data acquisition, and control	57
4	NONRIGID SYMMETRIC TOP MOLECULES STUDIED BY FS DFWM	59
4.1	Introduction.....	59
4.2	Benzene and perdeutero-benzene.....	61
4.2.1	Benzene and perdeutero-benzene in a gas cell at room temperature	62
4.2.2	Benzene and perdeutero-benzene in a seeded supersonic jet	66
4.2.3	Influence of the centrifugal distortions	69
4.2.4	Dependence of fs DFWM spectra on laser intensity	71
4.3	Cyclohexane.....	74
4.3.1	Cyclohexane in a gas cell at room temperature and in a seeded supersonic jet ..	75
4.3.2	Comparison of the experimental results with ab-initio calculations.....	77
4.4	Conclusions.....	84
5	THE STRUCTURE OF ASYMMETRIC TOP MOLECULES IN THE GROUND AND ELECTRONICALLY EXCITED STATE	85
5.1	Introduction.....	85
5.2	Pyridine.....	86
5.2.1	Influence of asymmetry on fs DFWM spectra.....	86
5.2.2	Pyridine by fs DFWM in a gas cell at room temperature and in a seeded supersonic expansion.	88
5.3	para-Difluorobenzene.....	92
5.3.1	fs DFWM of para-Difluorobenzene, ground electronic state (S_0).....	92
5.3.2	(1+2') pump-probe photoionization of para-Difluorobenzene, electronically excited state (S_1)	97
5.4	Conclusions.....	100
6	MOLECULAR CLUSTERS STUDIED BY FS DFWM: CARBOXYLIC ACID DIMERS	101
6.1	Introduction.....	101
6.2	Formic acid monomer (HCOOH)	103
6.3	Formic acid dimer (HCOOH)₂	107
6.3.1	Early time response.....	108
6.3.2	Supersonic jet experiments	110

6.3.3	Geometry of the formic acid dimer (HCOOH) ₂	115
6.3.4	Isomeric structure of C-H...O/O...H-O type	118
6.4	Acetic acid (CH₃COOH)	120
6.4.1	Acetic acid (CH ₃ COOH) ₂ acid dimer in a supersonic jet	122
6.4.2	Acetic acid (CH ₃ COOH) ₂ and per-deuterated acetic acid (CD ₃ COOD) ₂ dimer in a gas cell	125
6.5	Conclusions.....	129
7	TWO-RING MOLECULES IN RCS.....	131
7.1	Introduction.....	131
7.2	Cyclohexylbenzene.....	132
7.2.1	RCS by (1+1') PPI of cyclohexylbenzene, electronically excited state (S ₁).....	133
7.2.2	RCS by fs DFWM of cyclohexylbenzene, ground electronic state	136
7.3	para-Cyclohexylaniline.....	139
7.3.1	RCS by fs DFWM of para-Cyclohexylaniline.....	140
7.4	Nicotine	143
7.4.1	RCS by fs DFWM of Nicotine	144
7.5	Conclusions.....	147
8	SUMMARY	148
	ZUSAMMENFASSUNG.....	152
	APPENDIX: ABBREVIATIONS AND SYMBOLS.....	157
	BIBLIOGRAPHY.....	158

Chapter 1

1 Introduction

The evaluation of accurate molecular structures has been one of the most enduring problems in contemporary chemistry [Pra98, DoH92, BGJ01]. Indeed, it has been said that a detailed understanding of molecular shapes explains virtually all of chemistry [Tri80, Woo78]. In this context, high-resolution spectroscopic methods have demonstrated their efficacy in determining the equilibrium geometries of many polyatomic systems both in the ground and excited states [Pra98]. One of the best-known and most powerful ways to obtain geometrical information on isolated molecular species is the spectroscopic investigation with rotational resolution. The number of molecular systems that have been studied at rotational resolution increased dramatically with development of the supersonic molecular beam technology, since it allows for vibrational and rotational cooling and makes the molecular line spectra easier to resolve and analyze [KaG51, PaT68, Ber82]. A wide range of high-resolution spectroscopic methods involving microwave radiation, far-infrared, infrared and optical lasers [FeI92 and refs. therein] is now available. All of these frequency-resolved techniques are based on the investigation of molecular eigenstates and the transitions between these levels stimulated by electromagnetic radiation. One of the problems of frequency-based spectroscopy, especially in dealing with large molecular species, is spectral congestion due to the fact that with increasing species size, the spacing between rotational levels decreases and becomes more difficult to resolve. The situation is becoming even more complicated for molecules with short-lived excited states, or with complicated spectra resulting from vibrational mode mixing. Under these circumstances a time-domain approaches becomes important [FeI92, FeZ95a, Rie02]. Over the past decades a new method, which is called *rotational coherence spectroscopy* (RCS) has been developed and put to application [FBZ86, CKS89, FeI92, FeZ95a, Rie02].

Nowadays, RCS is known as a powerful spectroscopic method for obtaining structural information on large isolated species in ground and electronically excited states [FeZ95a]. This method allows one to measure transient modulations known as rotational recurrences, which result from periodic changes in the orientational anisotropy of the sample due to the rotational motion of the molecules. The temporal periodicity of the recurrences is determined by the principal moments-of-inertia related to the rotational constants of the molecules being in study. RCS has a number of advantages for large molecular systems in comparison to frequency based spectroscopic methods. First, the recurrences associated with rotational coherence become easier to observe, the larger the species (the time separation is proportional to the moments-of-inertia). Second, RCS can be classified as a Doppler-free spectroscopic method. Third, the amplitudes of rotational coherence effects are not markedly sensitive to the partition function of the sample. Note that rotationally resolved resonances in the frequency-domain spectrum have intensities that scale inversely with the partition function – intensities decrease with increasing species size. Finally, different types of rotational coherence effects, i.e. different types of rotational recurrences provide information on different rotational constants. Moreover, the recurrences of one type are spaced equally in time, which simplifies analysis of experimental data [FeZ95a].

The growing interest into coherent nonlinear spectroscopic techniques (CARS, RIPS, fs DFWM) as an experimental implementation of RCS is based on several attractive features. First, these methods have a better time resolution, since femtosecond laser pulses are usually used. Second, a high signal to noise ratio can be achieved because these methods are zero-background techniques and a coherent laser emission is detected in an experiment [MPH93, JMW02]. Finally, these methods could be applied under various experimental conditions from a seeded molecular beam to combustions processes and flames [LMF01, LFM00].

The outline of the thesis is as follows. In *Chapter 2* a qualitative description of rotational coherence effects as Boltzmann-averaged quantum beats is given. The different experimental implementations that have been successfully used for rotational coherence spectroscopy are summarized in the Section 2.3. Special attention will be paid to coherent nonlinear experimental methods (Section 2.4), in particular to femtosecond degenerate four-wave mixing (fs DFWM), because the main results presented in this thesis were obtained with this technique. In order to obtain high-resolution structural data from fs DFWM spectra

of nonrigid asymmetric top molecules a new computer code has been developed* and subsequently incorporated into a nonlinear fitting routine. General aspects of the simulation and fitting procedures are described in Section 2.4.4. Moreover, a newly developed theoretical approach for calculation of centrifugal distortion induced corrections to the periods of rotational recurrences will be described.

Chapter 3 briefly describes the experimental setup, which was used during this work.

With the introduction of fs DFWM spectroscopy for the molecular species in the gas phase new perspectives for the structural study of isolated large molecules and molecular clusters by rotational coherence spectroscopy have been opened up [BZD99, FBG99, LMF01, Rie02]. Since, each new spectroscopic technique should be calibrated against model compounds of known structure and complexity the study of benzene (C_6H_6) and benzene- d_6 (C_6D_6) by fs DFWM was performed (see *Chapter 4*). These molecules are often utilized as molecular benchmark systems for high-resolution spectroscopy. For the first time the time-resolved fs DFWM technique was applied to the investigation of medium-sized molecules in a supersonic jet expansion. These experiments show the high potential of fs DFWM spectroscopy for the structural study of large molecules in the gas phase. Apart from that, the study of cyclohexane details the comparison of the experimentally determined rotational constants with that obtained from high-level *ab-initio* calculations, emphasizing vibrational zero-point averaging effects.

In *Chapter 5* the application of fs DFWM was extended to the investigation of nonrigid asymmetric top molecules, i.e., the aromatic systems: pyridine and *para*-difluorobenzene (*p*DFB). The rather complicated experimental spectra were successfully fitted by way of the newly developed fitting procedure, so that, structural information on these molecules was received and their complicated spectra could be assigned. The significance of these results is emphasized by the fact that the obtained molecular parameters of *p*DFB in the ground electronic state are one of the first results received by the high-resolution spectroscopic method.

In *Chapter 6* fs DFWM measurements of the first two members of the homologous group of carboxylic acids are reported. The investigation of formic and acetic acid vapor in a gas cell at room temperature and in a seeded supersonic jet at low temperature is presented. Besides

* The original computer code developed by P.M. Felker for the ground-state RCS transients for *rigid* asymmetric tops was modified.

the transients of the monomeric species spectral features, which originate from the dimeric species of the cyclic O-H...O/O...H-O type were obtained. Additionally, to the structural investigations of dimers formed by two strong hydrogen bonds of O-H...O type the method was applied to search for a second isomeric structure of the formic acid dimer with C-H...O and O...H-O hydrogen bonds. This investigation was stimulated by a theoretical prediction based on a population analysis [CVH02].

In the last part (*Chapter 7*) fs DFWM experimental results, for large two-ring molecules in a heat-pipe oven [ViC69, Vid96] at elevated temperature (>300K) are presented. The molecules, which have been studied in this chapter, are on the border of feasibility for the traditional frequency-based spectroscopies. Moreover they have a low vapor pressure at room temperature (<0.1 mbar), so that the measurement of the spectra reported in this chapter became only possible after introduction of a heat pipe oven into the fs DFWM experimental setup. These results open new perspectives for the RCS, in particular the fs DFWM technique, for the investigation of the large molecules (also biomolecules) with low vapor pressure. Additionally the conformational analysis of molecular species in equilibrium mixture can be performed.

In *Chapter 8* general conclusions are drawn.

Chapter 2

2 Theoretical Background

2.1 Rotation and rotational spectra

The *moment of inertia* of a rigid body about an axis is defined by

$$I = \sum_i m_i r_i^2 \quad (2.1)$$

where r_i is perpendicular distance of the mass element m_i from the axis.

There are three mutually perpendicular directions for which the moment of inertia is a maximum or a minimum. These directions are called the principal axes and the corresponding moments of inertia the principal moments of inertia [Her45].

The labeling scheme for the axes in a molecule is based upon the magnitude of the moments of inertia. The axes are labeled a , b and c with

$$I_A \leq I_B \leq I_C \quad (2.2)$$

so that I_C is always the largest moment of inertia and I_A is the smallest [Ber95].

(i) The case, when one principal moment of inertia is zero, or extremely small, while the other two are equal, is fulfilled for all linear molecules. (ii) If all three principal moments of inertia are equal it is called a spherical top. (iii) If two of principal moments of inertia are equal it is called symmetric top. There are two types of symmetric tops: prolate and oblate symmetric tops (see below). (iv) If for a molecule the three principal moments of inertia are different it is called an asymmetric top.

Thus, molecules can be classified on the basis of the values of the three principal moments of inertia.

$I_A = 0, I_B = I_C$ – linear molecule.

$I_A = I_B = I_C$ – spherical top.

$I_A < I_B = I_C$ – prolate symmetric top.

$I_A = I_B < I_C$ – oblate symmetric top.

$I_A < I_B < I_C$ – asymmetric top.

To characterize the deviation of molecular symmetry from the symmetric top limit one can use Ray's asymmetry parameter [Her45, Ber95].

$$\kappa = \frac{2B - A - C}{A - C} \quad (2.3)$$

If $0 < \kappa < 1$ or $-1 < \kappa < 0$ a species exhibits oblate or prolate top symmetry, respectively, and when $\kappa = 1$ a molecule is an oblate symmetric top, $\kappa = -1$ – prolate symmetric top. Here A, B, C are the rotational constants. In spectroscopy the rotational constants are usually given in MHz or cm^{-1} [Ber95].

For example the value of B is

$$B = \frac{h}{8\pi^2 I_B} \times 10^{-6} (\text{MHz}), \text{ or } B = \frac{h}{8\pi^2 c I_B} \times 10^{-2} (\text{cm}^{-1}). \quad (2.4)$$

2.1.1 Diatomic and polyatomic linear molecules

2.1.1.1 Rotational energy levels

Linear and diatomic molecules belong to the point groups $D_{\infty h}$ or $C_{\infty v}$, depending on whether or not they have a plane of symmetry perpendicular to the internuclear axis.

If the angular momentum of the electrons about the internuclear axis is zero, the molecule can be treated as if the moment of inertia about the internuclear axis is exactly equal to zero. It means that one can consider a simple nonrigid rotator, for which the energy levels are given by:

$$F(J) = BJ(J+1) - DJ^2(J+1)^2 \quad (2.5)$$

where $F(J)$ is the rotational term value, J is the rotational quantum number, B, D are the rotational and centrifugal distortion (CD) constants, respectively.

Since the atoms in a molecule experience a centrifugal force, due to the rotational motion the internuclear positions are changed. The term $DJ^2(J+1)^2$ in equation 2.5 represents the influence of this centrifugal force.

In diatomic molecules the constant D is related to the rotational constant B and the vibrational frequency ω (assuming the harmonic oscillator approximation) by the simple formula [Her45]

$$D = \frac{4B^3}{\omega^2} \quad (2.6)$$

From the Eq. 2.6 one can see that D is directly related to the bond strength between atoms in a diatomic molecule.

2.1.1.2 Rotational Raman spectrum.

A prerequisite for the Raman effect is that the polarizability in a fixed direction changes during a molecular motion. Thus diatomic and linear polyatomic molecules of point group $D_{\infty h}$ or $C_{\infty v}$ always exhibit rotational Raman spectra. The selection rules for the rotational Raman transitions for linear and diatomic molecules are $\Delta J = 0, \pm 2$.

Substituting $J' = J''+2 = J+2$ into Eq. 2.5, one obtains for the wave-number shifts for diatomic and linear molecules

$$|\Delta \nu| = F(J') - F(J'') = (4B - 6D)(J + \frac{3}{2}) - 8D(J + \frac{3}{2})^3 \quad (2.7)$$

In fact only S-branch transitions are observable since $\Delta J = 0$ transitions correspond to the unshifted Rayleigh line. And the definition of the S-branch as $\Delta J = J' - J''$ means that both the Stokes and anti-Stokes transitions are S-branch lines [Ber95].

2.1.2 Symmetric top molecules

2.1.2.1 Rotational energy levels

In diatomic or linear molecule, the angular momentum vector L due to rotation of the molecule lies along the axis of rotation. In a prolate symmetric top the rotational angular

momentum vector L need not to be perpendicular to the top axis (see Fig. 2.1), but has in general a constant component L_z in the direction of the figure axis.

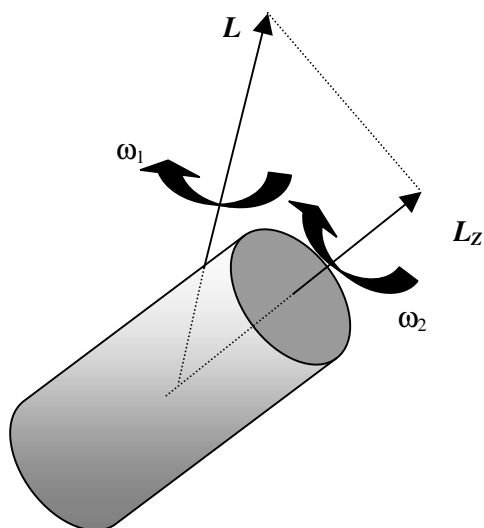


Fig. 2.1 Motion of the instantaneous axis of rotation and of the figure axis for a symmetric top.

Thus, a prolate symmetric top rotates (or nutates) about the axis of L and additionally rotates about the z -axis. The vector L_z represents the magnitude and direction of the angular momentum due to this motion. The solution of the Schrödinger equation for this system gives the term values for a nonrigid prolate symmetric top

$$F(J,K) = BJ(J+1) + (A-B)K^2 - D_J J^2(J+1)^2 - D_{JK} J(J+1)K^2 - D_K K^4 \quad (2.8)$$

Where $B = h/8\pi^2 cI_B$ and $A = h/8\pi^2 cI_A$ are rotational and D_J, D_{JK}, D_K are CD constants.

The quantum number K can adopt values $0, \pm 1, \pm 2, \dots, \pm J$. The fact that K cannot be greater than J follows from the fact that magnitude of the vector L_z cannot be greater than that of L . For oblate symmetric tops Eq. 2.8 is also valid after exchanging the rotational constants A and C .

2.1.2.2 Rotational Raman spectrum

As for the momental ellipsoid, so also for the polarizability ellipsoid the rule holds that an axis of symmetry coincides with one of its axes. That means that the polarizability ellipsoid is a rotational ellipsoid. In this case, a rotation about the figure axis, classically, is not connected with change of the induced dipole moment and therefore, quantum theoretically, a change of K cannot be produced by light scattering.

Thus we obtain the selection rules: $\Delta J = 0, \pm 1, \pm 2$; $\Delta K = 0$. When these selection rules for a Raman transition are applied to the energy levels of Eq. 2.8, two series of lines, the R and S branches, are obtained, [Her45] with displacements

$$\begin{aligned} |\Delta\nu| &= F(J+1, K) - F(J, K) = \\ &= 2B(J+1) - 2D_{JK}K^2(J+1) - 4D_J(J+1)^3, \quad J, K = 1, 2, \dots \end{aligned} \quad (2.9)$$

$$\begin{aligned} |\Delta\nu| &= F(J+2, K) - F(J, K) = \\ &= (4B - 6D_J)(J + 3/2) - 4D_{JK}K^2(J + 3/2) - 8D_J(J + 3/2)^3, \quad J, K = 0, 1, \dots \end{aligned} \quad (2.10)$$

where $\Delta J = \pm 1$ does not appear for $K = 0$.

2.1.3 Spherical top molecules

The energy levels for spherical top ($I_A = I_B = I_C$) molecules can be obtained from the expression for energy levels of symmetric top (Eq. 2.8) by assuming $A = B$

$$F(J) = BJ(J+1) - DJ^2(J+1)^2 \quad (2.11)$$

The energy depends only on J and in exactly in the same way as for linear molecules.

Since, for any rotation of the spherical rotor the induced dipole moment remains unchanged no rotational Raman spectrum appears.

2.1.4 Asymmetric top molecules

There are no closed formulae for the energy levels terms of asymmetric tops for arbitrary rotational quantum number J , like in the cases of linear and symmetric top molecules (Eqs. 2.5, 2.8). That is, the Schrödinger equation for the asymmetric top molecules has no analytical solution and therefore has to be solved numerically. Let us introduce the basis of the symmetric top eigenfunctions $|J, K, M\rangle$. Here the standard quantum notation is used: $J(J+1)$ is the eigenvalue of the square of the angular momentum, K and M are, respectively, the eigenvalues of the projection of the angular momentum on the z-axis of the molecular and the laboratory frame. Then the nonzero matrix elements of the rigid asymmetric top Hamiltonian, $\langle J_1 K_1 M_1 | \hat{H} | J_2 K_2 M_2 \rangle \equiv \delta_{J_1 J_2} \delta_{M_1 M_2} H_{K_1 K_2}^J$, read

$$H_{KK}^J = \{(A+B)[J(J+1) - K^2] + 2CK^2\}/2, \quad (2.12)$$

$$H_{KK+2}^J = (A-B)\sqrt{(J+K+2)(J+K+1)(J-K-1)(J-K)}/4.$$

While writing down formulas (2.12), the explicit assumption was made that the axis c of the largest moment of inertia was used as the quantization axis. By cyclic permutation of rotational constants A , B , and C one can readily obtain analogous expressions in the case of A and B quantization axes. In order to obtain eigenvalues and eigenfunctions of the asymmetric top molecule, the tridiagonal matrix with elements (2.12) has to be diagonalized numerically. For Raman transitions, the selection rules $|J - J'| \leq 1$ and $|J - J'| \leq 2$, respectively, must be obeyed, as in case of symmetric top molecules.

2.1.5 Thermal population of rotational levels

The thermal population of rotational levels of symmetric top species is defined by the Boltzmann distribution and can be written in the following form [Her45]

$$N_{J,K} \propto g_{J,K} \exp\left(-\frac{F(J,K)}{kT}\right) \quad (2.13)$$

where $g_{J,K}$ is the statistical weight, k the Boltzmann constant and T the absolute temperature. The values of $F(J,K)$ can be calculated from Eqs 2.5, 2.8, 2.11 for the different types of rotors. Due to the degeneracy of the rotational energy on the quantum number M , the factor $g_{J,K}$ is proportional to $2J+1$.

For example, the rotational energy levels of a symmetric top molecule are $(2J+1)$ -fold degenerate for $K = 0$ and $2(2J+1)$ -fold degenerate for $K \neq 0$. Coefficient 2 appears since the rotational states with K and $-K$ have the same energy. Linear molecules ($K = 0$) have a $(2J+1)$ degeneracy and the rotational states of spherical tops (energy levels independent of K) are $(2J+1)^2$ -fold degenerate.

In order to calculate the thermal population of the rotational levels of asymmetric top molecules one can use Eq. 2.13 with the eigenvalues obtained by the procedure described in section 2.1.4. with $2J+1$ degeneracy on the quantum number M . The K -type double degeneracy is removed in passing from the symmetric to asymmetric top, since there is no

longer a direction in the molecule along of which the rotational angular momentum vector L (see section 2.1.2.1) has a constant component [Her45].

The degeneracy also depends on the nuclear spin statistics (see the following Section 2.1.6).

2.1.6 Nuclear spin statistics

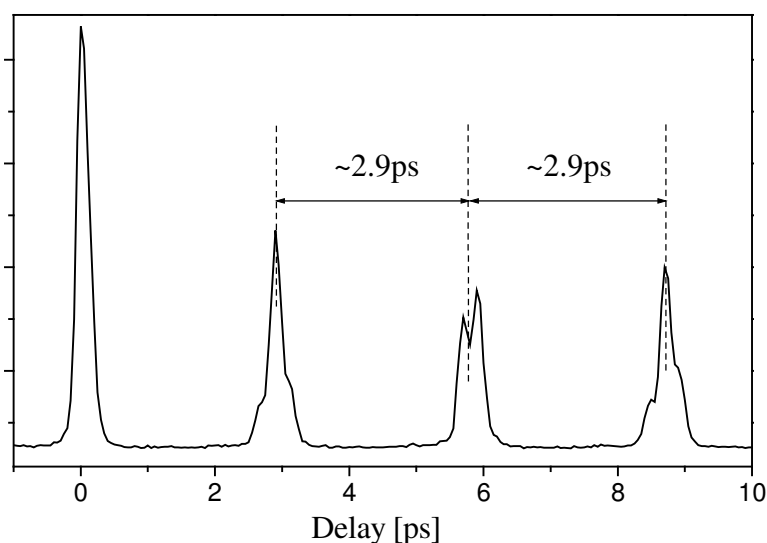


Fig. 2.2 Experimental fs DFWM spectrum of oxygen $^{16}\text{O}_2$.
Example of nuclear spin statistic weighting effect for the rotational states.

The selective occupation of rotational states that stems from the Pauli principle is termed *nuclear spin statistics*. Nuclear spin statistics must be taken into account whenever a rotation interchanges equivalent nuclei [Atk94]. To illustrate this statement, let us consider the fs DFWM of O_2 . Fig. 2.2 shows first 10 ps of the experimental fs DFWM spectrum of oxygen $^{16}\text{O}_2$ at room temperature. There are three rotational transients with temporal separation $\Delta t \sim 2.9\text{ps}$, and using the simple equation for determination of the rotational constant B from time-resolved RCS spectra one can get $B = 1/4\Delta t \approx 86\text{GHz}$. The obtained value of constant B is twice larger than well known rotational constant for oxygen ($B \approx 43.101\text{ GHz}$ see Refs. [Her45, JoL75]).

This effect can be rationalized by the influence of the nuclear spin statistics on the rotational level population. In the case of O_2 only every second rotational level is occupied. An

increase of the spacing between the rotational levels in the frequency domain leads to a decrease of the spacing in the time domain.

The explanation for the missing rotational states is given by the Pauli principle and the fact that O nuclei are bosons (spin = 0). Therefore, when the O₂ molecule is rotated by 180°, the two identical O nuclei are interchanged, but the overall wavefunction of the molecule must remain unchanged. From another side, the rotational wavefunctions change sign by $(-1)^J$ under such motion [Atk94]. Hence only the odd rotational levels are permissible for O₂.

However, for polyatomic molecules the consideration of the nuclear spin statistic weighting factor for the rotational levels is not so simple as in the case of O₂ and it is beyond of the scope of this work.

2.2 Rotational Coherence Effects

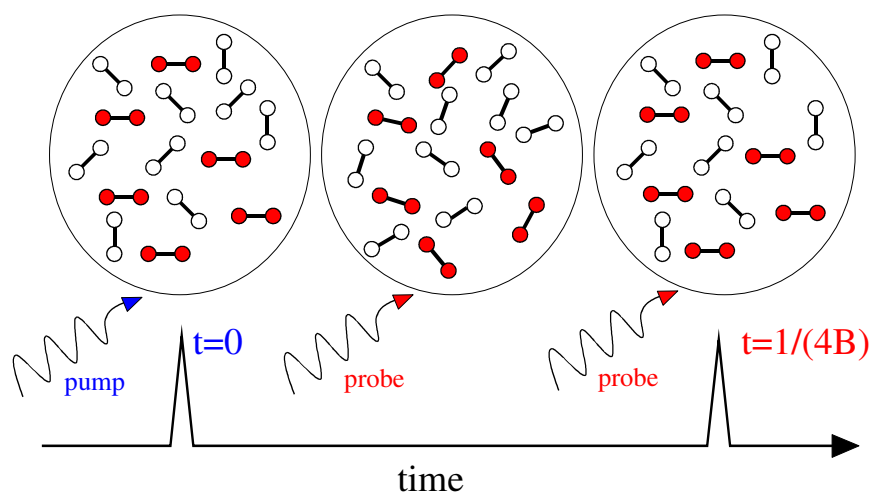


Fig. 2.3 Illustration of the probing of molecular rotation in real-time. A sample is excited with a linearly polarized pulse of light (the pump pulse), and examined by the probe pulse.

In the previous Sections it was shown that there are quantum numbers associated with the rotational motion of isolated species. The fact that the rotational frequencies are proportional to the rotational quantum numbers, permits the formation of rotational superposition states – *rotational coherences* – whose evolution is periodic rather than dissipative [FeZ95a]. The undamped rotational motion of free gaseous species gives possibility to monitor the superposition states in the time domain. Heritage et al. have experimentally demonstrated this for the first time for the CS_2 molecule in 1975. The modulations of the molecular refractive index have been attributed to the time evolution of a coherent sum of rotational superposition states [HGL75]. Bashkin et al. have applied the effect of rotational coherence to the investigation of the large molecule stilbene [BFZ86]. The observable signals from such experiments exhibit recurrences known as rotational coherence effects. The observation and characterization of rotational coherence effects is called “Rotational coherence spectroscopy” (RCS) [FeZ95a].

The principle of the technique is as follows (see Fig. 2.3). A polarized ultrashort pulse (the pump pulse) creates at zero-time an orientational anisotropy in the sample. This anisotropy appears due to the preferential interaction with those species whose transition dipoles (in case of the resonant RCS) or the polarizability tensor (nonresonant methods: RIPS, DFWM)

have large components along the pump laser beam polarization vector. This induced alignment in the ensemble of molecules decays on the picosecond time scale, but, due to the quantized nature of free rotation, rephases fully or partially again at a time determined by the rotational constants of the molecules.

Evolution of the anisotropy in the pump-probe experiments is monitored by the second laser pulse (the probe pulse) and observation of alignment rephasing in RCS can be accomplished by a number of different probe methods. All of these methods have three features in common. First, they involve monitoring spectroscopic transitions of the species that have interacted with the pump pulse. Second the monitored transitions reflect the alignment of these species. Third, the transitions are monitored as a function of time, on the picosecond time scale [Fel92 and refs. therein.]. The RCS spectrum is depicted schematically on the bottom of Fig. 2.3. The initial anisotropy at $t = 0$ rephases at regular intervals due to the periodic nature of free rotation and quantization of the rotational angular momentum. The experimental RCS spectra carry information about molecular parameters (the rotational and CD constants, transition dipole moment direction in the molecular frame or the traceless polarizability tensor), and experimental parameters (polarization direction and temperature) [FeZ87, Fel92, Dan01].

2.2.1 Quantum beats

The above-considered description is a useful picture of RCS experiment. However, a quantitative treatment of RCS requires a consideration of the quantum mechanics involved. RCS is based on the quantum beat phenomenon, a time-domain manifestation of quantum interference. To understand the nature of RCS one has first to consider the principles of quantum beat spectroscopy. Fig. 2.4a shows energy-level diagram, which depicts the simplest, two state quantum-beat experiment.

A short pulse of light, a pump pulse, simultaneously excites a molecule from the ground-state level $|g\rangle$ to two or more excited states that can combine in absorption with $|g\rangle$. The coherent excitation of the levels can be achieved if the spectral bandwidth $\Delta\nu = a/\Delta T$ of the pump laser pulse is bigger than the frequency separation of the energy levels. The constant a depends on the pulse profile $I_p(t)$.

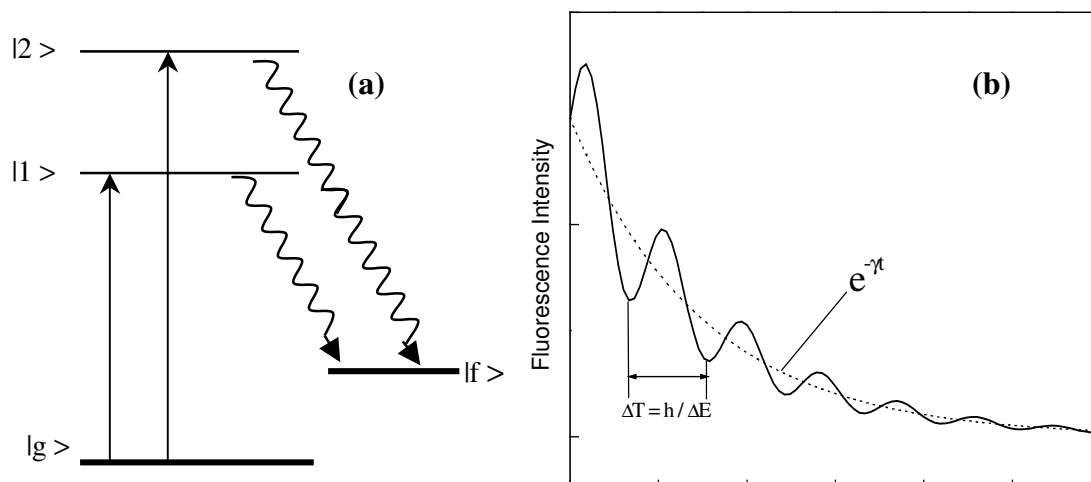


Fig.2.4 (a) Energy-level diagram, illustrating a quantum beat experiment; (b) Oscillating of the fluorescence exponential decay. The period of oscillation corresponds to the energy difference ΔE between excited levels.

The time-resolved total fluorescence intensity emitted from these coherently prepared levels shows a modulated exponential decay. To simplify the consideration, one can consider the case, when the two levels $|k\rangle$, $k=1,2$ are coherently excited. The excited state prepared by the pump pulse at $t = 0$ can be written as a linear superposition of the sublevel functions and is given by

$$|\psi(0)\rangle = C_1|1\rangle + C_2|2\rangle \quad (2.14)$$

where C_k , are coefficients, that represent the probability amplitudes of the transition from ground-state level $|g\rangle$ to excited levels $|k\rangle$. Because of the spontaneous transition into a final state $|f\rangle$ the excited state evolves as a function of time t . The evolution of the wave function $|\Psi(t)\rangle$ is given by the Schrödinger equation

$$|\Psi(t)\rangle = (C_1|1\rangle \exp[-i\frac{E_1 t}{\hbar}] + C_2|2\rangle \exp[-i\frac{E_2 t}{\hbar}]) e^{-\frac{\gamma}{2}t} \quad (2.15)$$

where γ is decay constant of the excited levels $|k\rangle$, $k=1,2$. (for simplification $\gamma = \gamma_1 = \gamma_2$), and E_k is the energy of $|k\rangle$. The damping of the modulation is given by the radiative lifetime of the excited states.

The prepared excited state is monitored by a probe pulse, that produces a signal $I(t)$, which corresponds to the transition probability from the excited levels $|k\rangle$ to the common final state $|f\rangle$.

Then the probability of this transition can be written as

$$I(t) = (A + B \cos(\omega_{21}t))e^{-\gamma t}, \quad (2.16)$$

A, B being numerical factors and

$$\omega_{21} = \frac{E_2 - E_1}{\hbar}. \quad (2.17)$$

If the probability of the transitions $|k\rangle \rightarrow |f\rangle$, $k=1,2$ is nonzero, then the observed signal reveals a modulation of the exponential decay (see Fig. 2.4(b)), with the frequency ω_{21} . From measurement of the modulation frequency one can determine the energy separation of the two levels, even if their splitting is below the Doppler width. Quantum beats (QBs) therefore allow for Doppler-free resolution. It is necessary to emphasize the conditions under which QBs occur. Beats only arise between eigenstates that first, can be excited from the same initial state $|g\rangle$ and second, can combine with the same final state $|f\rangle$ [Dem96, FeZ95a].

The physical interpretation of the quantum beat is based on the following effect. One cannot distinguish between transitions $|k\rangle \rightarrow |f\rangle$, $k=1,2$ if the total fluorescence is monitored. It is possible to say, that these two levels share the same photons, and the consequence is interference between the radiation from them. This quantum beat interference effect can be compared with Young's double slit interference experiment [Zar71]. For the fluorescence system in Fig. 2.4(a) the levels $|1\rangle, |2\rangle$ are analogues of the two identical slits in Young's experiment. The lifetimes of the states corresponding to the two levels can be compared with width of the slits in Young's experiment [Dem96, Hol98].

The situation depicted on Fig 2.4 is the simplest of cases. In general, there are N eigenstates that can be excited from the same initial state $|g\rangle$ and second, can combine with the same final state $|f\rangle$. That means that in a general case Eq. 2.16 will be transformed to the sum of $N(N-1)/2$ damped cosine terms. With the frequencies $\omega_{ij} = (E_i - E_j)/\hbar$, which are directly proportional to the energy differences between $N(N-1)/2$ distinct pairs of N eigenstates.

Different types of QBs have already been observed. Observation of QBs arising from the coherent excitation of fine structure levels, hyperfine structure levels, Zeeman levels [Har76, Zar71, BiH92] and arising from singlet-triplet electronic levels [BiH92, CGM81] and vibrational [FeZ88] coupling have been reported in literature.

2.2.2 Thermal averaging of rotational quantum beats

A special type of the generic quantum beats considered above is rotational QBs. In that case, the eigenstates are coherently prepared by the pump pulse in the rotational manifold of a single rovibronic state. Rotational selection rules allow for the excitation of more than one rotational level from any given initial rovibronic state. Similarly, the selection rules allow for combination of all transition from the excited eigenstates to a common final rovibronic state. Hence all necessary requirements for the rotational QBs to appear are fulfilled.

The situation depicted in Fig.2.4 and considered in section 2.2.1 has to be extended for the rotational quantum beats experiments involving thermal ensembles of molecular species, because many different initial rotational states of molecular system are populated, even at very low rotational temperature in the supersonic jet expansion. Upon pulse excitation different initial states give rise to different rotational superposition states. Therefore, in a rotational QBs experiments the signal contains contributions from many different excited superposition states, with different frequencies [FeI92, FeZ87, BFZ87]. In this case, the signal observed in experiment is the sum of a large number of beat terms with various frequencies ω_j . The Eq. 2.16 could be transformed for a resonant RCS signal to

$$I(t) \propto [A + \sum_j \alpha_j \cos(\omega_j t)] e^{-\gamma t} \quad (2.18)$$

where the α_j are constants that depend on rotational quantum numbers, temperature, and polarization scheme of experiment.

The summation of a big number of cosine modulation having random frequencies and amplitudes will wash out the of rotational QBs due to destructive interference. However, this does not occur in practice, because the frequencies and amplitudes do not vary randomly with the rotational numbers of initial states. Moreover it has been shown both theoretically [FeI92, FeZ87, FeZ95a,b] and experimentally [BFZ87, BaZ89, JCO92, Rie02]

that the manifestation of rotational coherence does not disappear in the simple case of symmetric top molecules and also not for asymmetric top species. The point is that the rotational frequencies are integer multipliers of certain fundamental frequencies, so that Eq. 2.18 is quasiperiodic. For example, Eq. 2.18 for rigid linear molecules is written as

$$I(t) = \sum_{J=0}^{\infty} N_J X(J, t) \quad (2.19)$$

Here

$$X(J, t) = a_1(J) + a_2(J) \cos\{4\pi B(2J-1)t\} + a_3(J) \cos\{4\pi B(2J+3)t\}$$

$$a_1(J) = \frac{J(J+1)}{(2J-1)(2J+3)}, \quad a_2(J) = \frac{3J(J-1)}{2(2J-1)(2J+1)}, \quad a_3(J) = \frac{3(J+1)(J+2)}{2(2J+1)(2J+3)} \quad (2.20)$$

Evidently, Eq. (2.19) is periodic with the period $1/4B$.

2.2.3 Characteristics of rotational coherence effects

In order to simplify the description, the characteristics of the rotational coherence effects are considered by example of the resonant time-resolved fluorescence depletion (TRFD) technique in this chapter. The characteristics of the rotational recurrences (RRs) obtained by the nonlinear coherent methods (fs DFWM CARS etc.) will be given later in Section 2.4.5. There are several types of rotational coherence recurrences, which appear in RCS spectra. A detailed classification and derivation of the formulas have been reported in the literature [JCO92, FeZ95a]. However, several points should be emphasized here about RR and the information, which can be extracted from RCS spectra. First, the types of transients that occur in a RCS trace are determined primarily by the transition dipole moment directions associated with the pump and probe processes or in the case of the coherent nonlinear techniques by the polarizability tensor. Second, more than one type of recurrences can be presented in a given spectra, which provide information on different rotational constants [RMG03, Rie02, CCH90]. Third, rotational coherence effects exist even for highly asymmetric top molecules. Of course this point is a very important one in regard to the general applicability of RCS [JCO92, Rie02, MRG03]. And finally, as shown for the first time by experiments on I_2 at room temperature by Gruebele et al. [GRD90], CD effects RCS transients. Later, it has been investigated in a series of publications for small molecules

[FBG00, FBG99, FML02] and also in the contributions from our group for larger species [MJR02, JMR03, MRG03]. Here, a short consideration of the types of RRs will be given and the requirements for their appearance, first, for symmetric top molecules. Second, a summary concerning the effects of asymmetry on the rotational coherence effect will be presented.

2.2.3.1 Symmetric tops

It is reasonable to start the classification of the RRs of rigid near-symmetric top species, whose rotational energies are given by Eq. (2.8) with CD-terms omitted. To date, five types of RRs from RCS spectra of near-symmetric top molecules have been observed. They were denoted as “*J-type*”, “*K-Type*”, “*hybrid*” transients and so-called asymmetry transients of “*A- and C-types*” [JCO92].

a. J-type transients

J-type transients appear from rotational QBs between states whose J (symmetric top quantum number which gives the total rotational angular momentum) values differ but whose K (gives angular momentum along the top axis) values remain unchanged ($\Delta J=1,2$; $\Delta K=0$). This type of recurrences can appear in case of any direction of the pump and probe transition dipoles. And upon thermal averaging this class of beats will produce transients at $t(n) \approx n/2(B+C)$ for prolatelike and at $t(n) \approx n/2(A+B)$ for oblatelike symmetric species (see Table 2.1). These transients have different polarities and the even recurrences at $t \sim (A+B)^{-1}$ are generally larger in amplitude than odd recurrences at $t \sim [2(A+B)]^{-1}$. A schematic depiction of the J-type recurrences one can see on Fig. 2.5.

b. K-type transients

K-type transients appear due to rotational QBs between states having the same J quantum number but K quantum numbers are differed by 2 ($\Delta J=0$, $\Delta K=2$). Second requirement is that excitation and probe dipoles each have a component perpendicular to symmetric top axis. If both conditions are valid one can expect the K-type recurrences at time $t \sim |4C - 2(A+B)|^{-1}$ in a case of an oblate symmetric top and $t \sim [(4A - 2(B+C))]^{-1}$ for a prolate symmetric top. All of these recurrences have the same polarity (see Fig 2.5).

Table 2.1: Characteristics of rotational coherence transients. Adapted from Ref. [Fel92]. o:oblate, p: prolate. Transient polarity given for TRFD experiment. (pump, probe) transition dipole moment; for (\perp ,H) also (H, \perp) is valid.

Transient type	top symmetry	Recurrence time $t(n) \approx n/\dots$	Transient polarity	Transition dipole moment	contributing coherences
J	P	$2(B+C)$	+, -, +, -,...	all cases	$ \Delta J =1,2;$ $\Delta K=0$
	O	$2(A+B)$			
K	P	$4A-2(B+C)$	-, -, -, ...	$(\perp,\perp), (\perp,H), (H,H)$	$\Delta J=0,$ $ \Delta K =2$
	O	$ 4C-2(A+B) $			
H (hybrid)	P	$2A-(B+C)$	+, -, +, -,...	(H,H)	$\Delta J=0,$ $ \Delta K =1$
	O	$ 2C-(A+B) $			
A	P	$4A$	not regular	$(\perp,\perp), (\perp,H), (H,H)$	$\Delta J=2,$
C	O	$4C$	not regular		$\Delta K=2$
A asymmetry	O	$4A$	not regular	all cases	$\Delta J=2$
C asymmetry	P	$4C$	not regular		$\Delta K=0,$

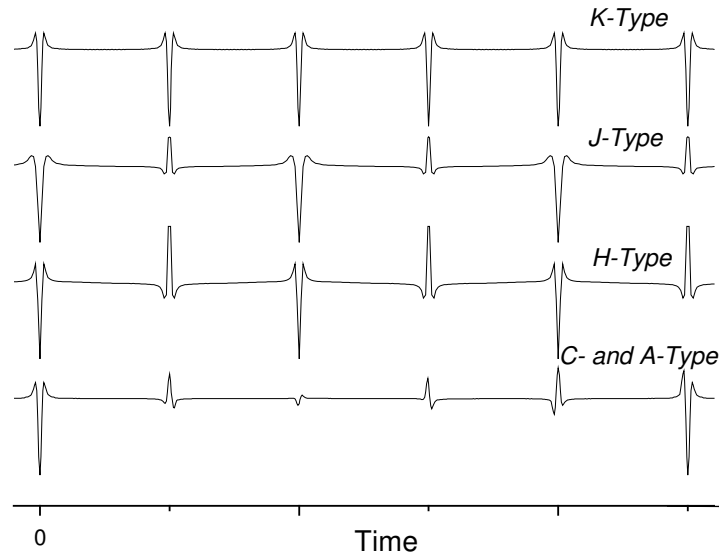


Fig. 2.5 Schematic depiction of the different types of RRs. The absolute polarities depicted refer to a time-resolved fluorescence depletion (TRFD) scheme in which pump and probe pulses have the same linear polarization.

c. Hybrid transients

If the transition dipole moment has a component both in the direction of the top axis and perpendicular to it when hybrid-type (H-type) transient could appear. H-type transients are due to rotational QBs between eigenstates with the same J quantum number and with K

differ by unit ($\Delta J=0$, $|\Delta K|=1$). Hybrid type features appear at a temporal separation twice of those of K-type recurrences with alternating polarity (see Table 2.1 and Fig. 2.5).

d. Asymmetry transients (A- and C-types) in RCS traces of symmetric top molecules

The requirements for the appearance of asymmetry transients in RCS traces of asymmetric tops will be considered in following section. However, the asymmetry transients can also arise for symmetric top molecules. For example, C-type recurrences can appear in a RCS spectrum of an oblate symmetric top molecule, if this molecule has both transition dipoles with perpendicular component to the main symmetry axis (c -axis). For a prolate symmetric top species the main symmetry axis is the a -axis. And A-type transients can appear for b and c -axis polarized transitions of prolate top molecules. If the above considered requirements are realized in an experiment, one can expect C-type transients at temporal positions $t(n)=n/4C$ for the oblate symmetric tops and A-type at $t(n)=n/4A$ in the case of the prolate symmetric tops. Both types of transients exhibit ill-defined polarity with dispersion and absorptionlike line shapes and modulated amplitudes [JCO92, FeZ95a]. Fig. 2.5 (bottom trace) shows an example of line shapes of asymmetry transients in which the first transient is absorptionlike with negative polarity, the second is mostly absorptionlike with positive polarity and the third is dispersionlike.

2.2.3.2 Asymmetric top molecules

Asymmetric top molecules are not rigorously characterized by fundamental rotational frequencies. Because of this, one may wonder about the existence of rotational QBs for these molecules at all. But it has been clearly shown that J-, K-, and hybrid-type transients all persist in RCS spectra of asymmetric top molecules, albeit with reduced magnitude. The reason for this is that significant patches of the rotational-level structure in asymmetric top retain symmetric top regularity [JCO92, CCJ90, BaZ89, FeZ87, BFZ87]. Even more, it has been shown that extra features begin to appear in RCS spectra of asymmetric top molecules as one departs from the symmetric limit [FeZ87, BFZ87]. These features have been called “A-type” and “C-type” transients or “*asymmetric*”. They are arising from the same frequency of rotational QBs, and have equal temporal positions like the ones considered in

section 2.2.3.1d., but their requirement with respect to the transition dipole moment is different. For example, the RCS spectrum of oblatelike molecules (Ray's asymmetry parameter $0 < \kappa < 1$) with the transition dipole moment along the main symmetric c -axis could exhibit A-type transients. Also, rotational QBs of prolatelike species ($-1 < \kappa < 0$) with the transition dipole moments along the a -axis give C-type transients. A further complication arises in the case of asymmetric tops having transitions polarized along the b principal axis. In particular, both A-type and C-type transients can be present for prolatelike and oblatelike species in this case. It should also be noted that C-type and/or A-type transients could be present in RCS traces of species that have transition dipole moment directions different from any of the principal axis direction, i.e. in case of hybrid transitions. The characteristics of all types rotational coherence effects are summarized in Table 2.1 and in Fig. 2.5. The detailed theoretical consideration of rotational coherence effects for asymmetric top molecules has been given in literature [JCO92, FeZ95a].

A new kind of transients (*P-type transients*) for planar molecules have been predicted from a theory based on a semiclassical approach for RRs in thermal ensembles of asymmetric top molecules by Gelin et al. P-type transients obey the same requirements for appearance as the C-type transients. Moreover, if a molecule is planar [$I_A + I_B = I_C$, $C = AB/(A+B)$] the periods of P- and C- recurrences are identically the same. In this case, these transients differ only by their polarity [GTB00]. Thus, up to now the P-type transients have not been assigned in the experimental spectra. However, they appear in the simulated spectra of Ref. [JCO92], (e.g., Figs 3b,c, 5, 6, and 8 of this paper) [GTB00].

In summary, the following effects of molecular asymmetry on rotational coherence can be tabulated. First, one generally expects RCS transients in asymmetric tops to be broader with smaller intensities than their counterparts in the symmetric top limit. Second, the intensity of the transients will decay faster with time, the further a species departs from the symmetric top limit [FeZ87, BFZ87]. And a last trend, J-, K- and H-type transient temporal positions will be not exactly equal to positions given in Table 2.1, and will be a complicated function of the principal rotational constants of the species. Therefore, accurate extraction of spectroscopic parameters of the molecule from the RCS measurements on asymmetric tops will generally require the complete fitting of the observed trace to a simulated one, with inclusion of CD effects where it is necessary (fs DFWM). Some considerations of the

corrections for the rotational recurrence periods due to the asymmetry of molecules and CD will be presented in the following two Sections 2.2.4 and 2.2.5.

2.2.4 Correction factors for asymmetric top molecules

Since asymmetry shifts rotational levels away from the regular spacing seen in the symmetric top, determination of the expected RRs periods is no longer trivial. In fact, the simple formula for the RRs periods of J-, K-, H- type of transients for symmetric top species (Table 2.1) is not correct for asymmetric top molecules. In the Refs. [FeZ95a, BaZ89] the authors are giving approximate expressions for calculation of RRs periods for asymmetric top molecules. To derive approximate expressions for RRs periods of the asymmetric top species one must start with the rotational energies. For low values of J , it is possible to represent the energies of an asymmetric rigid rotor in power series expansions in $J(J+1)$ and the asymmetry parameters $b_o = \frac{A-B}{2C-A-B}$ for near-oblate top symmetry molecules, and

$b_p = \frac{C-B}{2A-B-C}$ for molecules with prolate symmetry [Pol57, BaZ89]. The parameters b_o

and b_p are zero in oblate or prolate symmetric limit, respectively. The term, which is linear with b , will affect the recurrence amplitudes but has little effect on the RRs periods. Therefore, the b^2 terms are the first terms capable of causing a deviation from the expressions for symmetric top rotors. The derivation of the approximately corrected formulas based on expansion terms up to b^2 is given in the literature [BaZ89, FeZ95a].

Table.2.2: The expressions for the rotational recurrences periods of the J-, K-, H- types transients corrected for the asymmetric top species.

Transients type	Near-oblate top	Near-prolate top
J	$t_n \geq n / [2(A+B) + (2C-A-B)b_o^2]$	$t_n \leq n / [2(B+C) + (2A-B-C)b_p^2]$
K	$t_n \geq n / [4C-2A-2B)(1-b_o^2/2)]$	$t_n \geq n / [4A-2B-2C)(1-b_p^2/2)]$
H	$t_n \geq n / [2C-A-B)(1-b_o^2/2)]$	$t_n \geq n / [2A-B-C)(1-b_p^2/2)]$
	$b_o = \frac{A-B}{2C-A-B}$	$b_p = \frac{C-B}{2A-B-C}$

These formulas are collected in Table 2.2. It is necessary to note, that first, here the inequality is used, because their validity is decreasing with asymmetry increasing. Second, this type of corrections is not necessary for asymmetric transients, i.e., A- and C-

recurrences [FeZ95a]. The different inequality signs in the time spacing formulas for the J-recurrences (Table 2.2) show an increase of the period of the J-type transients for oblate asymmetric tops and a decrease of that for prolate asymmetric tops in parallel with enhancement of molecular asymmetry.

Other expressions for calculations of the corrected RRs periods of asymmetric rigid molecules have been reported in literature [GTB00]. Here the authors used a semiclassical approach to derive “exact” non-perturbative expressions for the periods of the J-, H-, and K-type transients. These formulas are given in the following: [GTB00]

$$t_o^J = [4(C + \sqrt{(A-C)(B-C)})]^{-1} \quad t_p^J = [4(A + \sqrt{(A-C)(A-B)})]^{-1}$$

$$t_o^H = [\sqrt{(A-C)(B-C)} + (A+B)/2 - C]^{-1} \quad t_p^H = [\sqrt{(A-C)(A-B)} + A - (B+C)/2]^{-1} \quad (2.21)$$

If the molecules under consideration are nearly oblate and prolate tops, one than can expand the above expressions in the Tailor series on the small parameter $(A-B)$ for oblate and $(B-C)$ for prolate tops:

$$t_o^J = [2(A+B) - 4\Gamma^O + O\{(A-B)^3\}]^{-1}$$

$$t_p^J = [2(B+C) + 4\Gamma^P + O\{(B-C)^3\}]^{-1} \quad (2.22)$$

for the J-type transients of near-oblate and near-prolate symmetric tops, respectively. And

$$t_o^H = [A+B-2C - \Gamma^O + O\{(A-B)^3\}]^{-1}$$

$$t_p^H = [2A-B-C - \Gamma^P + O\{(B-C)^3\}]^{-1} \quad (2.23)$$

for the H-type transients. The RRs periods of K-type transients are twice shorter than RRs periods of H-recurrences. And it is possible to disregard the contributions of these corrections. The values of Γ^O and Γ^P can be calculated from the following expressions:

$$\Gamma^O \equiv (A-B)^2 / [8(A-C)] \geq 0$$

$$\Gamma^P \equiv (B-C)^2 / [8(A-C)] \geq 0 \quad (2.24)$$

As a result, the formulas 2.21-2.24 as well as the expressions summarized in Table 2.2 lead to an increase of the J-type RRs periods for oblate asymmetric tops and a decrease for

prolate asymmetric tops. The asymmetry enlarges the period of the K- and H- type transients, irrespective of the type of molecular top [GTB00, BaZ89, FeZ95a].

2.2.5 Centrifugal distortion induced shifts of RRs periods

It is well known that CD affects the RRs periods [Rie02, MJR02, Dan01]. Thus, before complete fitting analysis, it is desirable to estimate how the CDs constant are changing RRs periods. In addition, this effect is interesting from theoretical side, because the CD-terms produce system frequencies, which are nonlinear with rotational quantum numbers and, thereof destroy periodic dynamics peculiar to the rigid rotor.

Changing of the RRs periods due to CD effect have been estimated for linear rotors and symmetric top species.

2.2.5.1 Linear rotor

For the linear rotors the modified RRs period can be calculated as: [GRM03]

$$\tau = \tau_0(1 + \delta) \quad (2.25)$$

where τ_0 is the uncorrected “fundamental” RRs period $\tau_0 = 1/4B$, (B is the rotational constant of the linear molecule), and δ the correction to the period. With assumption $B/\bar{T} \ll 1$, which holds for molecules even in a supersonic jet, ($T \sim 5K$) one can get

$$\delta = 4D\bar{T}/B^2 = 64D\bar{T}\tau_0^2 \quad (2.26)$$

where D is the CD constant (see Eqs. 2.5 and 2.6), $\bar{T} \equiv k_B T / h$, T is the temperature (\bar{T} [GHz]=20.835833T[K]), and k_B is the Boltzmann constant.

According to Eq. (2.26), the correction to the period, δ , is proportional to the temperature. This is in an accord with the experimentally confirmed observation that the CD-induced contribution increases with temperature [Rie02, MJR02, JMR03]. In addition, equations 2.25, 2.26 allows one to estimate the CD constant, provided the RCS periods are measured at two different temperatures. For example, if the RR periods are available in a cell (τ_{cell}) at a room temperature (T_{cell}) and in a supersonic jet ($\tau_{jet} \cong \tau_0, T_{jet} \ll T_{cell}$) one can estimate

$$D = \frac{(\tau_{cell} - \tau_{jet})}{64\overline{T}_{cell}\tau_{jet}^3} \quad (2.27)$$

Several assumptions have been adopted during the derivation of Eqs. (2.25, 2.26), therefore, the validity of these equations has to be considered. From comparison of present theory and simulation one can see that the simple linear formula (2.25) works for the first few RRs $n \leq 10$. Strictly speaking, the corrections for the RR periods must be n -dependent, so that $\delta \rightarrow \delta_n$. Only for the first few RRs the n -independence of δ is valid. That means that if one wishes to calculate a CD constant from the experimental RCS spectrum, one should use the first few RR positions for the linear regression analysis, which are n -independent. Also the temperature has to be not too high, and the CD constant should be small enough [GRM03].

2.2.5.2 Symmetric tops

The CD correction formulas have also been obtained for symmetric top molecules. In particular, correction was derived for three types of the transients: J, K, H-transients.

J-transients ($|\Delta J|=1,2; \Delta K=0$).

To calculate the modified RRs periods following expressions can be used

$$\tau^J = \tau_0^J (1 + \xi^J), \quad \tau_0^J = 1 / (4B), \quad \xi^J = \frac{\overline{T}}{B^2} (\lambda_j^J(s) D_j + \lambda_{jk}^J(s) D_{jk}), \quad (2.28)$$

$$\lambda_j^J(s) = 1 - 3s + 12/(3-s), \quad \lambda_{jk}^J(s) = -(1+3s)/2 + 4/(3-s).$$

Here the dimensionless parameter

$$-1 \leq s \leq 1 - B/C \leq 1 \quad (2.29)$$

has been introduced, which specifies the entire family of symmetric tops, from prolate ($s > 0$) to oblate ($s < 0$). $s = -1$ corresponds to a planar symmetric top, $s = 0$ does to a spherical top, and $s = 1$ does to a linear rotor.

The CD constants D_j and D_{jk} enter Eq. (2.28) with different, rotational constant-dependent weights $\lambda_j^J(s)$ and $\lambda_{jk}^J(s)$. If D_j and D_{jk} are of the opposite signs (this is so, e.g., for a number of polyatomic molecules) one can expect cancellation effects in the CD-induced

corrections. As expected, the CD constant D_k does not contribute to ξ^J . This effect has been shown for the RRs periods of benzene measured by the fs DFWM method [MJR02].

K-transients ($\Delta J = 0$, $\Delta K = \pm 2$).

The CD correction for K-transients can be written:

$$\tau^K = \tau_0^K (1 + \xi^K), \quad \tau_0^K = \frac{1}{4|B-C|}, \quad \xi^K = \frac{\bar{T}}{C(C-B)} (\lambda_k^K(s)D_k + \lambda_{jk}^K(s)D_{jk}), \quad (2.30)$$

$$\lambda_k^K(s) = 3, \quad \lambda_{jk}^K(s) = 1.5 + 1/(1-s).$$

In contrast to case of the J-type RRs the CD corrections for the K-transients depend on the centrifugal distortion constant D_k , moreover $\lambda_k^K(s) > \lambda_{jk}^K(s)$ if $-1 \leq s < 1/3$. The opposite is correct if $1/3 < s \leq 1$. This means that the influence of D_k is more important than that of D_{jk} for oblate and slightly prolate molecules, but the situation changes for highly prolate molecules.

H-transients ($\Delta J = 0$, $\Delta K = \pm 1$).

This type of transients does not need a separate investigation. It is evident from the above presentation that the corrections for H-type transients are described by the expressions (2.30) for K-transients, in which one should merely substitute $\tau_0^K \rightarrow \tau_0^H \equiv 2\tau_0^K$ (the rigid-body period of the H-type transients is twice longer than that for K-ones [Fel92, FeZ95a]). The H-transients, as distinct from K-ones, are sign-alternating [GRM03]. How this approach can be applied to the interpretation of actual experimental data will be demonstrated in the experimental part of this thesis.

2.3 Experimental implementations

A variety of spectroscopic methods is currently available for the implementation of RCS in the structural studies of large species in the ground and the electronically excited states. Most of them have the following common features. First of all, all of them are time-resolved methods with a picosecond resolution or better. Second, the below considered implementations of RCS, except time-correlated single-photon counting, are pump-probe methods. The principle of the pump-probe method has been considered at the beginning of this section and visualized in Fig.2.3. Third, in all RCS implementations linearly polarized pump and probe pulses are used. And fourth, they have a sensitivity that is high enough to investigate species in seeded supersonic molecular beams, but the application of some of these methods is not limited to species in a supersonic jet [GrZ93, Dan01, Rie02]. The differences between these RCS methods lie in their technical realization and in the information provided on the studied species (Table 2.3).

Table 2.3 Comparison of different experimental RCS implementations.

Implementation	Describ. in this work	laser pulses (colors)	Time resolution	state ^{a)}	Mass selective
TCSPC		1 (1)	30 ps	e	
TRFD	x	2 (1)	laser lim. ^{b)}	g, e	
TRSEP	x	2 (2)	laser lim.	e	
TRSRFD	x	2 (2)	laser lim.	g	
PPI	x	2 (2)	laser lim.	e	x
TRID	x	3 (2)	laser lim.	g, e	x
TRPES		2 (2)	laser lim.	e	
RIPS	x	2 (1)	laser lim.	g	
CARS	x	3 (2)	laser lim.	g, e	
DFWM	x	3 (1)	laser lim.	g	

^{a)} g: ground state, e: electronically excited state

^{b)} Limited by the laser pulse duration.

It is possible to divide the RCS implementations in two groups. First, there are resonant “*noncoherent*” methods for RCS registration; most of these methods are based on the detection of *incoherent* signals, such as fluorescence or multiphoton ionization. Second, there are “*coherent*” nonlinear techniques, where the coherent signal (e.g. laser radiation) is detected. In this chapter the main resonant methods will be presented. Since the main

experimental results, considered in this thesis, have been obtained by non-resonant method (fs DFWM), this RCS implementation will be considered separately and described in more detail in Section 2.4.

2.3.1 Pump-probe fluorescence depletion methods: TRFD, TRSEP, TRSRFD

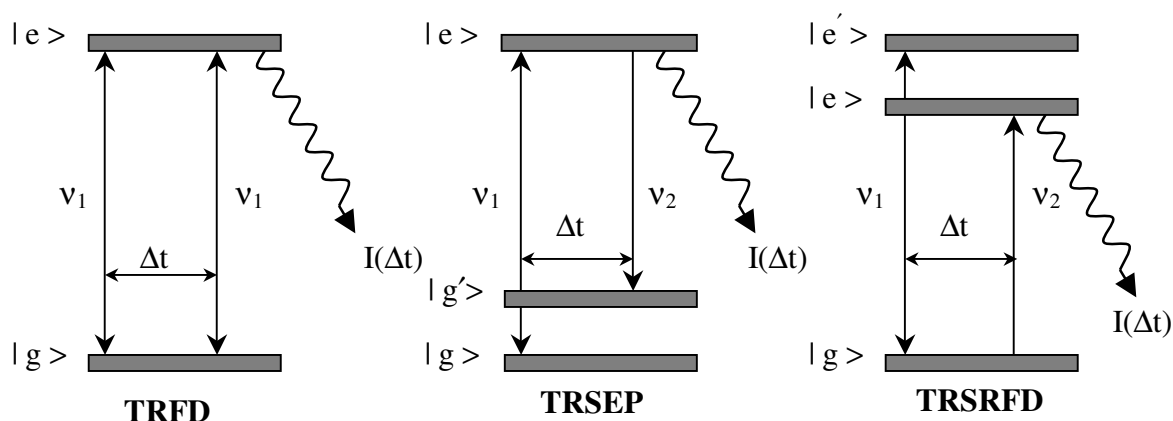


Fig. 2.6 Fluorescence depletion methods: TRFD, TRSEP, TRSRFD.

One of the most widely used method of obtaining a RCS spectrum employing a pump-probe technique is time-resolved fluorescence depletion (TRFD). TRFD was developed by McDonald and coworkers [CKS89, KCS89]. In TRFD (Fig. 2.6) the pump and probe laser pulses have the same wavelength ν_1 , which is tuned to a vibronic resonance of the molecule of interest. The total fluorescence intensity from $|e\rangle$ is monitored as a function of the time delay between pump and probe pulses (with identical energy, wavelength and polarization), and rotational coherence results in dips or peaks of a fluorescence background. The RCS spectra obtained by TRFD exhibit RRs from the ground as well as from the excited states [HCF91, Rie02]. That could cause complications in terms of assignment and evaluation of the transients [RWL00].

This method has some very attractive features in regard to RCS. First, the time resolution of TRFD is limited only by the laser pulse width, as it is pump-probe method. Second, the method is relatively simple due to the fact that only one tunable laser is necessary. Disadvantages of this method are that it can be applied only to species with reasonable

fluorescence quantum yields, and second, TRFD is a depletion spectroscopy, thus the rotational coherence transients appear as small modulations on a fluorescence background [Fel92].

There are two picosecond schemes, which can be considered as a two-color modification of TRFD. Those are time-resolved stimulated emission pumping (TRSEP) [CKS89, KCS89, CCH90] and time-resolved stimulated Raman-induced fluorescence depletion [CCH90, HCF91] (TRSRFD) (Fig.2.6). In TRSEP the probe pulse ν_2 is redshifted in wavelength relative to the pump pulse ν_1 so that only transitions into vibrational states $|g'\rangle$ of the electronic ground level are possible. The RRs from the electronically excited state $|e\rangle$ are detected in the RCS spectra, since only the stimulated emission from the electronically excited state $|e\rangle$ is observed.

In TRSRFD the polarized pump pulse ν_1 is resonant with a vibronic transition originating in the vibronic ground state $|g\rangle$. The probe pulse induces a transition from $|g\rangle$ to states (denoted as $|e'\rangle$) in the rotational manifold of a second excited vibronic state. The total fluorescence measured versus pump-probe delay time exhibits rotational coherence transients which arise from resonant stimulated rotational Raman process at delays reflecting ground-state rotational constants.

The main advantage of the latter two methods in comparison with TRFD is that one can measure the rotational constants of the species under study in the electronically excited and ground state separately.

2.3.2 Multiphoton ionization methods: (1+1') and (1+2') PPI, TRID

The first pump-probe version of RCS was demonstrated by Scherer et al. [SKR87]. In this contribution the authors have presented measurements of the rotational constants in the excited (S_1) state of *trans*-stilbene by implementation of picosecond pump-probe multiphoton ionization mass spectrometry in RCS. The scheme depicted in Fig.2.7b has been used for the measurements. Here the linearly polarized picosecond pump pulse ν_1 is used to coherently prepare rotational levels of the species in excited state $|e\rangle$. The second pulse ν_2 , delayed in time, probes the initially formed coherence by absorption from $|e\rangle$ to a highly excited electronic level $|e'\rangle$ with subsequent ionization. The probe wavelength is

adjusted to ensure a resonant transition between $|e\rangle \rightarrow |e'\rangle$. The dependence of the photoion signal vs. pump-probe delay is monitored. This particular scheme of RCS is named (1+2') pump-probe photoionization (PPI).

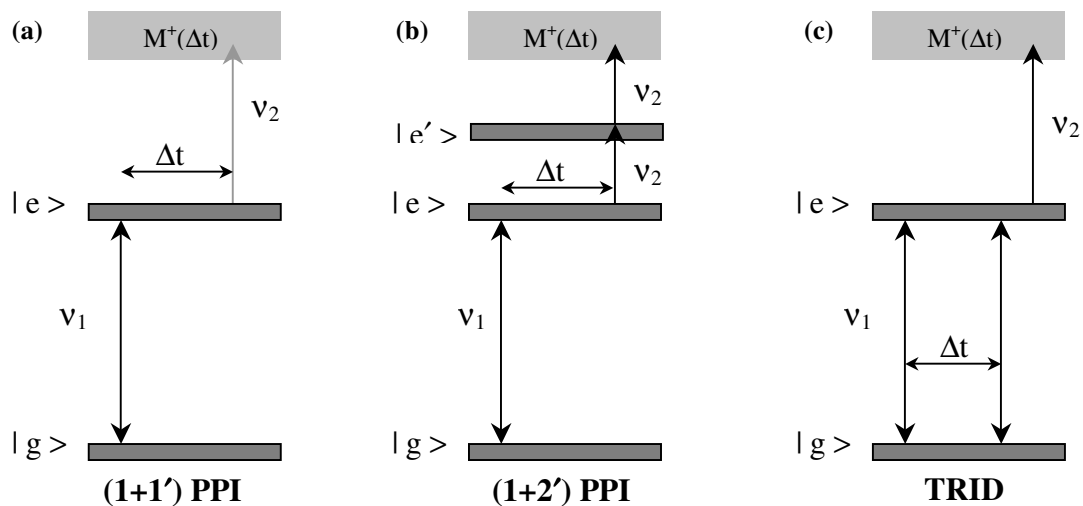


Fig. 2.7 Multiphoton ionization methods: (1+1') and (1+2') PPI, TRID.

PPI methods share the advantage of a mass-selective detection scheme when they are coupled, for instance, with a time-of-light mass spectrometer. In general, species with a very weak fluorescence quantum yield could be investigated by PPI methods. The resonant steps in these schemes are particularly helpful for the investigation of supersonic expansions where usually a distribution of clusters is present, since specific cluster structures can be selected by their 'UV fingerprints' in the excitation (pump) step and subsequently ionized (probe) non-resonantly. However, these methods deliver only transients and rotational constants related to the electronically excited state [Rie02].

Ohline and coworkers have proposed another three-photon ionization scheme, named time-resolved ionization depletion (TRID) (see Fig. 2.7c) [ORF93]. Here following a TRFD scheme, a third ionizing laser pulse was applied in order to probe the population of the excited state. TRID is based on the same principles as the time-resolved fluorescence depletion scheme with the only difference in the mode of detection. Thus, TRID has all advantages of TRFD, in addition a photoion detection scheme is implemented. This method has been applied in investigations of the fluorene monomer and the naphthalene trimer [ORF93, BGF99].

In our laboratory it has been shown that the application of a simpler two photon $(1+1')$ PPI scheme (Fig. 2.7a) is also possible for RCS investigation of species in the electronically excited state [RWB00, WRB01a, WRM02]. The observation of RCS transients in this scheme is remarkable since up to these measurements it was thought that simple $(1+1')$ PPI scheme should not be suitable for RCS experiments [FeZ95a, SKR87]. Moreover, other experiments with a similar scheme did not deliver any result [ORF93]. The crucial point for the explanation of these results was the fact that probe transitions to the “ionization continuum” are not clearly defined with respect to their final states. In particular, the cation can be generated in different rovibronic states with the departing electron carrying different amounts of energy. Moreover, different amounts of angular momentum can be imparted on the leaving electron so that the selection rules with respect to angular momentum are relaxed and possible RCS features are obscured. However, also from a theoretical analysis, the detection of RCS by $(1+1')$ PPI was not ruled out completely [FeZ95b,c]. So, this fact and our experimental results disprove the above supposition. The $(1+1')$ PPI scheme gives information about the rotational constants of the species in the electronically excited state as well as all PPI methods, described above.

2.4 Coherent nonlinear methods

Up to now only resonant methods for the RCS registration have been discussed. Most of these methods are based on the detection of incoherent signals, such as fluorescence or ion current (see Section 2.3). However, the application of coherent nonlinear techniques for the investigation of freely rotating molecules was theoretically analyzed some time ago [LHG71, MyH86, HCF91]. With the development of new powerful femtosecond (fs) laser systems, the third- or higher-order nonlinear techniques have been employed for studying molecular dynamics in the gas phase. In the first pioneering work of Heritage et al. [HGL75], the rotational QBs of CS₂ vapour have been observed utilizing picosecond laser pulses. The rotational coherence in gaseous oxygen, nitrogen and carbon dioxide was studied with fs resolution by Raman-induced polarization spectroscopy (RIPS) [MPH93, MPL95], which is analogous to the technique used in Ref. [HGL75]. Hayden and Chandler used fs time-resolved coherent Raman techniques to excite and monitor the evolution of the vibrational coherence of benzene and 1,3,5-hexatriene in the gas phase [HaC95]. Three femtosecond laser pulses at different wavelengths were used in the experiments. The signal of interest in these experiments was the coherent light that is Stokes or anti-Stokes shifted from the near UV probe pulse. Later, fs coherent anti-Stokes Raman scattering (CARS) and fs degenerate four-wave mixing (fs DFWM) were applied in order to investigate the evolution of the vibrational coherence in the ground and electronically excited states of iodine [SKM97a,b]. Nowadays coherent nonlinear methods are widely used for the study of the different types of molecular dynamics and for laser control of chemical reactivity [MPZ96, BZD99, FBG00, LMF01, Rie02, Dan01 and refs. therein]

In the following sections a short review of different nonlinear coherent methods (RIPS, CARS) will be given. The theoretical description of the degenerate four-wave mixing process and the simulation procedure of the RCS spectra obtained by fs DFWM will be considered in the sections 2.4.3-2.4.5.

2.4.1 Raman-induced polarization spectroscopy (RIPS)

In RIPS experiments, the rotational superposition state is prepared through nonresonant stimulated Raman excitation by a linearly polarized femtosecond pump pulse. The energy diagram for the RIPS is shown in Fig 2.8a. A molecule in level $|g\rangle$ can be excited into a virtual state and then stimulated back into different levels $|g'\rangle$ or $|g''\rangle$, by the same pump photon. This stimulated Raman process creates coherently excited states in the ground rovibronic manifold. In RIPS, the time evolution of the molecular alignment is probed through coherent interaction of the sample with a delayed probe pulse.

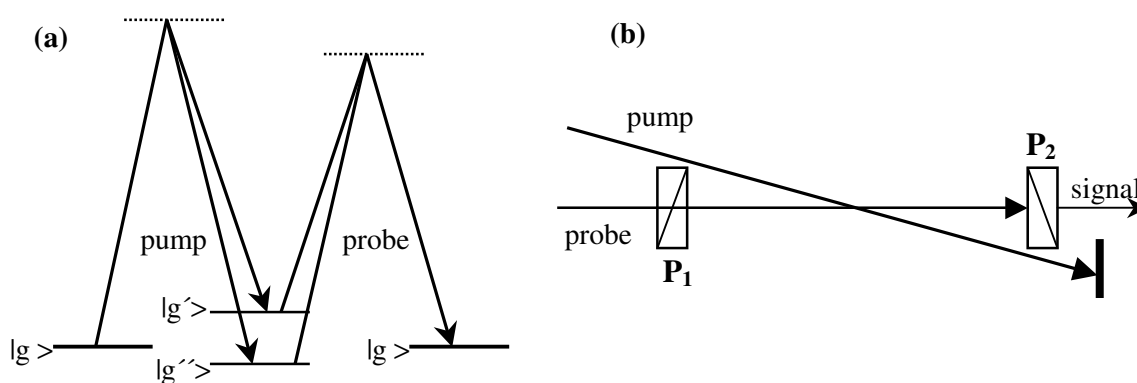


Fig. 2.8 (a) Energy level diagram for RIPS. (b) Optical setup used in the RIPS experiments.

The pump and probe beams, derived from a fs laser (usually the pump beam is more intense) are crossed in the cell at small angle. The probe laser, polarized at 45° with respect to the polarization plane of the pump laser, passes through two perpendicularly aligned polarizers P_1 and P_2 (see Fig. 2.8b) placed before and after the cell. After the cell the pump beam is blocked. The part of the probe beam (signal), which is transmitted through the second polarizer is detected by a photomultiplier. The RIPS spectra are obtained by recording the intensity of the coherent signal as a function of the time delay between pump and probe pulse. Whenever the molecular alignment induced by the pump pulse reappears the polarization of the probe beam will be modified due to a stimulated Raman interaction with the sample, which causes RCS recurrences in the signal [MPH93, LFM00].

2.4.2 Time-resolved coherent anti-Stokes Raman scattering (CARS)

The scheme of fs time-resolved coherent anti-Stokes Raman scattering (CARS) is depicted in Fig 2.9. The energy level diagram and the transitions involved in the CARS process are also given.

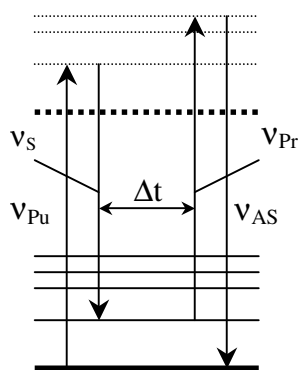


Fig. 2.9 Energy level diagram for CARS.

The pump and probe laser pulses have the same frequency $\nu_{pu} = \nu_{pr}$. The third laser pulse (Stokes, ν_S) is tuned to a lower frequency in such a manner that the difference between pump and Stokes laser frequencies is resonant with a vibrational transition in the ground state. While the pump pulse (ν_{pu}) and Stokes pulse (ν_S) are coincident in time ($\Delta t = 0$) the third probe pulse (ν_{pr}) arrives at a variable delay time. The time-resolved CARS spectrum is recorded as the dependence of the intensity $I(\Delta t)$ of the signal (anti-Stokes pulse, ν_{AS}) on the

delay time between the pump and probe pulses [SKM97a].

For CARS experiments, one can use two main configurations, collinear [HaC95] and folded BOXCAR arrangements (see Section 2.4.3.1). In case of collinear configuration, the CARS signal can be spectrally separated from the laser beams. On the other hand, the folded BOXCAR configuration permits a spatial discrimination of the CARS signal.

The above considered nonlinear methods have several advantages. Since for these techniques fs laser pulses are usually used, they have better time resolution. That leads to the higher precision for the determination of the rotational constants from RCS spectra. In these experiments a coherent signal is detected, therefore an excellent signal-to-noise ratio can be achieved with values of up to 10^4 in a gas cell and even for low number density samples expanded in a supersonic jet [MPH93, Rie02]. Moreover, nonlinear methods work under different experimental conditions from a seeded molecular beam (low temperature) [MJR02, JMR03, MRG03] to combustion processes and flames [LFM00, LMF01]. The both methods provide information about the ground electronic state structure. The main disadvantage of these methods is the square dependence of the signal from the sample number density.

2.4.3 The degenerate four-wave mixing process

The local response of a medium to incident electromagnetic radiation can be described by the induced macroscopic electric polarization, \mathbf{P} . The dielectric polarization of a medium can be written as an expression expanded in the power of the applied field strength [She84].

$$\mathbf{P} = \mathbf{P}^{(1)} + \mathbf{P}^{(2)} + \mathbf{P}^{(3)} + \dots = \epsilon_0(\chi^{(1)}\mathbf{E} + \chi^{(2)}\mathbf{E}^2 + \chi^{(3)}\mathbf{E}^3 + \dots) \quad (2.31)$$

Where $\chi^{(k)}$ is the susceptibility of the k^{th} order.

The first term, with the susceptibility $\chi^{(1)}$ is responsible for linear processes such as absorption, Rayleigh and spontaneous Raman scattering. The three wave mixing processes, like frequency doubling, vanish for isotropic media, and arise from the second term with the second-order nonlinear optical susceptibility $\chi^{(2)}$. Finally, last term in Eq. 2.31 $\mathbf{P} = \epsilon_0\chi^{(3)}\mathbf{E}^3$ is responsible for four-wave mixing processes such as CARS, degenerate four-wave mixing (DFWM) and third harmonic generation [Muk95, MPZ96].

2.4.3.1 Phenomenological description of DFWM (transient gratings picture)

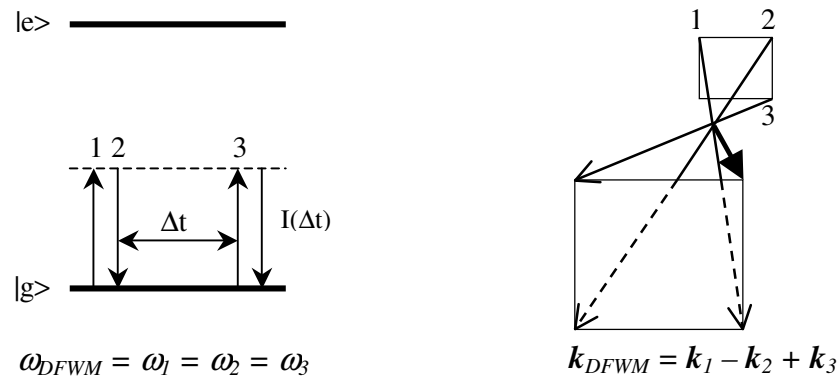


Fig. 2.10 (a) Energy levels diagram of the DFWM process; (b) Folded BOXCAR arrangement. Wave vectors of the three incident beams (k_1, k_2, k_3) and resulting signal beam k_{DFWM} .

In the DFWM process, three input beams of the same frequency ω which are identical in terms of pulse envelope (i.e. degenerate), interact with a nonlinear medium, producing a

fourth beam also at frequency ω [MPZ96]. Fig. 2.10a shows the simple energy diagram corresponding to this process.

In this work the experimental scheme with beams 1 and 2 coinciding in time preceding beam 3 in time were used. The conservation of the momenta for the three laser beams and DFWM signal beam is shown in Fig. 2.10b. This configuration is called folded BOXCAR arrangement, or three-dimensional forward geometry. The direction of the fourth (signal) beam has to be subjected to the phase matching condition, and energy conservation restricts the frequency of the measured signal [BZD99, MPZ96, She84].

$$k_{DFWM} = k_1 - k_2 + k_3, \quad (2.32)$$

$$\omega_{DFWM} = \omega_1 = \omega_2 = \omega_3.$$

The phase-matching condition holds automatically in case of collinear beam arrangement, when all three beams propagate along the same line. In that case, one encounters difficulties in separating the signal from the laser beams. Thus, the abovementioned BOXCAR configuration has been used.

Time-resolved four-wave mixing techniques can be explained in terms of the formation of transient grating by the incident beams 1 and 2 [Fay82, EGP86].

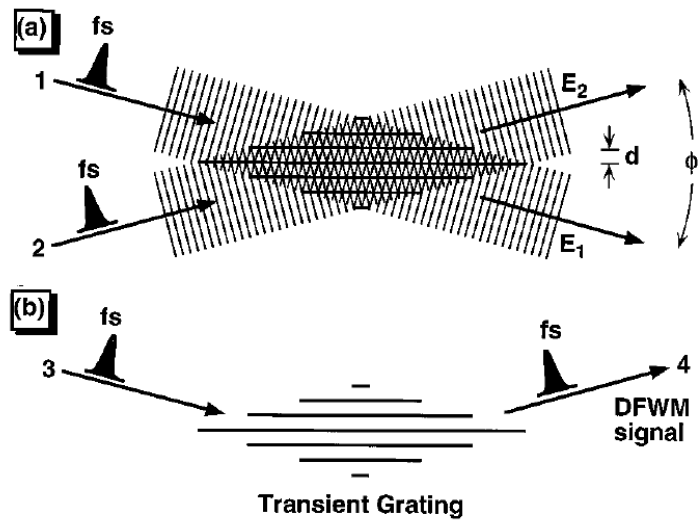


Fig. 2.11 DFWM processes illustrated by transient grating picture.

Three degenerate laser beams are interacting with a medium. At the cross section of the two beams E_1 and E_2 , the spatial modulation of their electric fields varies due to constructive and

destructive interference (see Fig. 2.11). Thus, the molecules in the interaction region are affected by different electric field intensities according to their position that leads to formation of a transient grating of polarized molecules in space. The incoming probe beam is scattered from the induced grating. Hence, the transient grating formation can be examined by the detection of Bragg scattering of a third beam.

2.4.3.2 Intensity of the fs DFWM spectra

As was mentioned before, the four-wave mixing process arises from the term of Eq. 2.31 with the non-linear third-order susceptibility $\chi^{(3)}$, and the rotationally-sensitive part of a general fs DFWM signal is expressed through this molecular susceptibility $\chi^{(3)}(t)$ as follows [MPL95, CDS93]

$$I_{DFWM}(t) = I_{pr}(t) \otimes \left(I_{pu}(t) \otimes \left| \chi^{(3)}(t) \right|^2 \right) e^{-t/\tau}. \quad (2.33)$$

Here $I(t)$ is the intensity of the laser pulses, τ is a phenomenological decay time, which accounts for the DFWM signal intensity decrease caused by various process, e.g., collisions, and $\chi^{(3)}(t)$ is proportional to the imaginary part of the second rank orientational correlation function of the symmetric traceless time-dependent polarizability tensor (PT) [MPL95]

$$\chi^{(3)}(t) \sim \text{Im} \sum_{i,j=A,B,C} \langle [\beta_{ij}, \beta_{ji}(t)] \rangle \quad (2.34)$$

The indices label the axes of the principal moments of inertia,

$$\beta_{ij} \equiv \alpha_{ij} - (\bar{\alpha}/3)\delta_{ij}, \quad \bar{\alpha} = \sum_{i=A,B,C} \alpha_{ii},$$

$$\beta_{ij}(t) = \exp\{-iH_R t / \hbar\} \beta_{ij} \exp\{iH_R t / \hbar\} \quad (2.35)$$

α_{ij} is the imaginary part of the PT of a ground vibronic state and H_R is rotational Hamiltonian.

Generally speaking, it is necessary use the total (vibration plus rotation) electronic ground state Hamiltonian $H = H_V + H_R$. But if one is interested in the purely rotational coherence, and one monitors the fs DFWM response at times that are greater than the characteristic vibrational relaxation time the formulas (2.34, 2.35) are valid.

2.4.3.2.1 fs DFWM of linear rotor and symmetric tops

The Eq. 2.33 reduces to Eq. 2.36, which is providing the intensity of a DFWM signal for a symmetric top species if the PT possesses also a cylindrical symmetry with respect to the molecular figure axis. The transient following excitation at $t = 0$ is obtained from the Fourier transformation (summing sine functions over all Raman transition frequencies weighted with the population distribution and transition probabilities) [FBG00, MJR02].

$$I_{FWM}(t) = I_{pr}(t) \otimes \left(I_{pu}(t) \otimes \sum_{E_{g'} > E_g} (\rho_{g'} - \rho_g) A_{gg'} \sin(\Omega_{gg'} t) \right)^2 e^{-t/\tau} \quad (2.36)$$

where $\Omega_{gg'}$ is the fundamental frequency of the Raman transition $g \rightarrow g'$, see equations (2.7, 2.9, 2.10), $\rho_{g'} - \rho_g$ the difference in the population of the two levels, $A_{gg'}$ the orientation integrated Raman transition probability and τ is an external dephasing time. The population ρ_g of the levels is calculated according to the Boltzmann distribution including nuclear spin statistics. Additionally, all frequencies of the synthetic Raman spectrum are weighted by the J dependence of the Raman cross section $A_{gg'}$ (Placzek-Teller coefficient; for linear molecules they are given explicitly by Eq. 2.20) [PIT33]. The result of the sum over all Raman frequencies is convoluted with the temporal evolution $I_{pu}(t)$ of the pump pulses, squared and convoluted again with $I_{pr}(t)$ – the probe pulse.

Upon application of the Raman selection rules to the term values for a symmetric nonrigid oblate rotor, expressions for the Raman transition frequencies for the R and S branch can be given in an analytical form by Eqs. (2.9) and (2.10), where $\Delta J = \pm 1$ does not appear for $K = 0$. These values are used together with Eq. (2.36) to calculate the corresponding fs DFWM spectrum. This particular consideration for symmetric species with PT of cylindrical symmetry allows to make simulations of the experimental fs DFWM spectra more simple and save computer time during the fitting procedure.

2.4.3.2.2 fs DFWM of asymmetric tops

In order to calculate the fs DFWM signal via Eqs. 2.33 - 2.35 in the most general case of a nonrigid asymmetric top molecule, the Watson parametrization of the nonrigid asymmetric top Hamiltonian can be adopted:

$$H = F(\hat{J}_A) + \Phi(\hat{J}_A)\hat{J}_{CB}^2 + \hat{J}_{CB}^2\Phi(\hat{J}_A). \quad (2.37)$$

Here

$$\begin{aligned} F(\hat{J}_A) &= (C + B)\hat{J}^2/2 + (A - (C + B)/2)\hat{J}_A^2 - \Delta_J\hat{J}^4 - \Delta_k\hat{J}_A^4 - \Delta_{Jk}\hat{J}^2\hat{J}_A^2, \\ \Phi(\hat{J}_A) &= (C - B)/4 - \delta_k\hat{J}_A^2 - \delta_J\hat{J}^2, \quad \hat{J}_{CB}^2 \equiv \hat{J}_C^2 - \hat{J}_B^2, \end{aligned} \quad (2.38)$$

\hat{J}_i are the angular momentum operators in the molecular frame, $A \geq B \geq C$ are the rotational constants, $\Delta_J, \Delta_k, \Delta_{Jk}, \delta_k, \delta_J$ are the CD constants, and the a-axis of the smallest moment of inertia (the largest rotational constant) is chosen as the quantization axis.

The Hamiltonian has been used to calculate the eigenfunctions of the rotational states by a numerical diagonalization of the asymmetric top Hamiltonian on the basis of the symmetric top states (see Section 2.1.4).

2.4.4 Simulation of the fs DFWM spectra

In order to evaluate Eq. 2.33 for a general nonrigid asymmetric top molecule, the original computer code developed by P. M. Felker for the simulation of the ground-state RCS transients for rigid asymmetric tops [FeZ95a] has been modified.

In general, this procedure consists of the following steps. First, from the assumed rotational and CD constants the nonrigid asymmetric rotational Hamiltonian is obtained. The eigenvalues of the rotational states are calculated by numerical diagonalization of the Hamiltonian in a basis of symmetric top states. Second, the rotational beat frequencies are determined and also their amplitudes. The amplitudes of these frequencies are calculated according to a Boltzmann distribution with an assumed temperature and weighted by the J dependence of the Raman cross section. In the next step the received quantum beat spectrum is converted to the time-domain spectrum by fast Fourier transformation. And in the last step, the time-domain trace is convoluted with the temporal evolution of the laser pulses. The laser pulse shapes are assumed to be of Gaussian type.

Subsequently, the new DFWM code has been incorporated into a nonlinear fitting routine, in order to obtain high-resolution data from experimental fs DFWM transients. The

simulated fs DFWM spectrum is determined by several different parameters. These include eight molecular parameters (the rotational and CD constants), the rotational temperature T , the decay time τ , and the five components of the traceless symmetric PT β_{ij} . In principle, all the aforementioned parameters can be regarded as fitting parameters and, therefore, can be varied to bring experimental and simulated spectra into correspondence. Thus, a natural question arises: how sensitive is the simulated fs DFWM spectrum to all these parameters? It is thus desirable to disregard less important quantities, in order to reduce the number of parameters and make the fitting procedure more reliable and efficient. In connection with this, the following two observations are of particular importance. First, if a molecule is a slightly asymmetric top, then the asymmetry-induced CD constants δ_k, δ_j can be put to zero or fixed to certain (plausible) values. Second, one can multiply the PT by an arbitrary scaling factor, that is tantamount to changing the signal intensity (normalization). One can therefore proceed as follows. Without any loss of generality, one can parameterize the diagonal components of the traceless PT as follows:

$$\beta_{AA} = \xi, \beta_{BB} = \eta, \beta_{CC} = -\xi - \eta, \quad -\infty < \xi, \eta < \infty. \quad (2.39)$$

By introducing the polar coordinates in the $\xi\eta$ space ($\xi = r \cos(\varphi)$, $\eta = r \sin(\varphi)$), one can normalize the PT according to the requirement $(\beta_{AA})^2 + (\beta_{BB})^2 + (\beta_{CC})^2 = 1$. This is equivalent to choosing $r = 1 / \sqrt{2 + \sin(2\varphi)}$. In doing so, we end up with the PT $\tilde{\beta}_{ij}$, whose components are connected with those of the original PT α_{ij} via the transformations

$$\tilde{\beta}_{ii} = (\alpha_{ii} - \bar{\alpha}/3) / r, \quad \tilde{\beta}_{ij} = \alpha_{ij} / r \quad (i \neq j). \quad (2.40)$$

An important message from that formula is the following. If all the components of the PT are known, one can use them directly in the simulations. If one tries to extract the components of the PT from experimental transients by a fitting procedure, one should keep in mind that the signal is not sensitive to all the components of the PT in full measure. There are various sets of equivalent PTs (with different r and $\bar{\alpha}$) which, within a numerical normalization factor, give rise to equivalent signals. Even in the most fortunate case, one gets from the fitting procedure the components of the PT $\tilde{\beta}_{ij}$, from which one cannot

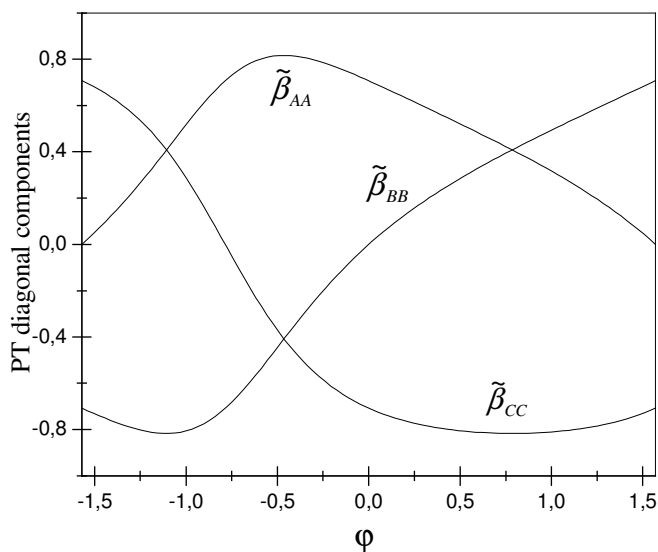


Fig. 2.12 Visualization of the parametrization of the diagonal components of the PT, $\tilde{\beta}_{ii}(\varphi)$, $i = A, B, C$.

construct the original PT tensor α_{ij} uniquely, because the DFWM signal is not sensitive to the parameters r and $\bar{\alpha}$. Without any loss of generality one can additionally imply that, e.g., $\tilde{\beta}_{AA}$ is positive. This means that $-\pi/2 \leq \varphi \leq \pi/2$ specifies all the nonequivalent (from the point of view of simulations) diagonal components of the PTs. Moreover, the diagonal components of any PT tensor are usually much larger than the off-diagonal ones (see, e.g., [JÅO02]). Therefore, to a good approximation, one can neglect the off-diagonal components in favour of diagonal ones, and represent any PT by only one parameter: φ . This finding is quite important for doing actual simulations, since it approximate the original six-component symmetric PT to a single angle φ . The meaning of this parameter is clarified in Fig. 2.12, which reproduces the diagonal components $\tilde{\beta}_{AA}$ of the PT as the functions of φ . Of course, the meaning of the angle φ is less transparent than, e.g., that of the values of projections of the transition dipole moment on the axes of the molecular frame, but the Fig. 2.12 helps to visualize how the PT components depend on that angle [RMG03].

2.4.5 Characteristics of the rotational coherence recurrences obtained by fs DFWM

From comparison of the Eqs 2.18 and 2.36 one can see that in order to simulate the position and the shape of the recurrences obtained by time-resolved fs DFWM one could square the time-derivative of the resonant RCS spectrum. Fig. 2.13 shows the spectra obtained in this way from the spectra depicted in Fig. 2.5. The upper trace shows the approximate shape of K-type transients for the rigid top species. In contrast with K-type transients obtained by

resonant methods the fs DFWM K-transients have a double peak structure with constant positive polarity, which results from the squaring of the signal.

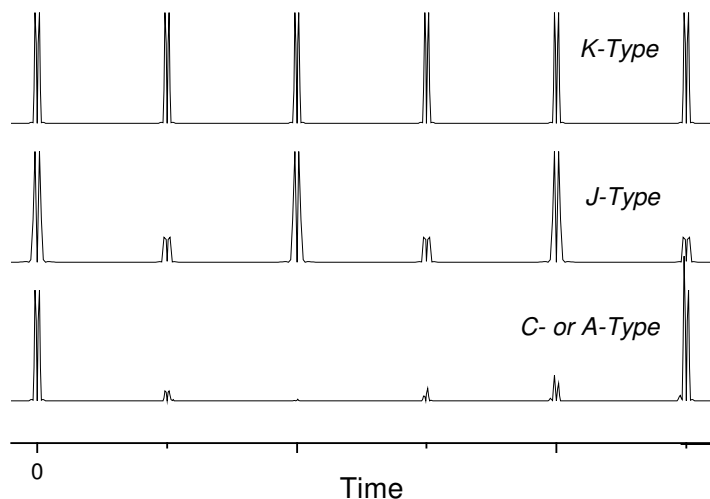


Fig 2.13 Schematic depiction of the different types of RRs obtained by fs DFWM method. Traces obtained by squaring of the time derivatives of the traces from Fig. 2.5.

Two series of transients with different intensity can be observed in the middle trace of Fig. 2.13, these are half (odd) and full (even) J-type recurrences. This is in agreement with the usual observation for J-type RRs of symmetric top species neglecting CD. The half recurrences correspond to the S branch in the Raman spectrum, which extends to higher frequencies than the R branch. The full recurrences originate from the sum of QBs from the S and R branches. The A- and C-type recurrences show an ill-defined shape of the transients with modulated intensity similar to resonant experiments (Fig. 2.13 bottom trace).

All observations considered in Section 2.2 concerning the recurrence times and requirements for appearance for the different type of rotational transients are also valid for fs DFWM. One aspect is worth to investigate here that is how RCS spectra obtained by fs DFWM depend on the parameter φ , which characterizes the diagonal elements of the polarizability tensor (see section 2.4.4)?

Fig. 2.14 shows the simulation of fs DFWM spectra for species with the following rotational constants $A = 77.53$, $B = 12.05$, $C = 10.42$ GHz. These constants are close to the values of the formic acid molecule. From Ray's asymmetry parameter $\kappa = -0.951$ one can conclude that this species is a near-prolate top. In order to emphasize the dependence of the fs DFWM

spectra on the parameter φ all CD constants are set to zero. The trace in Fig. 2.14a gives a simulated fs DFWM spectrum for $\varphi = -0.464$, i.e., $\tilde{\beta}_{AA} > \tilde{\beta}_{BB} = \tilde{\beta}_{CC}$ (see Fig. 2.12).

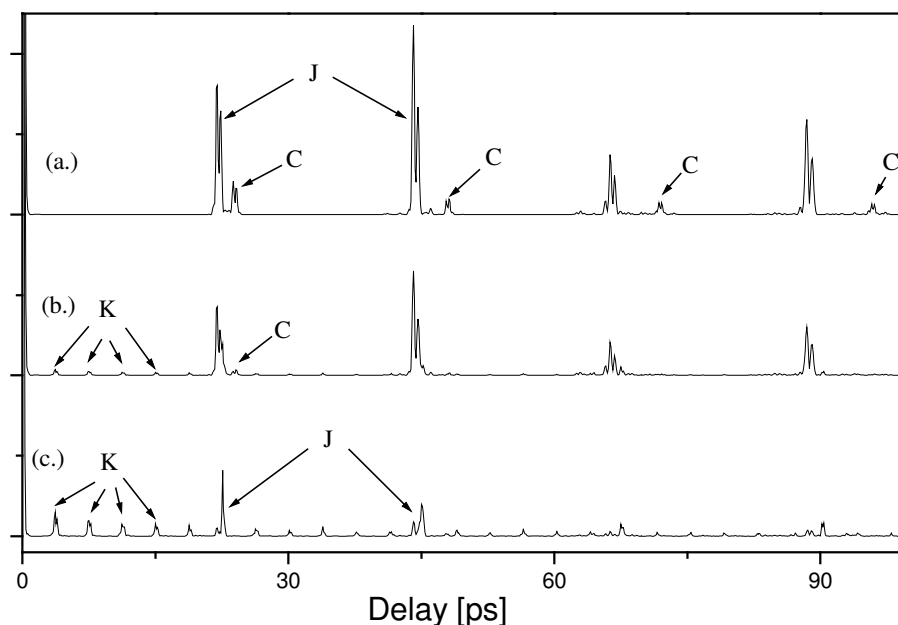


Fig 2.14 Simulated RCS fs DFWM spectra for a species with rotational constants $A = 77.53$, $B = 12.05$, $C = 10.42$ GHz for different values of φ . **(a.)** Simulation with “parallel” polarizability and moment-of-inertia tensors, related to $\varphi = -0,464$; **(b.)** Simulation with “hybrid” polarizability $\varphi = 0,1$; **(c.)** Simulation with “perpendicular” polarizability and moment-of-inertia tensors $\varphi = 0,785$. The intensity of the transients is normalized to zero-time peak.

In this case the PT is symmetric with respect to the a -axis of the molecular frame. Two types of rotational recurrences can be identified in the trace a. First, there are intense J-type transients with a time separation $t_J \approx 1/[2(B+C)]$. Second, C-type recurrences with smaller intensity and slightly longer period $t_C \approx 1/4C$ appear due to the near-prolate top symmetry of the species. With increase of the parameter φ from -0.464 ($\tilde{\beta}_{AA} > \tilde{\beta}_{BB} = \tilde{\beta}_{CC}$) to 0.785 ($\tilde{\beta}_{AA} = \tilde{\beta}_{BB} > \tilde{\beta}_{CC}$) the following observations can be made. The simulated spectrum for $\varphi = 0.1$ ($\tilde{\beta}_{AA} > \tilde{\beta}_{BB} > 0$, $\tilde{\beta}_{CC} < 0$) still exhibits J- and C- types transients but with reduced intensity (Fig 2.14b) in comparison to the trace for $\varphi = -0.464$. Moreover an additional set of peaks can be found in the spectrum with temporal separation $t_K \approx 1/[4A-2(B+C)]$, these peaks can be assigned to K-type transients. It can be seen that in case of $\varphi = 0.1$, i.e., [with a

polarizability component perpendicular to the figure axis (*a*-axis)] one can expect a similar spectral behaviour as for perpendicular dipole transitions in resonant RCS experiments. In terms of rotational Raman spectroscopy, which is the frequency analogue to fs DFWM spectroscopy, one has to take into account that for accidental symmetric tops the selection rules $\Delta J = 0, \pm 1, \pm 2$ and $\Delta K = 0, \pm 1, \pm 2$ are valid [Her45, PIT33]. Thus, one can expect a similar spectral behaviour as for perpendicular dipole transitions, which are known to give rise to K-type recurrences in rotational coherence spectroscopy (see Table 2.1 in Section 2.2.3).

With increase of the parameterized polarizability angle the reduction of intensity for J- and C- and increase for K-type transients become more pronounced (Fig. 2.14c). One can also expect the corresponding effect for near-oblate top symmetric molecule, i.e., rise of K-recurrences with appearance of the polarizability component perpendicular to the figure axis (*c*-axis).

Chapter 3

3 Experimental setup

In this chapter, a description of the experimental setup that was used for the measurement of rotational coherence spectra will be presented. The experimental setup consists of an ultrashort pulse laser system, an optical setup, a vacuum apparatus, and a synchronized data acquisition system. The detailed description of the main components of the setup for the “picosecond” experiments has been given in Ref. [WRB01b]. Since, during this work two types of experimental implementations of RCS have been applied, two modifications of the experimental setup have been used. Formally, these modifications are called the “picosecond” and “femtosecond” setup. The “femtosecond regime” has been applied for fs DFWM experiments whereas the “picosecond regime” has been used for the two-color pump-probe (1+1') and (1+2') photoionization (PPI) measurements.

3.1 Laser system

The laser setup is based on components of a standard commercial 1kHz solid state chirped pulse amplified (CPA) laser system. A block diagram of the CPA system is given in Fig. 3.1. The main components are a femtosecond Ti:Sapphire oscillator with cw argon-ion pump laser, a stretcher-compressor unit, and a regenerative amplifier pumped by a Q-switched Nd:YLF laser. Two optical parametric generators/amplifiers are used in order to obtain picosecond tunable UV radiation for the two-color ionization experiments. The general features of the laser system for the femtosecond experiments are given in Section 3.1.1. The modifications and additional optical system for the picosecond experiments are described in Section 3.1.2.

Block Diagram of Ultrafast ps/fs-Laser System

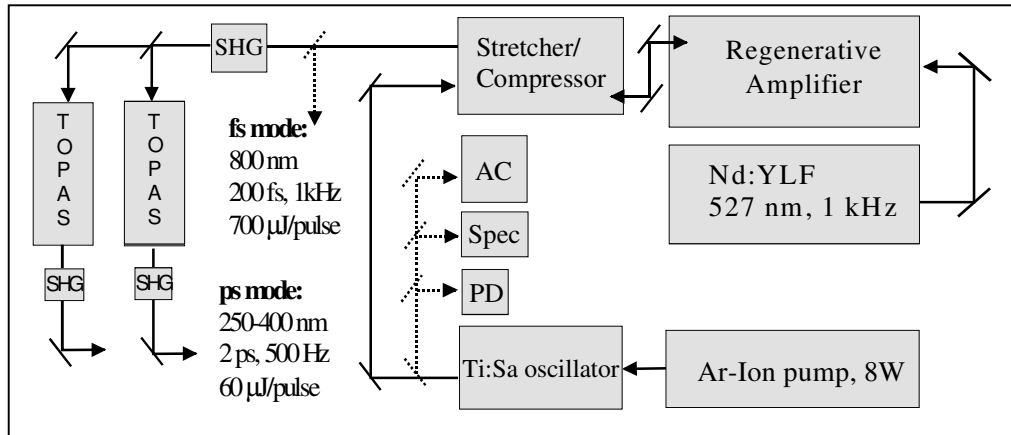


Fig 3.1 Block diagram of the ultrashort chirped-pulse amplified (CPA) laser system.

Where are **PD** – photodiode; **Spec** – monochromator with CCD camera for spectrum check; **AC** - scanning autocorrelator; **SHG** - second harmonic generation; **TOPAS** – optical parametric generator/amplifier.

3.1.1 Femtosecond setup

A Kerr-lens-mode-locked Ti:Sapphir oscillator (Coherent, Mira Basic, 800 nm, 76 MHz, FWHM of autocorrelation (AC) 130 fs, bandwidth 14 nm, average power > 600 mW) is pumped by an all line 8W argon-ion laser (Coherent Innova 310).

This output is used for chirped pulse amplification (CPA) (Quantronix, 4800 Series). The output is directed to a stretcher-compressor unit in order to stretch the pulse in time. Amplification takes place in a regenerative Ti:Sapphire amplifier which is pumped by the second harmonic of a Q-switched Nd:YLF laser (Quantronix, 527 Series), delivering 10 mJ/pulse. Synchronization of the oscillator with the regenerative amplifier, the Nd:YLF laser, and the experiment is done by dividing the 76 MHz signal sampled with a fast photodiode by 76 000. A divider and a digital delay generator which is combined with the Pockels cell control unit (Medox Electro-Optics) is used for this purpose, generating the 1 kHz master trigger for all following units, including the Pockels cell in the regenerative amplifier and the Q-switch of the Nd:YLF laser. A selected pulse is amplified in the regenerative amplifier up to 2 mJ pulse energy and then recompressed in the compressor stage. A low dispersion grating (1200 lines/mm) is used in stretcher-compressor unit in

order to achieve a short pulse. Typical output parameters from the CPA system in the “femtosecond regime” are: wavelength 800nm, FWHM of AC 200fs (bandwidth 7nm), pulse energy 700 μ J at a repetition rate of 1 kHz.

3.1.2 Picosecond setup

In the “picosecond” regime, the same CPA unit was used with some modifications. The output parameters of the Kerr-lens-mode-locked Ti:Sapphire oscillator are: pulse width \approx 180 fs FWHM (AC), bandwidth \approx 5.5 nm, average power > 700 mW with wavelength 800 nm and repetition rate 76 MHz.

The stretcher was modified for narrow-bandwidth ps-operation using a grating with high dispersion (2000 lines/mm) and an adjustable slit mask in order to decrease the spectral bandwidth to \approx 0.42 nm. The 76 MHz signal from oscillator was divided by 152000 to achieve 500 Hz repetition rate.

Table 3.1: Parameters of the laser system in “femtosecond” and “picosecond” versions.

Ti:Sapphire oscillator		
	<i>fs – version</i>	<i>ps – version</i>
Pulse duration	130 fs, AC FWHM	180 fs, AC FWHM
Bandwidth	14 nm	5.5 nm
Wavelength	800 nm	800 nm
average power	\sim 600 mW	\sim 700 mW
Repetition rate	76 MHz	76 MHz
CPA system		
	<i>fs – version</i>	<i>ps – version</i>
Pulse duration	200 fs, AC FWHM	5 ps, AC FWHM
Bandwidth	7 nm	0.52 nm
Wavelength	800 nm	800 nm
Pulse energy	700 μ J	1 mJ
Repetition rate	1 kHz	500 Hz
Parametric generator (TOPAS)		
	<i>fs – version</i>	<i>ps – version</i>
Tuning range		250-400 nm
Pulse duration		2 ps (typical)
Spectral width		\sim 10 cm^{-1}
Pulse energy (two TOPAS)		2x30 μ J at 272 nm

Typical output parameters for the CPA system are: wavelength 800 nm, repetition rate 500 Hz, pulse energy after compression > 1 mJ, AC 5 ps FWHM, bandwidth ~ 0.52 nm. A telescope in front of the compressor has been used to adjust the pulse intensity for compression and a second telescope after the compressor is used to optimize the beam diameter for SHG and the parametric generator. In order to obtain tunable radiation the second harmonic of the CPA output is produced in a 2 mm thick BBO crystal and directed into two traveling-wave optical parametric generators and amplifiers of superfluorescence (TOPAS, Light Conversion) [DPP93, DPT96]. The second harmonic of their visible output is used for the pump-probe ionization experiments. The output parameters are: wavelength 250-400 nm, repetition rate 500 Hz, AC 3 ps FWHM, bandwidth ≈ 10 nm. The pulse energy of each of the TOPAS is > 30 μ J.

The typical output parameters of the laser system in “femtosecond” and “picosecond” versions are summarized in Table 3.1

3.2 Optical setups

Two different beam arrangements have been used in the experiments. In case of the two-color pump-probe measurements a Michelson-type interferometer was applied. For fs DFWM measurements the so-called folded BOXCAR arrangement was employed [BZD99, FBG00]. Fig.3.2 shows the optical setup that has been used for fs DFWM measurements. The fundamental output from the Ti:Sapphire amplifier is split into three equal parts – two pump and one probe beam – by two beam splitters (BS1, BS2). The polarizations of all three beams are parallel to each other. The path lengths of the two pump pulses are matched by a manual translation stage (delay 2) that provides fine adjustment so that the pulses coincide in time. The probe beam is directed over a computer controlled translation stage (delay 1, Anorad LW10). The probe pulse could be delayed in time up to 4 ns with a maximum resolution of $\Delta t = 1.3$ fs (0.1 μ m step size) and a maximum delay range of 60 cm (4 ns, two passes). For the precision of the delay line an absolute accuracy of 20 μ m/600 mm (0.003 %) has been guaranteed by the manufacturer. As a reflector a Gold-coated hollow retroreflector is used. The three beams are focused by a 300 mm focal length lens (L1) into a cell containing a sample gas at reduced pressure. The sample cell can be alternatively replaced by a supersonic expansion or a heat pipe oven. The adjustment of all

beams in time and space is achieved by using two identical masks and by substituting the sample by a BBO crystal so that the pairwise SHG of all beams as well as the DFWM signal can be optimized.

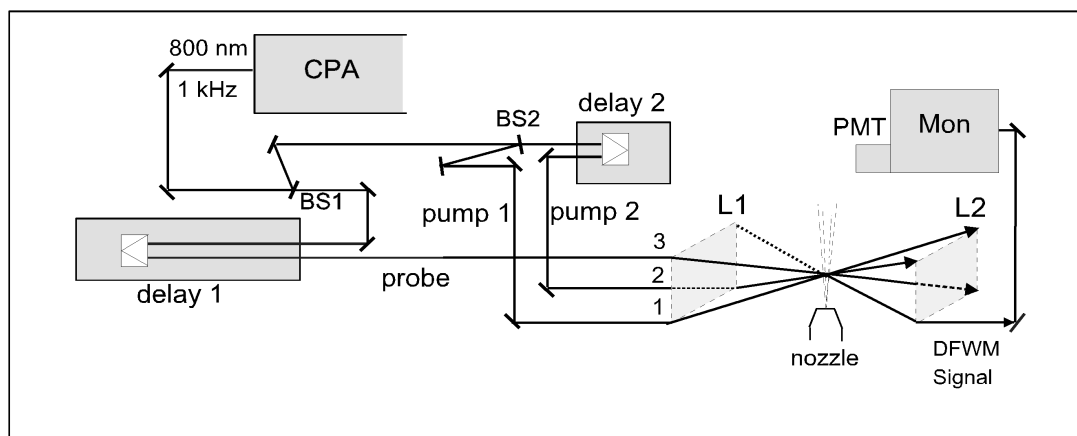


Fig. 3.2 Optical setup for femtosecond DFWM: **CPA** - chirped pulse amplified Ti:Sapphire laser system, **delay 1** – a computer controlled translational stage 0-4ns, **delay 2** - optimized for overlap of pulses pump1 and pump2, **Mon** - monochromator, **PMT** - IR sensitive photomultiplier.

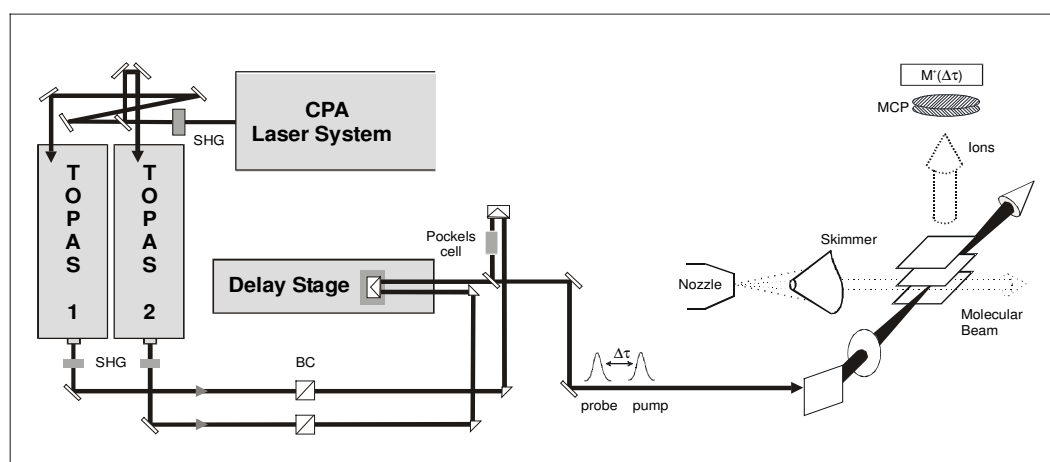


Fig. 3.3 Optical setup for picosecond pump-probe ionisation experiments: **SHG** – second harmonic generation, **BC** – Berek compensator, **MCP** – microchannel plate.

After recollimation with a second lens ($L2$, $f = 300$ mm) the DFWM signal beam is spatially filtered by a set of apertures and collimated before it passes through a monochromator (Oriel 77200). The maximum bandwidth of the monochromator (≈ 14 nm), at the center wavelength (800 nm) has been used. As a detector an IR sensitive photomultiplier (EMI 9684B) was used.

For the two-color picosecond pump-probe experiments, the UV laser pulses of different wavelength from the two TOPAS are sent through a Michelson-type interferometer equipped with two fused-silica triple prisms as retroreflectors and a dielectric 50/50 beam splitter (see Fig. 3.3). One beam (pump beam) is directed through the fixed arm of interferometer and the other (probe beam) through a computer-controlled linear positioning stage (Anorad, LW10). The pump and probe beams are recombined on the dielectric 50/50 beam splitter.

The Berek compensators (BC) in each arm of the interferometer have been used for the control and rotation of the polarization of each individual beam. The beams exiting the interferometer are aligned collinearly and focused into the vacuum apparatus with a CaF₂ or fused-silica lenses with different focus lengths, depending on the studied molecular system. In order to perform difference measurements on a pulse to pulse basis a UV Pockels cell (Gsänger, LM10SG, equipped with windows coated for the UV, transmission at 300 nm > 93 %) can be introduced in the fixed arm of the interferometer. Synchronized to one half of the repetition rate of the laser system, alternating measurements on two different relative polarizations of pump and probe pulse measurements for the probe pulse can be performed.

3.3 Vacuum systems and signal detection

The RCS experiments were carried out under different experimental conditions. A broad range of rotational temperatures (10 – 450 Kelvin) was used during this work. In order to cool the species to low rotational temperatures one can use the supersonic expansion technique. Thus, simplified RCS spectra are obtained and molecular systems with weak binding energies, which do not exist at high temperatures, can be investigated. All pump-probe ionization experiments and part of the fs DFWM experiments have been done under supersonic expansion conditions. To overcome the square dependence of the fs DFWM signal from species number density and get additional structural information (for example centrifugal distortion) the experiments at room and elevated temperatures have been performed. In the following sections an overview of the vacuum systems used in this work is given. Additionally, the signal detection system in case of the ionization experiments is considered.

3.3.1 Molecular beam vacuum system

The vacuum system for the pump-probe ionization experiment consists of two vacuum chambers – the expansion and ionization chambers separated by a skimmer (2mm) (see Fig. 3.3). The typical background pressure is $4 \cdot 10^{-4}$ mbar in the expansion chamber and $< 5 \cdot 10^{-5}$ mbar in the ionization chamber. The chambers are differentially pumped by three turbo molecular pumps: 1100 l/s (Leybold Turbovac 1100) in the expansion chamber, 450 l/s (Leybold Turbovac 450) in the ionization chamber and 500 l/s (Balzers TPH 510S) in the detection region of the time-of-flight mass spectrometer.

A seeded continuous supersonic expansion with argon or helium as carrier gas is expanded through a nozzle with 80 μm diameter. In order to entrain solid samples into the carrier gas, the sample is kept in a stainless steel container and heated up to 100 °C upstream from the nozzle. For liquid samples a gas mixing system outside the vacuum apparatus is employed. The stainless steel containers for the substances can be cooled or heated and the carrier gas is bubbled through the liquid sample. The molecular beam passes through a skimmer diameter into the ionization region of a home-built linear Wiley-McLaren-type time-of-flight mass spectrometer ($m/\Delta m \approx 300$). The ionization region is located approximately 10 cm downstream from the nozzle. The generated ions are detected by a home-built two-stage microchannel plate detector [WRB01b].

For obtaining a seeded supersonic jet expansion for the fs DFWM experiments a piezoelectric, pulsed nozzle (repetition rate: 1 kHz, diameter: 0.5 mm) based on the design of Gerlich and coworkers [PaG94] as well as continuous supersonic expansion (nozzle diameter: 0.5 mm) were used. In case of the measurements with the pulsed nozzle the vacuum chamber was pumped by turbo molecular pump 1100 l/s (Leybold Turbovac 1100). The background pressure in that case was below 10^{-3} mbar.

Not for all substances a piezoelectric pulsed nozzle is suitable. Some substances can damage the piezoelement, especially the contact area for the driving voltage, which can cause incorrect operation of the nozzle. For investigation of more aggressive substances (like formic and acetic acid) a continuous nozzle expansion was used. In that case the vacuum chamber was evacuated by a 270 m³/h roots pump (Balzers, WKP 250A). The background pressure during the experiment was up to $\approx 10^{-1}$ mbar.

The vacuum systems were backed by a pump (Leybold, Ruvac WAU501, 500 m³/h) in combination with a rotary pump (Leybold, Trivac D60A, 60m³/h).

3.3.2 Vapor cell and heat-pipe

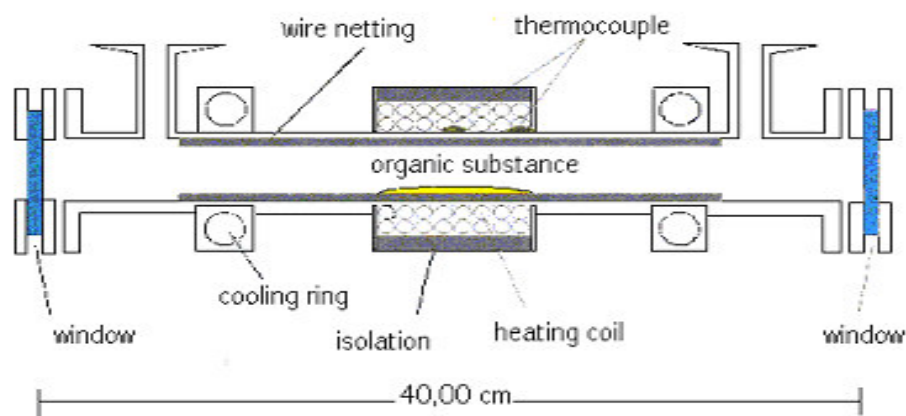


Fig. 3.4 Schematic arrangement of the heat-pipe oven.

The vacuum chamber, which has been used during the fs DFWM measurements, can be used as a gas cell operated at room temperature. The application of coated focusing lenses L1 and L2 (see Fig. 3.2) as windows for the cell reduces the scattered laser light and correspondingly improve the signal-to-noise ratio. Many molecules have a very low vapor pressure at room temperature (< 0.1 mbar.). Therefore they have to be heated in order to achieve a high enough concentration. A heat-pipe oven was used which is known as an elegant technique for optical investigation of metal vapors at high temperature [ViC69, ViH71, Vid96].

Fig. 3.4 shows the design of the heat-pipe oven. It consist of a cylindrical tube (40 cm length and 20 mm diameter) the inner wall of which is covered by a capillary structure, for example, several layers of woven mesh. The central zone is heated by a heating cable (3 m length, 500 Watt, maximal temperature < 900 K). This zone is covered by thermo-insulating material in order to minimize losses of the heat. The regions before the windows (cooling zones) are water cooled. The temperature gradient along the pipe is controlled by two thermocouples.

In order to operate this device, the pipe is first of all filled with an inert gas at low pressure (~5mbar). Heating of the central zone causes evaporation of the substance at a temperature for which the vapor pressure equals or just exceeds the inert gas pressure. This causes the vapor to diffuse towards both ends until it condenses again before the windows. Ideally, the condensed, liquid sample is then guided back into the heating zone by the metal mesh that acts like a wick in a candle. Finally an equilibrium is reached, in which the center part of the pipe is filled with the substance vapor at a pressure determined by the confining inert gas at both ends of the pipe [ViC69].

The heat-pipe oven exhibits a number of desirable features. First, the inert gas boundaries solve the window contamination problem; because the substance vapor is kept in the inner part of the tube and only the inert gas is in direct contact with the windows. That makes the heat-pipe technique very useful for spectroscopic studies. The second advantage is that the heat-pipe oven can be operated continuously under well-known conditions. The pressure can be determined directly from the inert gas pressure. The temperature is nearly constant over the whole vapor zone and is only a function of the confining inert gas pressure as long as the vapor flow velocities are not too large [ViH71]. Therefore one of the most fundamental applications of the heat pipe was the accurate measurement of vapor pressure curves [BoS65, BoS67]. Finally, this tool can be easily adopted for fs DFWM experiments, because of this it was used for DFWM experiments in the frequency regime before [CPC90, PCC92, MPK98].

3.4 Timing, data acquisition, and control

The trigger and timing scheme is depicted in Fig. 3.5. It consists of one part related to the laser system, and another part related to the data acquisition. For the timing of the data acquisition, the 500 Hz or 1 kHz (DFWM experiments) master trigger from the laser system is multiplexed via electronic amplifiers to four parallel channels. These trigger signals arrive about 20 ns before the first laser pulse. This time interval is sufficient to trigger the boxcar integrator (Stanford Research, SR250) and an oscilloscope (LeCroy 9362) by the actual master pulse, minimizing the timing jitter, that would have been introduced, if the preceding pulse would have been used for this timing. The signal is monitored by the oscilloscope and is integrated in the boxcar integrator. Its output signal is digitized by an ADC card

(Meilhaus ME260) at 500 Hz (1kHz) and stored on a personal computer after averaging over number of laser pulses (typically 500).

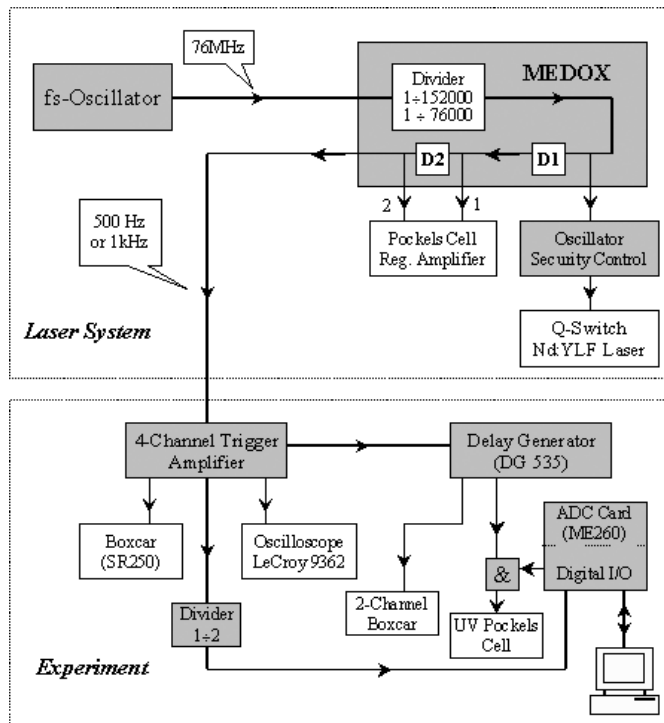


Fig. 3.5 Trigger and timing scheme used for synchronization of the different components of the laser system and data acquisition.

The pulse-to-pulse switching mode can be used for the investigation of spectral regions of additional interest to obtain RCS data with reduced baseline fluctuations. The timing of the UV Pockels cell (for one lock-in-type alternating scan mode) and the two-channel boxcar integrator (for monitoring the laser energy) has to be triggered by the preceding laser pulse. The corresponding delay is adjusted by a delay generator (Stanford Research DG535). The computer software which enables the switching of the UV Pockels cell provides a logic signal to the digital I/O of the ADC card. The actual low-jitter timing of the UV Pockels cell, is done with reference to the master trigger, connecting both signals with a logical “AND” in a synchronization unit. The data are collected into two channels for different polarizations of the UV Pockels cell “ON” or “OFF”. A third channel is used to store the calculated difference signal “ON”-“OFF” [WRB01b].

Chapter 4

4 Nonrigid Symmetric Top Molecules Studied by fs DFWM

4.1 Introduction

In this chapter, the results of time-resolved fs DFWM measurements for the symmetric top species (benzene C_6H_6 , perdeutero-benzene C_6D_6 and cyclohexane C_6H_{12}) will be presented. The measurements have been performed in a gas cell at room temperature (298K) and in a supersonic expansion (30-40K). All of these molecules are oblate symmetric tops. In case of benzene and perdeutero-benzene, the molecules belong to the D_{6h} point group. Cyclohexane in the chair conformation belongs to the point group D_{3d} . From the fitting of the experimental data very accurate rotational and centrifugal distortion (CD) constants for these molecules in the ground electronic state have been obtained.

Since accurate spectroscopic data for benzene are available from several experimental methods and this molecule is highly polarizable with third-order nonlinear optical susceptibility $\chi^{(3)} \approx 12 \times 10^{-14}$ esu [MBH83, KaM85] it is a good model system to test fs DFWM spectroscopy as a high-resolution method. Another intention of the benzene investigation was to show that fs DFWM could be employed for medium-sized molecules in a supersonic jet expansion. The combination of the gas cell experiment at room temperature and the molecular beam experiment at low temperature provides information about the influence of centrifugal distortion and temperature on the fs DFWM signal and opens the perspective for the structural study of more complex species. Moreover, a change in the shape of the rotational recurrences (RRs) with increase of the laser intensity will be considered by example of the fs DFWM spectra of benzene in a seeded supersonic jet.

Apart from highlighting the versatility of the fs DFWM as experimental implementation of RCS in determining accurate structures of medium-sized molecules without dipole moment, the study of cyclohexane also details the comparison of the experimentally determined rotational constant B_0 , with that obtained from high-level *ab initio* calculations. The theoretical calculations, which were carried out at both the second order Møller-Plesset (MP2) and coupled-cluster with single, double, and triple perturbative substitutions (CCSD(T)) levels of theory also takes into account zero-point vibrational averaging effects. A detailed investigation of the vibrational averaging effects reveals that the corrections emerge from only the six highly symmetric A_{1g} modes, a justification of which is provided by an analysis of these modes.

4.2 Benzene and perdeutero-benzene

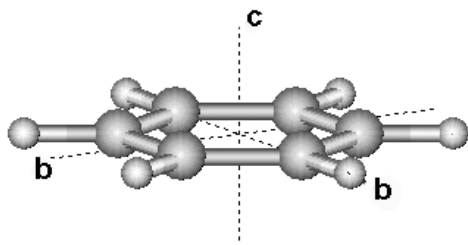


Fig.4.1 Schematic view of benzene (C_6H_6) structure with principal axes of inertia.

Benzene (Fig. 4.1) has been long time the subject of extensive spectroscopic studies as it is a prototype aromatic molecule. The first high-resolution rotational Raman spectra of benzene and benzene- d_6 were measured by Stoicheff [Sto54]. The data obtained were used to calculate the moment of inertia and precise C-C and C-H bond lengths in the benzene molecule.

Later high-resolution rotation-vibration Raman spectra of benzene vapour were studied by Hollinger and Welsh using laser excitation [HoW78]. A recent summary of the spectroscopic results on benzene can be found in the work of Hese and co-workers [OMH99]. Experimental methods applied involve high-resolution IR spectroscopy for the electronic ground state and rotationally resolved UV spectroscopy for the electronically excited state.

Neusser and co-workers applied ns-DFWM in the frequency domain yielding for the first time a sub-Doppler DFWM spectrum of a polyatomic molecule [HNN96]. Riehn *et al.* measured RCS spectra of benzene in both the ground and the electronically excited state using TRFD [RWB01]. Precise rotational constants with a relative uncertainty on the order of 10^{-5} for benzene in the ground and electronically excited state were obtained.

The first time-resolved coherent Raman experiment on benzene in the gas phase has been reported by Hayden and Chandler [HaC95]. They have monitored the dephasing of the initial coherence up to a time delay of 14 ps. Later these results were confirmed by Kiefer and co-workers [RSK98]. Recently, the early time response of benzene (up to 100 ps with 50 fs laser pulses) has been investigated by Dantus and co-workers [BZD99, Dan01]. From a simulation a rotational constant B_0 of $0.1897 \pm 0.0002 \text{ cm}^{-1}$ has been inferred.

The benzene molecule is an oblate symmetric top of point group D_{6h} . For the common assumption of molecular planarity in the ground state the relationship $B = 2C$ between the rotational constants is obtained. This is an approximation within the limits of the inertial defect, which is about 0.05 u A^2 for benzene [OMH99]. In previous RCS studies [RWB01], recurrences of the ground state rotational coherences were observed every 43.9437

± 0.0022 ps with strong even and weaker odd J-type transients. The J-type transients appeared at $t_J = n/(4B)$, $n = 1, 2, \dots$. Due to the symmetry of benzene they were superimposed by K- and C- type transients at $t_C = t_K = n/(2B)$, resulting in an alternation of transient intensity. The measured recurrences correspond to a rotational constant of $B_0 = 5689.10 \pm 0.13$ MHz, in very good agreement with high-resolution results reported in the frequency domain [OMH99].

4.2.1 Benzene and perdeutero-benzene in a gas cell at room temperature

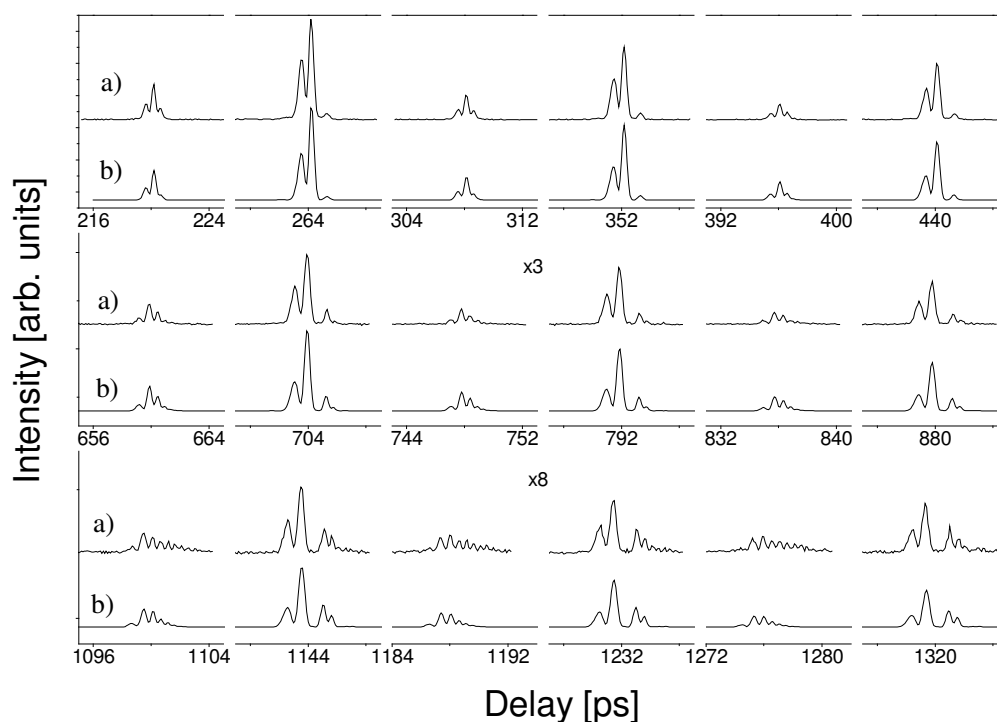


Fig. 4.2 Structure of transients in a fs DFWM spectrum of benzene in a gas cell (298K).

- a) Experimental spectrum.
- b) Fitted simulation of the spectrum (values for parameters, see Tab. 4.2).

In the experiments at room temperature, a cell was filled with the sample gas (298K) at reduced pressure ~ 5 mbar. RRs have been obtained up to 1.6 and 1.2 ns for benzene and benzene- d_6 respectively. The decay of the RRs is mainly determined by the collisions

between the molecules. In order to get precise information, time windows of 10 - 12ps were scanned around the transients with a step size of 0.1ps. The experimental spectra were recorded with a laser pulse energy not higher than 90 μ J. Due to high signal-to-noise ratio of the fs DFWM spectra, smoothing or filtering of the raw data was not necessary.

Fig. 4.2, trace a) shows several magnified recurrences measured for benzene in the gas cell in the region from 200 ps up to 1330 ps. The transients occur at a time period of ≈ 43.9 ps with alternating intensity and were assigned to J-type transients of an oblate symmetric rotor. Thus, their position in time is given by $t_J^{cell} = n/(4B)$ (see above), with recurrence number $n = 1, 2, 3, \dots$ and rotational constant B in Hz. The alternation in intensity of RRs can be rationalized by the fact that half recurrences (weak, odd numbered) are a result of beating of frequencies in S branches $|\Delta J|=2$ (Eq. 2.10), whereas the full recurrences (strong, even numbered) result from beating of different frequencies in both S and R branches (Eqs. 2.9, 2.10). It also can be seen from the simulation based on the equation 2.36.

At short time delay the transients show a pronounced double-peak structure with some smaller wings. This structure is becoming more and more complicated with increasing time delay. As will be shown in Section 4.2.3 this modulation is caused by the contribution from the CD terms, which cannot be neglected for molecules at high temperature (298K). It follows clearly that a simple linear regression analysis of the recurrence times, i.e., an analysis of peak center position in time versus recurrence number using the relation given above for t_J^{cell} is not useful. It would result in an effective rotational constant B_{eff} that is too small due to the influence of CDs. For example, one finds that RRs of benzene are separated in time with the averaged period $t_J^{cell} = 43.972$ ps. The corresponding value of the rotational constant $B_{eff} = (4t_J^{cell})^{-1} \approx 5685.4$ MHz is obviously smaller than the values reported in literature by Juntilla and coworkers ($B=5689.3$ MHz, Ref. [JDF91]). Only a complete fit of the fs DFWM spectrum based on a simulation procedure gives the correct value for the rotational constant B_0 . From such a fitting procedure the values for the CD constants D_J and D_{JK} have also been obtained (see Tab.4.2). Fig. 4.2b shows a simulated spectrum fitted to the experimental data. A nonlinear least-squares fitting procedure based on the simulation of the fs DFWM spectrum using Eq. 2.36 was employed. The fitting parameters were the rotational constant B , the CD constants D_J and D_{JK} , the temperature T , the external dephasing time τ , a time shift of all transients and a scaling factor for the total intensity of the fs DFWM signal.

Table 4.1: Nuclear spin statistical weights for benzene, perdeutero-benzene and cyclohexane. Adapted from Ref. [Web80].

Molecule	Point-group	K = 0		K > 0
		J = even	J = odd	
Benzene ($^{12}\text{C}_6\text{H}_6$)	D_{6h}	7	3	10, 11, 9, 14, 9, 11
Benzene-d ₆ ($^{12}\text{C}_6\text{D}_6$)	D_{6h}	92	38	130, 116, 124, 119, 124, 116
Cyclohexane ($^{12}\text{C}_6\text{H}_{12}$)	D_{3h}	720	656	1376, 1360, 1360

The nuclear spin statistical weights of rotational levels were also included in the simulation of the symmetric top's fs DFWM spectra. An example of the influence of the nuclear spin statistical weights on the RCS spectrum of oxygen was considered in Section 2.1.6. In Table 4.1 the values of the nuclear statistical weights for molecules, which will be analyzed in this chapter, are given. The weights for the rotational levels of these molecules are not differing so much from state-to-state like in the case of oxygen. The simulations of the fs DFWM spectra of benzene and cyclohexane show that the nuclear spin statistics have very little effect on the shape of the transients.

Table 4.2: Results for fs DFWM experiments of benzene (C_6H_6) for the ground state: rotational constants (in MHz) and CD constants (in kHz), fitting parameters, recurrence times and data from the literature.

	Fs-DFWM (this work)			TRFD [RWB01]	Ref. [JDF91]	Ref. [DJP91]
	Gas cell	Supersonic jet				
	Fitting data	Lin. Regression	Fitting data			
B	5688.95 ± 0.55	5688.54 ± 0.08	5689.25 ± 0.11	5689.10 ± 0.28	5689.278(1) ^{a)}	5689.241 (13)
D_J	1.1 ± 0.2		$1.1^{\text{b)}$		1.24(1)	1.48(9)
D_{JK}	-1.4 ± 0.4		$-1.4^{\text{b)}$		-2.06(2)	-2.53(20)
t_j [ps]		43.9480 ± 0.0006		43.9437 ± 0.0022		
Temp. [K]	301 ± 27		30 ± 2			
τ [ps]	440		2780			

^{a)} Uncertainties in parentheses are one standard deviation (1σ)

^{b)} Fixed.

The comparison of the fitted (Fig. 4.2b) with the experimental spectrum (Fig. 4.2a) shows that the position, shapes, and relative intensities of the transients are simulated very well up

to 1.3 ns. The resulting values of B , D_J , and D_{JK} for benzene are summarized in Table 4.2 and compared to the literature data [OMH99, RWB02, JDF91, DJP91].

The error analysis was performed by a systematic variation of one parameter. From that a reduced $\Delta\chi^2/\chi^2_{min} = 2\%$ error margin was calculated and reported as an uncertainty σ with a high level of confidence (>95%) [RWL00, JMR03, RMJ03]. This procedure has been used in error analysis of all measurements presented in this work.

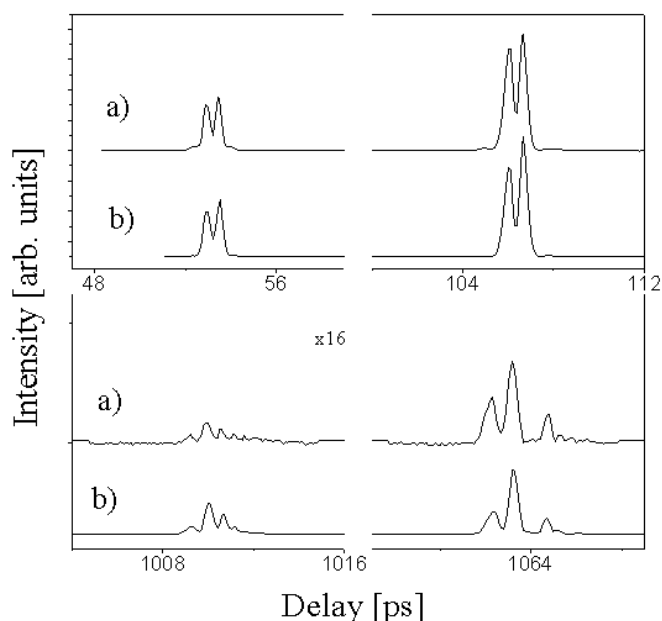


Fig. 4.3 Selected magnified transients (J-type) of benzene-d₆ (C₆D₆) from fs DFWM spectroscopy in a gas cell (298K).

a) Experimental spectrum.

b) Fitted simulation of the spectrum (values for parameters, see Tab. 4.3).

Table 4.3: Results for fs DFWM experiments of benzene-d₆ (C₆D₆) for the ground state: rotational constants (in MHz) and CD constants (in kHz), fitting parameters, recurrence times and data from the literature.

	fs DFWM (this work)			High-resolution IR Ref. [PVC89]
	Gas cell	Supersonic jet		
	Non-linear fitting	Linear regression ^{a)}	Non-linear fitting	
B	4706.4 ± 0.3	4706.68 ± 0.09	4707.23 ± 0.12	4707.312 ± 0.104
D_J	0.41 ± 0.04	--	0.749^b	0.749 ± 0.068
D_{JK}	-0.22 ± 0.30	--	-1.251^b	-1.251 ± 0.224
t_j [ps]		53.116 ± 0.001		
Temp. [K]	310 ± 30		41 ± 3	
τ [ps]	354		2910	

Uncertainties represent 2σ standard deviation.

^{a)} CD not included. Only peak center positions used.

^{b)} Fixed for the simulation. Values taken from Ref. [PVC89].

The transients of perdeutero-benzene appear in the fs DFWM trace with a periodic spacing of ~ 53.2 ps. The RRs of C_6D_6 also exhibit a time-dependent structural modulation (see Fig. 4.3). Again, the position and structure of the RRs is reproduced well by the fitted simulation. The rotational and the CDs constants (see Tab. 4.3) are comparable to the results of rotationally-resolved IR spectroscopy [PVC89].

In general, there is a bias of gas cell experiments to deliver rotational constants that are systematically too small, which could be attributed to a small contribution of vibrationally excited states populated at room temperature. This behavior was found also for C_6H_6 (see Tab. 4.2) and seems to be more pronounced for C_6D_6 , due to its lower frequency vibrational levels.

The fs DFWM spectrum of C_6D_6 is apparently (see Table 4.3) not very sensitive to D_{JK} , so that only its order of magnitude could be determined. D_J could be determined with higher accuracy, but its value is clearly shifted from the literature values. The difficulties in determination of the CD constants also could arise from the contributions of vibrationally excited states to the fs DFWM spectrum measured at room temperature.

4.2.2 Benzene and perdeutero-benzene in a seeded supersonic jet

For obtaining a seeded supersonic jet expansion, a piezoelectric, pulsed nozzle (repetition rate: 1 kHz, diameter: 0.5 mm) was employed (see section 3.3.1). In order to saturate the gas phase with the sample's vapour pressure, helium (stagnation pressure: 1 bar) was bubbled through the liquid samples at room temperature, (298 K) before the nozzle expansion. The fs DFWM traces of molecules in the seeded supersonic jet were measured with a step size in time of 0.2 ps. The spectra were recorded with a typical energy of 120 μ J per pulse.

The fs DFWM spectra of C_6H_6 and C_6D_6 under supersonic jet expansion have several common features. First, the temperature is significantly reduced (20-40 K), so that the influence of CD is minimized. Second, in this collision-free environment the collisional dephasing is negligible on the time-scale of observation. The measurements were limited to a maximum of 4 ns, due the length of the delay line. The signal-to-noise ratio of $10^2 - 10^3$ is comparable to that obtained in the gas cell experiment. Because of that no smoothing or filtering of the raw data were applied.

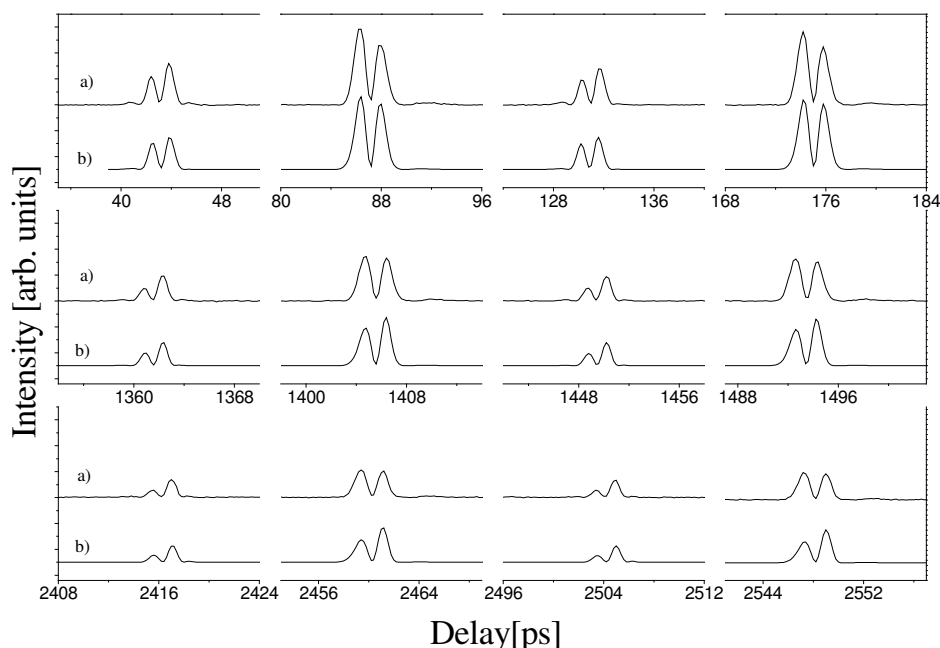


Fig.4.4 Structure of transients in fs DFWM spectrum of benzene in a supersonic jet (30K).

- a) Experimental spectrum.
- b) Fitted simulation of the spectrum (values for parameters, see Tab.4.2).

The fs DFWM traces of benzene and benzene- d_6 show again RRs with strong even and weak odd numbered J-type transients. Every recurrence has a pronounced double-peak structure up to 3.9 ns with some weaker modulations in the wings (Figs. 4.4, 4.5). The decay time of the recurrences is much longer than that for the cell experiment due to the absence of collisions in the jet. This is illustrated by the values of the decay parameter τ - the external dephasing time (see Eq. 2.36). For the spectra of hydrogenated benzene a value of $\tau = 2780$ ps was determined, whereas for the gas cell experiment $\tau = 440$ ps was obtained. Therefore a significantly higher precision of the rotational constant can be obtained from the supersonic jet spectrum (see Tabs. 4.2 and 4.3).

Two methods of analysis for the recorded fs DFWM supersonic jet spectra have been employed. The first was a linear regression analysis of the transient peak positions assuming that at low temperature the contribution of the CD can be neglected. For the second approach a numerical simulation of the fs DFWM trace was used.

In the linear regression analysis the peak positions were determined for all available J-type recurrences (87 for C_6H_6 and 72 for C_6D_6), which have been measured. The minimum between the two peaks of a particular recurrence as its position in time was used. From the

linear regression analysis of the peak position versus recurrence number the values of $t_J = 43.9480 \pm 0.0006$ ps and $t_J = 53.116 \pm 0.001$ for benzene and benzene-d₆ respectively were obtained, where the error margins correspond to the statistical error of the linear regression procedure. The corresponding values of the rotational constants $B_0 = 5688.54 \pm 0.08$ MHz and $B_0 = 4706.68 \pm 0.09$ (see Tabs. 4.2 and 4.3) are smaller than the rotational constants obtained from a complete fitting of the same fs DFWM spectra. Thus, it can be concluded, that even under supersonic jet conditions the CD terms cannot be completely neglected. This can be demonstrated by fitting of the fs DFWM traces neglecting CD constants (D_J , D_{JK}), which gives a rotational constant of $B_0 = 5688.5$ MHz for hydrogenated benzene similar to the linear regression result. However, this type of analysis is additionally listed for analysis of the spectra from symmetric tops, since it provides a very simple approach towards ‘relatively’ precise rotational constants without complete simulation of the fs DFWM spectra.

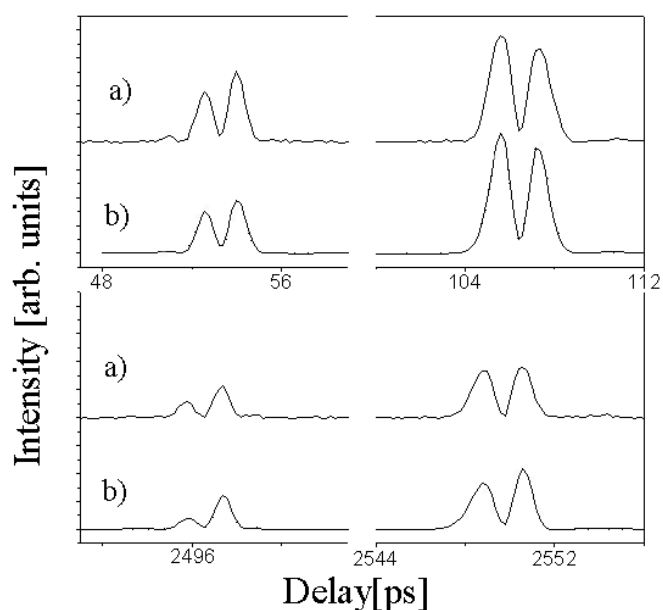


Fig. 4.5 Selected magnified transients (J-type) of benzene-d₆ from fs DFWM spectroscopy in a supersonic jet.

- a)** Experimental spectrum.
- b)** Fitted simulation of the spectrum (values for parameters, see Tab. 4.3).

In order to obtain the correct rotational constants B from the spectra recorded under supersonic jet conditions, a complete fitted simulation of the fs DFWM spectra was performed. Since the fitting was not very sensitive for the CD constants, D_J and D_{JK} , they were not varied. Figs. 4.4 and 4.5 (trace a) shows several enlarged experimental transients in comparison to those obtained from the fitted simulation (trace b). The simulation reproduces the position, shape and width of the transients very well. The values of the fitting parameters are given in Tables 4.2 and 4.3.

There are some small differences between experimental and fitted data, mainly concerning the ratio of the peaks of the recurrences. These differences were rationalized as perturbation of fs DFWM spectra by high laser intensity. For the supersonic jet experiments it was necessary to use relatively high laser intensity ($\sim 10^{12} \text{ W cm}^{-2}$) in order to compensate for the low number density of the sample in the beam. The inclusion of the high laser field distortions in the simulation of the fs DFWM spectra will be considered in Section 4.2.4.

4.2.3 Influence of the centrifugal distortions

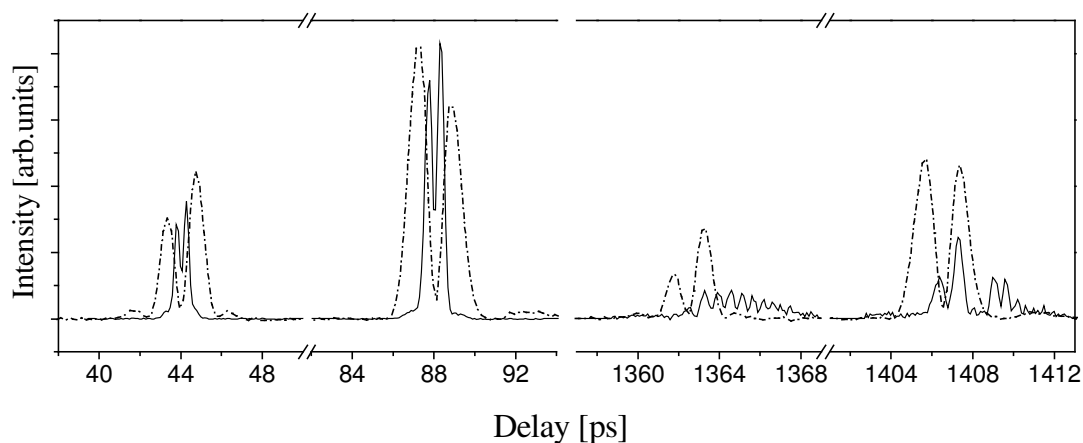


Fig. 4.6 Comparison of fs DFWM signal of benzene in a cell (solid line) and in a seeded supersonic jet expansion (dotted line).

Note: The transients from the cell experiment in the region 1360-1412 ps are magnified 8 times.

By comparing the fs DFWM traces from the supersonic jet and the gas cell the influence of the CD can be directly assessed. Fig. 4.6 shows the comparison of the fs DFWM signal of benzene in a cell (solid line) and in a seeded supersonic jet expansion (dotted line).

Clearly, the spectra are affected in two ways. First, the peak positions are shifted towards longer times in the gas cell experiment. Second, the recurrences for the high temperature experiment show a strong modulation or splitting, which is mainly ascribed to the CD terms. Moreover, since the width of the transients is proportional to $1/(B \cdot T)^{1/2}$ [FeZ95a], the recurrences measured in the supersonic jet (30 K) are broadened by approximately a factor of three compared to those measured in the gas cell at room temperature (298 K).

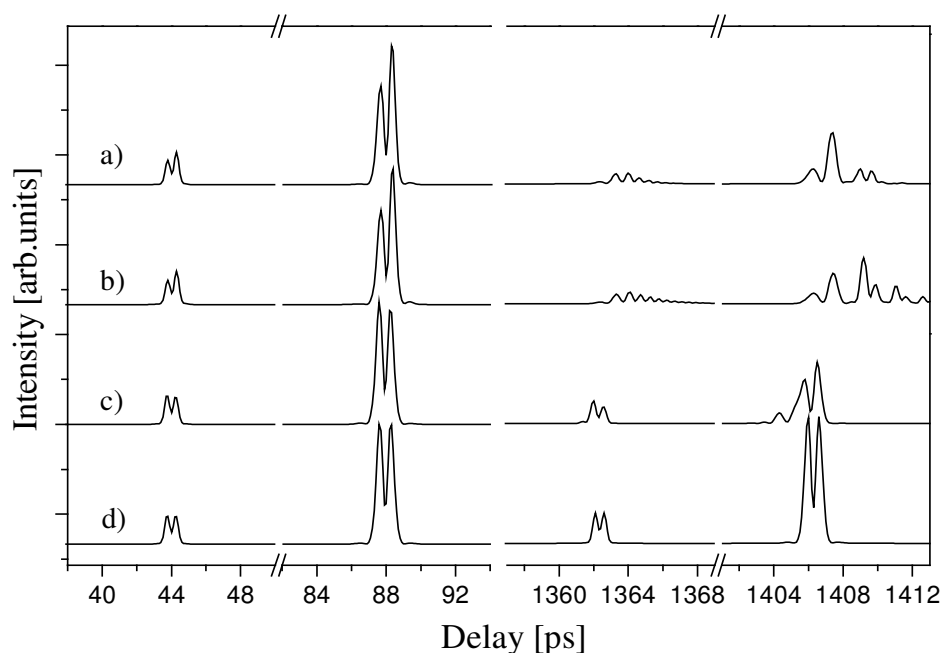


Fig. 4.7 Illustration of centrifugal distortion influence on fs DFWM spectrum by simulated spectra. The set of parameters corresponds to benzene at room temperature (298K).

- a) Simulation with the parameters outlined in Tab. 4.2. ($B = 5688.95$ MHz; $D_J = 1.1$ kHz; $D_{JK} = -1.4$ kHz)
- b) $D_{JK} = 0$. All other parameters as in a).
- c) $D_J = 0$. All other parameters as in a).
- d) $D_J = 0$ and $D_{JK} = 0$. All other parameters as in a).

One can also use the numerical simulation to examine the influence of CD on fs DFWM spectra. Fig. 4.7 shows the dependence from CD constants at short delay time and at relatively long time delay ~ 1.4 ns. Examination of the traces at short time delay reveals that in this region the influence of CD is rather very weak. One can only note a difference in the intensities of the peaks of the RRs. However, a stronger influence of the CDs can be seen at longer time delay. From comparison of the traces a) and d) ($D_J = D_{JK} = 0$) in Fig. 4.7 it can be seen that CD affects RCS spectra in two ways. First, a shift in peak positions towards longer times is observed. Second, pronounced structural modulations appear. Both effects were found also in the experimental spectra (see above Fig. 4.6). The D_J and D_{JK} constants distinctly influence the simulated spectra (see Figs 4.7b,c). First, due to their different signs D_J (positive) provides a shift of the recurrences towards longer times whereas D_{JK} (negative) provides an opposite shift but smaller in magnitude. Even more important is their influence on the transient's structure. While D_J is responsible for the appearance of the pronounced modulation of the even numbered transients and the splitting of the odd

numbered ones, D_{JK} affects the asymmetry and the damping within the structure of a particular transient.

In order to demonstrate how well our approach for calculation of CD induced corrections to the periods of RRs (Section 2.2.5) works, it is applied here to the experimental data for benzene. The J type transients obtained at room temperature have an averaged period of $t_J^{cell}=43.972$ ps (see Section 4.2.1). If one takes the best fit values of the rotational constant and CDs (see Tab. 4.2) and calculates the RRs period for a planar symmetric top according to Eqs 2.28 and 2.29, the result will be 43.986ps. Since the laser pulse duration in the experiment was approximately 150 fs and the scanning step was 100 fs, this is in reasonable agreement.

It should be noted that the period of RRs from a molecular beam experiments t_J obtained from linear regression analysis is also affected by the CDs (see Section 4.2.2). Indeed, if one takes the best fit values of the rotational constants and CDs (Tab. 4.2) for benzene in the supersonic jet and calculates the J transient period according to the equations 2.28, 2.29 in Section 2.2.5, one obtains the value of t_J^{jet} reported above for a temperature of $T_{jet}=39$ K. This value is in good agreement with the temperature obtained from the complete fitting of the fs DFWM spectrum of benzene in a seeded molecular beam. Therefore, the present theory can be invoked for the estimation of the CDs from the experimental data, provided the rotational constants of the molecule of interest are known, and also the positions of the first few RRs are available [GRM03].

4.2.4 Dependence of fs DFWM spectra on laser intensity

It was noticed for fs DFWM spectroscopy that a change in the shape of the rotational transients occurs with increasing laser intensity [CPD00, MJR02, RMJ03]. The physical effects behind this spectral perturbation depend on the optical field strength and can range from active alignment [PPB03] over molecular deformation to field ionization [CSD03].

In order to evaluate how a high intensity laser field affects the shape of the rotational transients, the first 180 ps of the spectrum of benzene in molecular beam were recorded for different laser energies (Fig. 4.8(I)).

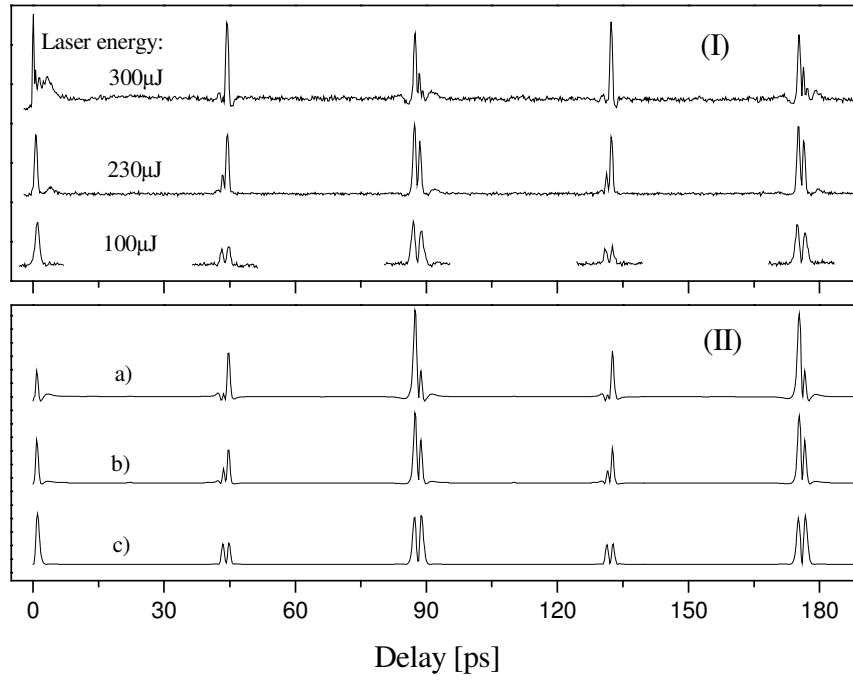


Fig. 4.8 (I) Dependence of fs DFWM spectrum of benzene on the energy of laser pulses. (seeded supersonic jet).
(II) Simulations for different values of the background parameter k . Traces **a)**, **b)**, **c)**, for $k = 0.2, 0.1$ and 0 which correspond to laser energies 300, 230 and 100 μJ , respectively.

As a parameter the total energy for all three laser beams, i.e., the energy of the laser beam before splitting it up into the pump and probe beams, was measured. From Fig. 4.8(I) it can be seen that there is a gradual change in the structure of the RRs from the double-peak shape at 100 μJ towards a single peak shape at 300 μJ . The original double-peak structures suffer a reduction of the spike at short (long) time delay for the odd (even) numbered recurrences. Moreover, a new, broad feature appears on the short (long) time delay side for the odd (even) numbered recurrences and a constant background signal emerges.

In order to describe the fs DFWM signal for an intensity regime in which spectral perturbation just sets in [MJR02, JMR03, RMJ03], a coherently coupled background signal is employed by means of an extra fitting parameter k (0.0 ... 1.0) added to the sum before squaring (see Eq. 4.1).

$$I_{DFWM}(t) = I_{pr}(t) \otimes \left(I_{pu}(t) \otimes \left(k + \sum_{E_{g'} > E_g} (\rho_{g'} - \rho_g) A_{gg'} \sin(\Omega_{gg'} t) \right) \right)^2 e^{-t/\tau} \quad (4.1)$$

Here the Eq. 4.1 is analogous to Eq. 2.36 and all variables are defined in Section 2.4.3.2.1. In Refs. [MPH93, LFM00] a mixture of homodyne and heterodyne signal detection was calculated in an equivalent way. To be correct, some effective value k must be considered, which depends on the concrete molecule and the sample number density.

The simulated spectra obtained in this way are depicted in Fig. 4.8 (II). For comparison, in trace c) a simulation with the parameter k set to zero is depicted. Upon increasing its value to $k = 0.1$ an asymmetric distortion of the double-peak structures of the recurrences appears (Fig.4.8(II), trace b)), reproducing the effects observed for the experimental spectra quite nicely. Also, the smaller features in the wings of the transients are matched in the simulated traces. However, a difference concerning the alternation in intensity for even and odd numbered transients remains.

With $k = 0.2$ (Fig.4.8(II), trace a)) the transients appear as single peaks. The simulations with $k = 0, 0.1$ and 0.2 can be compared to the experimental spectra with 100, 230 and 300 μJ , respectively. This quantitative approach has been used for analysis of several fs DFWM molecular spectra in order to account for the spectral perturbation by high laser intensity. It improves the reproduction of experimental data and automatically increases the quality of the extracted information. It should be noted that the structural perturbations of the recurrences induced by the increasing laser intensity could not be fitted or reproduced by a change of the rotational or the CD constants within the assumption of a symmetric rotor structure [JMW02, MJR02, JMR03].

4.3 Cyclohexane

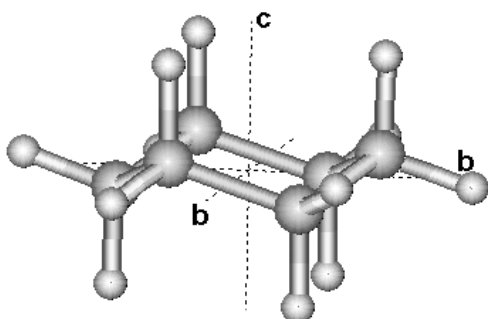


Fig.4.9 Schematic view of cyclohexane (chair conformation; C_6H_{12}) structure with principal axes of inertia.

Cyclohexane (C_6H_{12}), which is one of the smallest saturated cyclic hydrocarbons has been the focus of a large number of structural investigations [DaH63, AlK63, GBM71, PWW73, BFS73, EKS76, Wib83, LMB94]. Both experimental and theoretical investigations concur that the chair conformer of cyclohexane (Fig. 4.9) is the predominant geometry at room temperature, with the chair conformer being about 8.1 (6.6) kcal/mol more

stable than the corresponding boat (or twisted boat) conformation [LMB94]. Since the pioneering work of Davis and Hassel [DaH63], there have been several attempts to obtain the structural characteristics of this chair conformer. The most recent estimates of the cyclohexane C-C bond length of $1.536 \pm 0.002 \text{ \AA}$ (r_g) [BFS73] and $1.535 \pm 0.002 \text{ \AA}$ (r_g) [EKS76] indicate that they are close to the standard value for an unconstrained C-C bond, to be precise, that of ethane ($1.5351 \pm 0.0001 \text{ \AA}$, r_2) [HES81].

Since cyclohexane in the chair conformation belongs to the point group D_{3d} , it is not possible to employ microwave spectroscopy. However several diffractive and spectroscopic methods were employed in the past to obtain information on cyclohexane geometry [DaH63, AlK63, GBM71, PWW73, BFS73, EKS76]. Peters et al. carried out a rotational Raman study and obtained a value of the rotational constant $B_0 = 4299.89 \pm 0.06 \text{ MHz}$ (cyclohexane is an oblate symmetric top, where the following relation for the rotational constants holds: $A = B > C$) and the CD constant $D_J = 0.468 \pm 0.009 \text{ kHz}$ [PWW73]. Using these values and a simplified r_0 model, the C-C bond length and $H_{eq}CH_{ax}$ angle was found to be $1.535 \pm 0.001 \text{ \AA}$ and $110.0 \pm 0.3^\circ$, respectively. Later, utilizing the fact that unsymmetrically deuterated isotopomers of cyclohexane exhibit a small permanent dipole moment, Dommen et al. determined the precise rotational and CD constants of five isotopomers by Fourier-transform microwave spectroscopy, and consequently obtained a complete substitution structure (r_s) for cyclohexane [DBG90]. Bialkowska-Jaworska et al. used these results and obtained an improved r_0 structure ($B_0 = 4305.84(15) \text{ MHz}$ and $C_0 =$

2463.34(6) MHz) for pure cyclohexane by fitting it to the moments-of-inertia of all five isotopomers of the work of Dommen et al. [BJK95].

4.3.1 Cyclohexane in a gas cell at room temperature and in a seeded supersonic jet

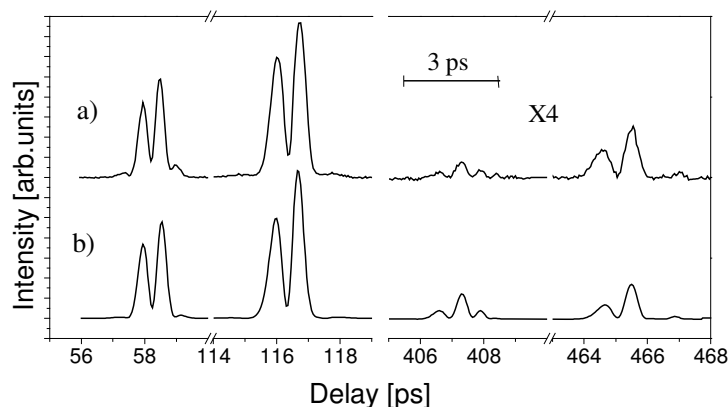


Fig. 4.10 Selected transients from the fs DFWM spectrum of cyclohexane in the gas cell (25mbar, 298K).

- a) Experimental spectrum.
- b) Fitted simulation (parameters given in Table 4.4).

Please note the different time scales in Figures 4.10 and 4.11. A 3 ps ruler is depicted for comparison.

In the gas cell the fs DFWM spectrum was recorded up to 700 ps in steps of 0.2ps. Scans around the RRs (ca. 5 ps wide) with a step size of 0.05 ps have been additionally recorded. A reduced pressure (~25mbar) of cyclohexane vapor was used in the gas cell experiments. For the non-linear fitting analysis 10 transients in the region up to 700 ps have been considered. Some selected transients are given in Fig. 4.10a in comparison to the fitted simulation (Fig. 4.10b).

The fs DFWM spectrum in the supersonic expansion was measured in two regions (0 – 350, 1300 – 1650ps) with a step size of 0.2ps. The seeded supersonic expansion was generated from helium as carrier gas (1 bar stagnation pressure) and cyclohexane held at room temperature (vapor pressure ≈130 mbar). This gas mixture was expanded into the vacuum by a home-built piezoelectric nozzle (diameter 0.5 mm) operated at 1 kHz repetition rate. For the nonlinear fitting analysis 12 transients have been considered.

All presented spectra for cyclohexane were taken at low enough laser intensity, so that the extra fitting parameter k (see section 4.2.4) was not necessary.

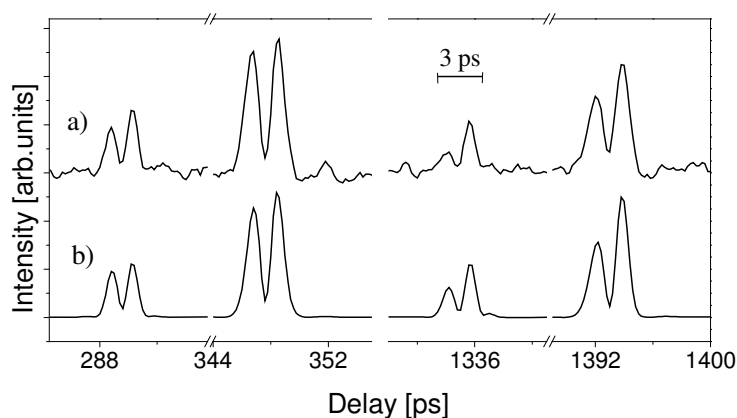


Fig. 4.11 Selected transients from the fs-DFWM spectrum of cyclohexane in the supersonic jet (45K).

- a) Experimental spectrum.
- b) Fitted simulation (parameters given in Table 4.4).

Table 4.4: Results for fs DFWM experiments on cyclohexane for the ground state: rotational constants (in MHz) and CD constants (in kHz), fitting parameters, recurrence times and data from the literature.

	fs DFWM (this work)			Ref. [PWW73]	Ref. [BJK95]
	Gas cell	Supersonic jet			
	Non-linear fitting	Linear regression ^{a)}	Non-linear fitting	Rotational Raman	Microwave (struct. fit)
B	4303.22±0.39	4305.14±0.33	4305.44±0.25	4299.89±0.06	4305.85(15)
D _J	0.51±0.10	--	0.51 ^{b)}	0.468±0.009	0.91 ^{c)}
D _{JK}	-0.29±0.81	--	-0.29 ^{b)}		-1.33 ^{c)}
t _J [ps]		58.0699 ± 0.0022			
Temp. [K]	287±29		45±4	298	220

Uncertainties in parentheses are one standard deviation (1σ). Uncertainties given with $a\pm b$ represent two standard deviations (2σ).

^{a)} Centrifugal distortion not included. Only peak center positions used.

^{b)} Fixed for the simulation. Values obtained from the gas cell experiment.

^{c)} Δ_J and Δ_{JK} reported. No uncertainties given.

Fig. 4.11a shows some selected transients from the fs DFWM spectrum of cyclohexane in the supersonic jet with comparison to a fitted simulation (Fig.4.11b). The fitting results for both the gas cell and the jet data, including the nuclear spin statistics weights from Tab. 4.1

are summarized in Table 4.4. Also, the results obtained by linear fitting of the supersonic jet data, i. e., by neglect of the CD, are listed.

In comparing the different values from Table 4.4, one can clearly see that *all* B_0 values obtained from the fs DFWM experiment are larger than the one formerly reported from Raman spectroscopy by +0.1% [PWW73]. From all three evaluations of the fs DFWM data, the result from the cell experiment gives the smallest value for this constant.

The value deduced from the supersonic jet experiment after analysis by non-linear fitting is recommended as new, reliable rotational constant $B_0 = 4305.44(13)$ MHz for cyclohexane. This value is in good agreement with the calculated constant of Ref. [BJK95] (see Table 4.4). The value for B_0 is significantly shifted (+5.5 MHz) from the one reported in the former Raman investigation by Peters et al [PWW73]. Since only room temperature experiments have been performed in Ref. [PWW73], the contribution of vibrationally excited levels cannot be ruled out. Moreover, the analysis of the R and S branch gave drastically different rotational and CD constants, so that eventually only the S branch results were reported, a sign for some experimental inconsistency Ref. [PWW73]. However, it is difficult to ascertain the source of error. If one considers the B_0 values for C_6D_{12} , a similar shift between the results reported in Ref. [PWW73] and Ref. [BJK95] is noted.

The CD constants determined in this work could only be deduced from the gas cell data and are reported tentatively and with relatively large error bars (Table 4.4). Compared to the investigation on benzene (section 4.2), these large uncertainties can be explained by the relatively small third-order susceptibility of cyclohexane ($\chi^{(3)} \approx 6.5 \times 10^{-14}$ esu, Ref [KaM85]), which leads to a weak Raman scattering signal. Hence, compared to benzene a higher concentration of cyclohexane in the gas cell was necessary for the measurements, which in turn limits the maximum time window due to collisional dephasing (0.7 ns for cyclohexane vs. 1.6 ns for benzene) and RRs at larger delay time could not be examined [RMJ03].

4.3.2 Comparison of the experimental results with *ab-initio* calculations

4.3.2.1 Computational details

The equilibrium structure of cyclohexane (Fig. 4.9) was evaluated using calculations carried out at both the second order Møller-Plesset (MP2) and the coupled-cluster with single,

double, and perturbative triple substitutions [CCSD(T)] levels of theory [MøP34, RTP89, Bar89]. Both the Gaussian-98 and ACES II programs were used to carry out the geometry optimizations [Gau98, ACEII].

Two different approaches have been employed to obtain the magnitudes of the rotational constants at the complete basis set (CBS) limit [FeD01, PWD94, HKK97]. These approaches have earlier been employed to estimate the equilibrium bond lengths, and harmonic vibrational frequencies at the CBS limit. Thus in the first approach [FeD01, PWD94], the estimated value of the physical parameter “ F ” under consideration at the CBS limit, can be obtained by employing Eq. 4.2.

$$F(X) = F(\infty) + Y \cdot \exp[-(X-1)] + Z \cdot \exp[-(X-1)^2] \quad (4.2)$$

In Eq. (4.2), X is the cardinal number of the basis set (2, 3, 4, for VDZ, VTZ, and VQZ sets, respectively). $F(\infty)$ is the estimated CBS limit as $X \rightarrow \infty$. The values of F , Y , Z , can be easily obtained, since there are three unknowns and three equations. In a second simpler approach [HKK97], the value of “ F ” at the CBS limit can be obtained by employing Eq. 4.3.

$$F(X) = F(\infty) + Y \cdot X^3. \quad (4.3)$$

While it is advantageous to use Eq. 4.3, because it involves the evaluation of only two variables, and hence requires only two values, the rotational constants have been evaluated at the CBS limit using Eq. 4.2, because the mixed exponential/Gaussian function form was often found to yield better agreement with experiment [when $X=2$ (VDZ), 3 (VTZ), 4 (VQZ)] than simple exponential or Gaussian forms [FeD01, PWD94].

It is well known that vibrational anharmonic effects have substantial contributions to the rotational constants [BGJ01, CAR88, ÅRT00, RÅT00]. Therefore, an effective comparison of the experimentally determined rotational constants to the theoretically evaluated numbers is only feasible when vibrational anharmonic effects are explicitly taken into account, when evaluating the latter. Till a few years back, the evaluation of vibrational anharmonic effects was limited to very small molecules because the computationally arduous cubic and quartic force constants [CAR88], have to be calculated to obtain the magnitude of the vibrational anharmonic effects. However, it has recently been shown that these vibrational anharmonic effects can be easily obtained from only the cubic force constants [ÅRT00, RÅT00]. Eq. 4.4 represents a mathematical expression for the evaluation of the vibrationally averaged geometries [ÅRT00, RÅT00].

$$\langle r_i \rangle = r_{e,i} - \frac{1}{4\omega_i^2} \sum_{j=1}^{3N-6} \frac{V_{ij}^{(3)}}{\omega_j^2} \quad (4.4)$$

In the above equation, $\langle r_i \rangle$ is the corrected geometry, ω_i and ω_j are the harmonic frequencies for normal modes i or j , and $V_{ij}^{(3)}$ is the cubic force field. Since the determination of the cubic force constants is a non-trivial task for the size of systems like cyclohexane, the vibrational effects have been evaluated at the Hartree-Fock HF/6-31G*, HF/cc-pVDZ, and HF/cc-pCVDZ levels. The DALTON program was used to evaluate the vibrational effects [DAL01]. A detailed analysis of the errors involved in the evaluation of the vibrational effects at both the Hartree-Fock and correlated levels of theory can be obtained from Ref. [PJO02].

4.3.2.2 Results of *ab-initio* calculations and discussion

All the *ab initio* calculations were carried out for the chair form of cyclohexane. Since this form possesses D_{3d} symmetry, it can uniquely be described by six geometrical variables. Table 4.5 highlights the variation of some of these variables and the resulting rotational constants of all the optimized structures at the MP2 and CCSD(T) levels.

The use of progressively larger basis sets resulted in an increase of the magnitude of the rotational constants at the MP2 level. This increase in the rotational constants primarily results from a decrease in both the C-C and C-H bond lengths because there are little changes in the magnitudes of the intramolecular angles. Given the size of cyclohexane and the number of variables needed to describe it, it was impossible to carry out the geometry optimizations at the CCSD(T) level using the larger CCSD(T)/cc-pCVTZ and CCSD(T)/cc-pVQZ basis sets. However, the results obtained using the cc-pVDZ, cc-pVTZ, and aug-cc-pVDZ basis sets seem to indicate that the inclusion of higher correlation effects leads to an elongation of the C-C and C-H bond lengths. Consequently, one observes that the calculated rotational constants are smaller than those obtained at the MP2 level. One can also note that the use of the core-valence basis sets leads to extremely small changes in the geometries and the rotational constants.

Table 4.5: Rotational constants, geometries, and energies of the D_{3d} conformer of cyclohexane after geometry optimization at the MP2 and CCSD(T) levels of theory and various basis sets.

MP2						
	cc-pVDZ	aug-cc-pVDZ	cc-pVTZ	aug-cc-pVTZ	cc-pVQZ	aug-cc-pVQZ
NBASIS	144	246	348	552	690	1032
A (MHz)	4304.3	4300.3	4391.4	4385.5	4391.4	4389.0
B (MHz)	4304.3	4300.3	4391.4	4385.5	4391.4	4389.0
C (MHz)	2465.6	2465.5	2515.9	2510.8	2514.7	2514.2
R_{C-C}	1.533	1.535	1.520	1.520	1.519	1.520
$R_{C-H_{ax}}$	1.107	1.106	1.091	1.093	1.091	1.092
$R_{C_{Cheq}}$	1.104	1.103	1.087	1.090	1.087	1.088
$\theta_{H_{ax}-C-H_{eq}}$	106.7	106.9	106.9	107.0	106.8	106.8
E (Hartree)	-235.097937	-235.140311	-235.426092	-235.462115	-235.577647	-235.589667
	cc-pCVDZ	aug-cc-pCVDZ	cc-pCVTZ	aug-cc-pCVTZ	cc-pCVQZ	aug-cc-pCVQZ
NBASIS	168	270	426	630	864	1206
A (MHz)	4312.0	4307.6	4372.4	4368.3	4385.7	4383.6
B (MHz)	4312.0	4307.6	4372.4	4368.3	4385.7	4383.6
C (MHz)	2470.6	2470.1	2503.8	2501.6	2511.4	2510.4
R_{C-C}	1.532	1.534	1.523	1.524	1.520	1.521
$R_{C-H_{ax}}$	1.106	1.105	1.093	1.093	1.091	1.092
$R_{C_{Cheq}}$	1.103	1.102	1.090	1.090	1.088	1.089
$\theta_{H_{ax}-C-H_{eq}}$	106.8	106.9	106.8	106.9	106.8	106.8
E (Hartree)	-235.304651	-235.346824	-235.622287	-235.639145	-235.724640	-235.731412

CCSD(T)					
	cc-pVDZ	aug-cc-pVDZ	cc-pVTZ	cc-pCVDZ	aug-cc-pCVDZ
NBASIS	144	246	348	168	270
A	4266.0	4256.1	4356.6	4272.9	4263.0
B	4266.0	4256.1	4356.6	4272.9	4263.0
C	2441.5	2437.9	2494.0	2446.0	2442.1
R_{C-C}	1.540	1.543	1.526	1.539	1.541
$R_{C-H_{ax}}$	1.110	1.109	1.094	1.110	1.109
$R_{C_{Cheq}}$	1.107	1.106	1.090	1.106	1.106
$\theta_{H_{ax}-C-H_{eq}}$	106.8	107.0	107.0	106.8	106.8
E (Hartree)	-235.203437	-235.248749	-235.535989	-235.423289	-235.457869

NBASIS is the number of basis functions; A, B, C, are the rotational constants; E, is the energy of the system in Hartrees; H_{ax} and H_{eq} , are the axial and equatorial hydrogens of cyclohexane. All distances are in units of Å and angles are in degrees.

As was mentioned earlier, the mixed exponential/Gaussian function has been used to estimate the magnitude of these rotational constants at the complete basis set limits [FeD01, PWD94]. Though the above procedure has frequently been employed to estimate the energies of the system at the CBS limit, there has been a report of a similar extrapolation procedure being employed to obtain accurate estimates of the geometries of the ammonium radical [SSS01]. Using the MP2/cc-pVxZ results, the values of $B = 4388.4$ MHz and $C = 2512.1$ MHz were obtained at the MP2/CBS limit. The use of the aug-cc-pVxZ values in the extrapolation leads to $B = 4388.4$ and $C = 2514.9$ MHz at the MP2/CBS limit. The presence of only two calculations at the CCSD(T) level prevents us from carrying out a similar extrapolation. However, an estimate of the rotational constants at the CCSD(T)/CBS limit ($B = 4350.4$ MHz and $C = 2490.3$ MHz) was obtained on the assumption that the (CCSD(T)-MP2) difference at the cc-pVQZ level mirrors the difference at the cc-pVTZ level.

Table 4.6: Correction of the calculated rotational constants by vibrational averaging.

	Uncorrected		Corrected		$\Delta(\text{HF})$		$\Delta(\text{MP2})$		$\Delta(\text{CCSD(T)})$	
	6-31G*	cc-pVDZ	6-31G*	cc-pVDZ	6-31G*	cc-pVDZ	cc-pVxZ	aug-cc...	cc-pVTZ	cc-pVXZ
A,B	4319.2	4313.8	4277.2 (4277.2)	4269.8 (4269.7)	42 (42)	44 (44)	83	83	51	45
C	2462.2	2459.9	2437.2 (2434.9)	2433.7 (2431.5)	25 (27)	26.2 (28)	49	52	31	27

The corrections are calculated on the HF/6-31G* and HF/cc-pVDZ level of theory. $\Delta(\text{HF})$ denotes the difference between the uncorrected and the corrected rotational constant. $\Delta(\text{MP2})$ and $\Delta[\text{CCSD(T)}]$ denote the difference between the rotational constants of the computational CBS limit and the experimental values. The CBS limit for the CCSD(T) calculations was estimated from the MP2 results (see text). The experimental values used are: $B_0 = 4305.44$ MHz from this work and $C_0 = 2463.34$ MHz from Ref. [BJK95].

All values are given in MHz. Values outside of parentheses are for $T = 0$ K, in parentheses for $T = 300$ K.

Compared to the experimental numbers, the above estimates of the rotational constants are clearly larger by about 80 MHz at the MP2 and about 40 MHz at the CCSD(T) level. This can be rationalized by the fact that results of the calculations are related to the minimum energy structure of cyclohexane and are therefore not corrected for zero-point vibrational effects. Hence, the CBS limit results represent the so-called ‘global minimum energy

structure', also often referred to as 'equilibrium structure', r_e . Calculations of the vibrational averaging effects require the evaluation of the cubic force constants of cyclohexane, which is computationally not feasible at the correlated levels of theory reported in this study. A number of recent high-level theoretical investigations of small molecules, like cyclopropane, benzene, and the water dimer have evaluated the magnitudes of the vibrational corrections for the equilibrium structure rotational constants [BGJ01, PJO02, GCS00, GaS00, SiS01, KMC92]. In most cases, the magnitude of this correction is around $\sim 1\%$ of the uncorrected rotational constants.

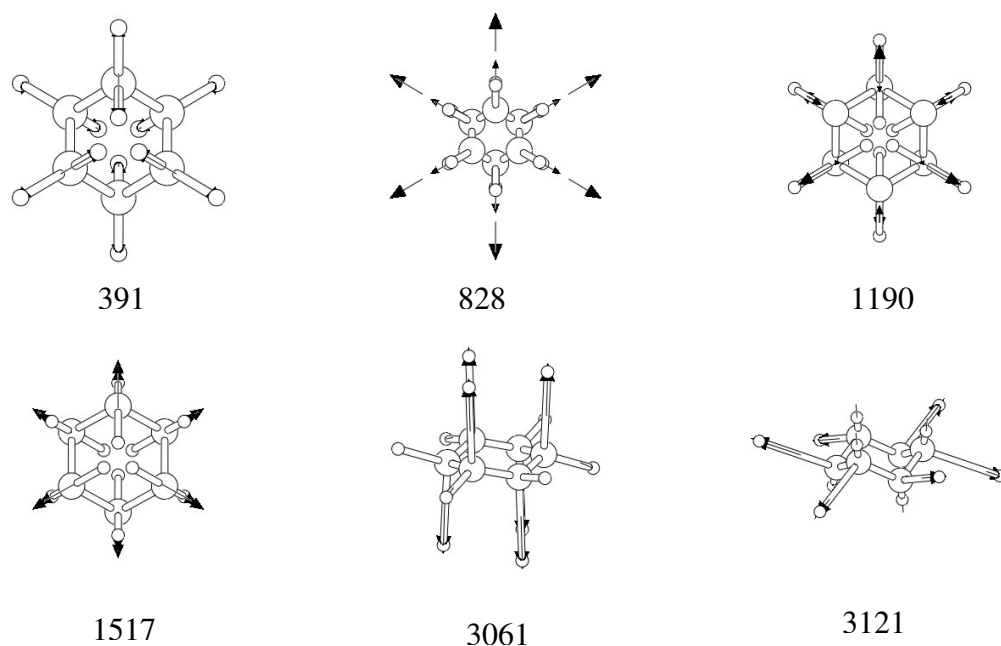


Fig. 4.12: Normal mode plots of the highly symmetric A_{1g} modes of cyclohexane, highlighting the vibrational extrema. The calculated MP2/cc-pCVTZ frequencies (cm^{-1}) of these modes are given below the plots. The normalized displacement vectors shown in the figure have been scaled by a factor of 3.5.

In order to provide an estimate for the vibrational averaging effects HF calculations using the 6-31G*, cc-pVDZ and cc-pCVDZ basis sets have been carried out using the method delineated in Refs. [FeD01, PWD94, HKK97, ÅRT00]. The results are listed in Table 4.6. A vibrational correction of ≈ 45 MHz for the rotational constant B is obtained, close to the difference between the CBS limit of the CCSD(T) calculations and the experimental values. Also, for the rotational constant C , a vibrational correction of ≈ 27 MHz is obtained, which is in close correspondence to the difference of the CCSD(T) calculation, reported here, and the value obtained by fitting the microwave data in Ref. [DBG90]. It has been pointed out

previously that the net vibrational averaging effects can be obtained to a fairly good accuracy without the inclusion of electron correlation [SiS01, KMC92, PLB83].

Interestingly, of the 48 normal vibrational modes, only the 6 highly symmetric ones (A_{1g}) are responsible for the vibrational averaging effects, which is in line with the conclusions of Salem who found that only totally symmetric modes contribute to anharmonicity [Sal69]. In order to obtain some insight on the origin of these corrections it is useful to visually examine the vibrational extremes of these 6 symmetric normal modes in Fig. 4.12. Clearly all of them exhibit significantly close atom-atom contacts as a result of displacements from the equilibrium positions. Since by definition, the magnitude of the vibration-rotation interaction constants depends on the principal component of the moment of inertia in the equilibrium geometry, the change in the magnitude of the reduced mass would significantly influence the magnitude of anharmonicity.

The calculated temperature dependence of the vibrational correction for the B constant is negligible, whereas in the experiment a shift of approx. 2 MHz was observed (Table 4.4). This could be explained by the influence of collisions on the gas cell fs DFWM spectra, which is not accounted for in our simulation model. However, for the rotational constant C , a larger change of 2 MHz was obtained from the calculations. Unfortunately, no experimental values are available for comparison.

In summary, the vibrational correction to the calculated equilibrium rotational constants of cyclohexane provides results that are close to the experimentally determined numbers. The above theoretical calculations also indicate that reliable estimates of the rotational constants can be obtained by performing geometry optimizations at correlated levels of theory and evaluating the vibrational effects at the HF level [RMJ03].

4.4 Conclusions.

Fs DFWM has been successfully applied to medium-sized molecules, such as benzene (C_6H_6), perdeutero-benzene (C_6D_6) and cyclohexane (C_6H_{12}), both in the gas cell (298K) and seeded supersonic jet (30-40K). From the comparison of the gas cell spectra and the molecular beam spectra, the influence of centrifugal distortion, collisions and temperature on the fs DFWM spectra was experimentally investigated. The distinct influence of CD constants D_J and D_{JK} on the simulated spectrum of a symmetric top has been shown and classified. The theoretical approach for calculation of periods of the RRs of nonrigid molecules [GRM03] was applied in order to evaluate CD induced corrections to the period of J-type transients of benzene. The obtained results are in reasonable agreement with experimental data. It shows that, the present theory could be invoked for the estimation of the CDs from the experimental data without a complete fitted simulation of the RCS spectra. A perturbation in the shape of the rotational transients with increasing laser intensity was examined. The simulation procedure was extended in order to analyze experimental data obtained with high laser intensity. This procedure works well and can be introduced in the analysis of experimental spectra in order to improve the quality of the extracted parameters. For a detailed analysis of the fs DFWM results, the simulated spectra were fitted to the experimental data using a nonlinear least-squares minimizing procedure. The rotational and CD constants of benzene, perdeutero-benzene and cyclohexane in the ground electronic state were obtained with high precision. The molecular parameters obtained for benzene and benzene- d_6 are in a good agreement with the literature values [OMH99, RWB02, JDF91, DJP91, PVC89]. The literature data for cyclohexane have been revised. The observed shift in the rotational constant B_0 of cyclohexane by +0.13% compared to a former rotational Raman investigation [PWW73] is significant and confirms recent microwave spectroscopic results on deuterated isotopomers of cyclohexane and the subsequently derived r_0 geometry of cyclohexane by structural fitting [DBG90, BJK95]. At the complete basis set limit of the *ab initio* calculations, the estimated rotational constants are shifted towards larger values as compared to the experimental results. This is rationalized as the difference between the minimum energy and the vibrationally averaged structure of cyclohexane. These vibrational corrections primarily emerge from the highly anharmonic symmetric breathing modes of cyclohexane.

Chapter 5

5 The Structure of Asymmetric Top Molecules in the Ground and Electronically Excited State

5.1 Introduction

In this chapter the application of pump-probe RCS methods to nonrigid asymmetric top molecules is described. The structure of *para*-difluorobenzene (*p*DFB) in the first electronically excited state S_1 has been obtained by (1+2') pump-probe photoionization (PPI) experiments in a supersonic jet expansion. In addition, the fs DFWM technique is tested for the asymmetric top molecules, pyridine and *p*DFB in the electronic ground state. The experiments were performed in a gas cell at room temperature (298K) and in a collision-free seeded supersonic jet (20–40K). The influence of molecular asymmetry onto the spectra is elucidated by comparison of the experimental results for benzene with pyridine. A complete fit of the spectra, based on a newly developed simulation procedure for nonrigid asymmetric tops, delivers accurate values for the rotational and centrifugal distortion constants, and also information on the anisotropy of the polarizability tensor.

Besides the methodological importance of these investigations, fs DFWM spectroscopy was applied for the first time to asymmetric medium-sized molecules and successfully analyzed. The molecular parameters for near-prolate asymmetric top molecule *p*DFB in the ground electronic state are one of the first experimental rotationally resolved spectroscopic data for this molecule.

5.2 Pyridine

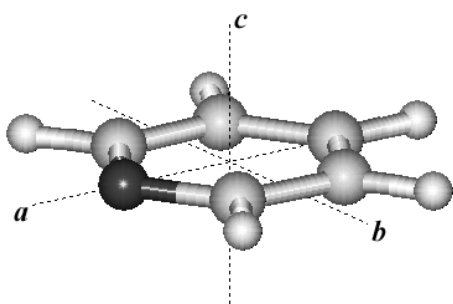


Fig. 5.1 Pyridine (C₅H₅N) structure with principal axes of inertia.

Pyridine (see Fig. 5.1) has been chosen as a molecular benchmark for asymmetric tops in fs DFWM experiments since precise reference values for the rotational and centrifugal distortion (CD) constants are available [Sør67, MQS77, WMD88]. By comparison of the spectra of benzene (see Chapter 4) and pyridine the influence of asymmetry on the fs DFWM spectra under both gas cell and supersonic jet conditions can be

studied. As a result, fitted simulations of the fs DFWM spectra of pyridine rotational and CD constants are presented.

5.2.1 Influence of asymmetry on fs DFWM spectra

In order to evaluate the influence of the molecular asymmetry on fs DFWM spectra, one can compare the spectra of symmetric (benzene) and asymmetric tops (pyridine). The detailed description of the results obtained by the fs DFWM technique for benzene was given in the previous Chapter 4. Fig. 5.2 shows the first 550 ps of the fs DFWM spectra from the vapor of benzene (**a**) and pyridine (**b**) in a gas cell at temperature 298 K and a reduced pressure 10 mbar. Both spectra exhibit strong even and weak odd numbered recurrences. The decay of the rotational recurrences is mainly induced in both cases by collisional dephasing, but even under this condition, the signal from pyridine vapor is a subject of a stronger decay in comparison to the benzene signal. Especially, one can observe a more pronounced dumping of the odd J-type rotational recurrences of pyridine. Both effects could be ascribed to the influence of asymmetry on the rotational coherence signal, and were described in Section 2.2.3.2 and in the literature [FeZ87, BFZ87, FeZ95a].

The fs DFWM spectra obtained under supersonic jet conditions are given in an overview in Fig. 5.3. They exhibit several important features. First, the temperature is significantly reduced to ~30 K, so that the influence of CD is minimized.

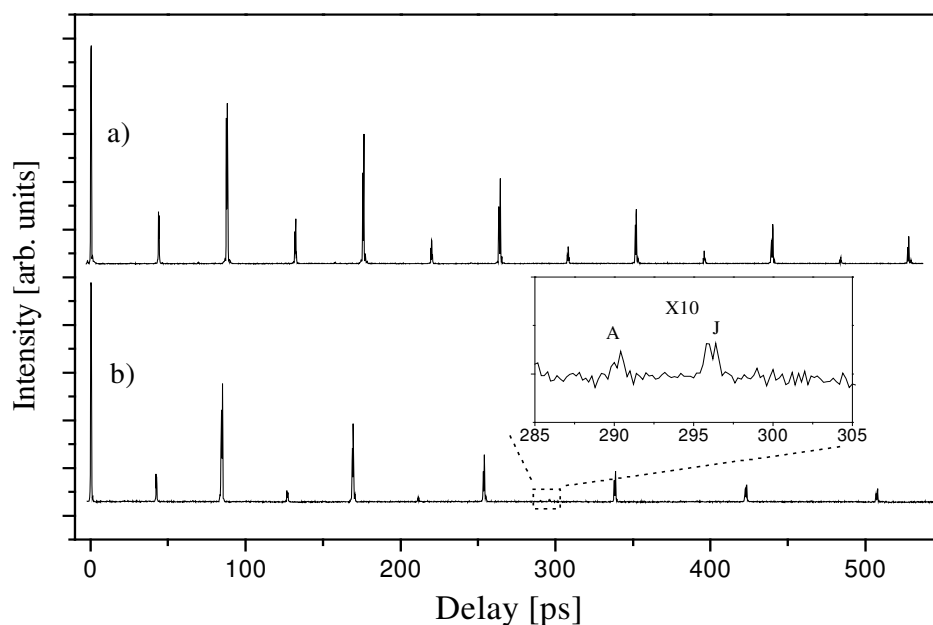


Fig. 5.2 Fs DFWM spectra in a gas cell at 298 K (overview):
a) benzene, **b)** pyridine. Vapor pressure was 10mbar for both measurements.

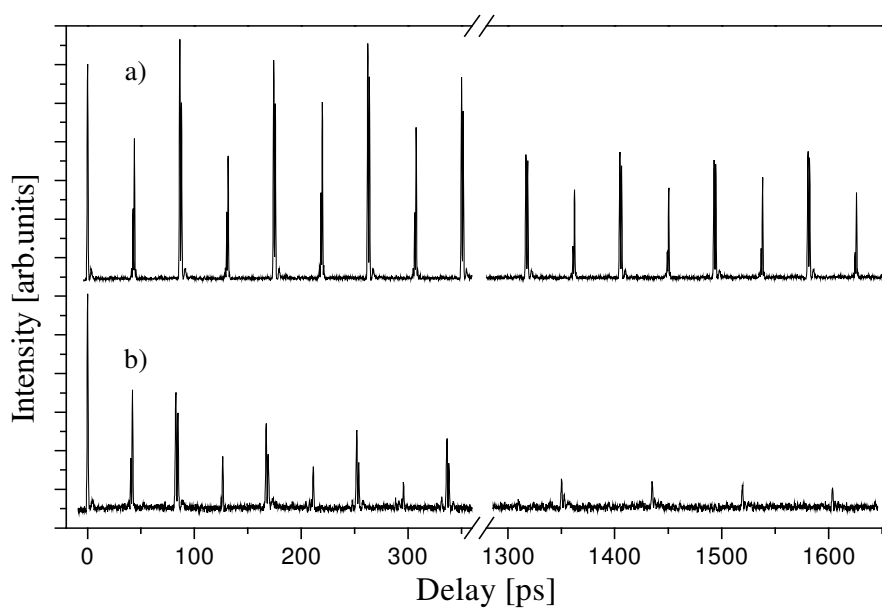


Fig. 5.3 Fs DFWM spectra in a supersonic jet ~ 30 K (overview) :
a) benzene, **b)** pyridine.

Second, in this collision-free environment the collisional dephasing is negligible on the time-scale of observation. However, for pyridine even under supersonic jet conditions a relatively short decay time of the DFWM signal (ca. 1.2 ns) was obtained, pointing towards its asymmetric top character.

Additionally, for pyridine several recurrences of A-type (see inset in Fig. 5.2) have been obtained under gas cell and supersonic jet conditions. The appearance of “*asymmetric*” A-type transients originates in the asymmetry (Ray’s asymmetry parameter $\kappa = 0.8477$) of pyridine with appreciable polarizability parallel to the *c* axis ($\tilde{\beta}_{AA} \approx \tilde{\beta}_{BB} > \tilde{\beta}_{CC}$) [JMR03].

5.2.2 Pyridine by fs DFWM in a gas cell at room temperature and in a seeded supersonic expansion.

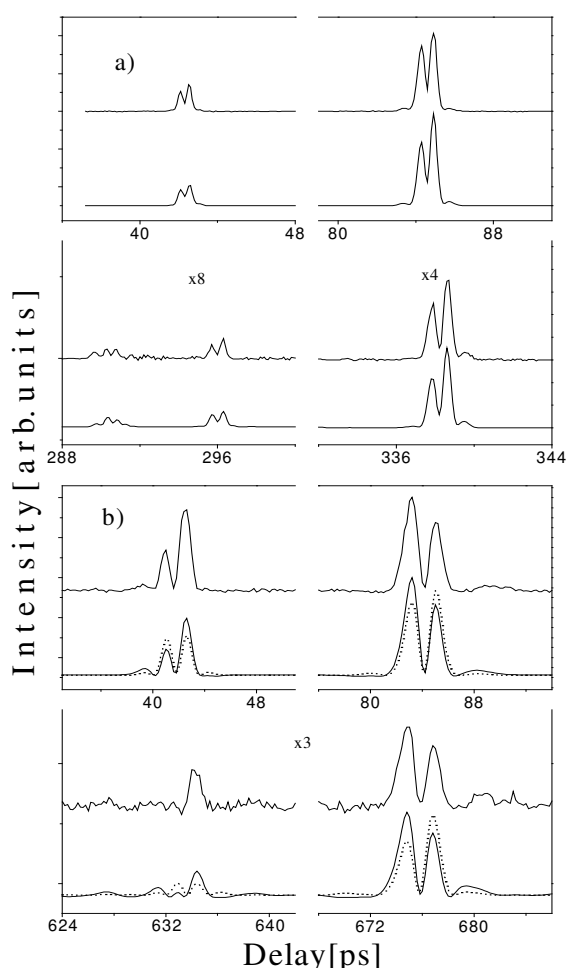


Fig. 5.4 Selected magnified transients (J-type) of pyridine from fs DFWM spectroscopy.

a) Gas cell: experiment (upper trace) at energies $70 \mu\text{J}/\text{pulse}$ for each of the three laser beams and fitted simulation (lower trace).

b) Supersonic jet: experiment (upper trace) at energies $150 \mu\text{J}/\text{pulse}$ for each of the three laser beams and fitted simulation (lower trace; solid line: including parameter k for laser intensity dependence, dotted line: $k=0$).

The experimental conditions were described in previous Chapter 4. Briefly, the overview scans were measured with a step size in time of 0.2 ps. For the detailed analysis, time windows of 10-15 ps were scanned around the transients with a step size of 0.1 ps. The

pressure 10 mbar of pyridine (purity 99.5%, Grüssing GmbH) in a gas cell at room temperature was used.

The fs DFWM spectra of pyridine exhibit an alternation in intensity recurrences with the periodic spacing for J-type transients $42.26 \text{ ps} \geq 1/[2(A+B)]$ (see Figs. 5.2, 5.3, 5.4).

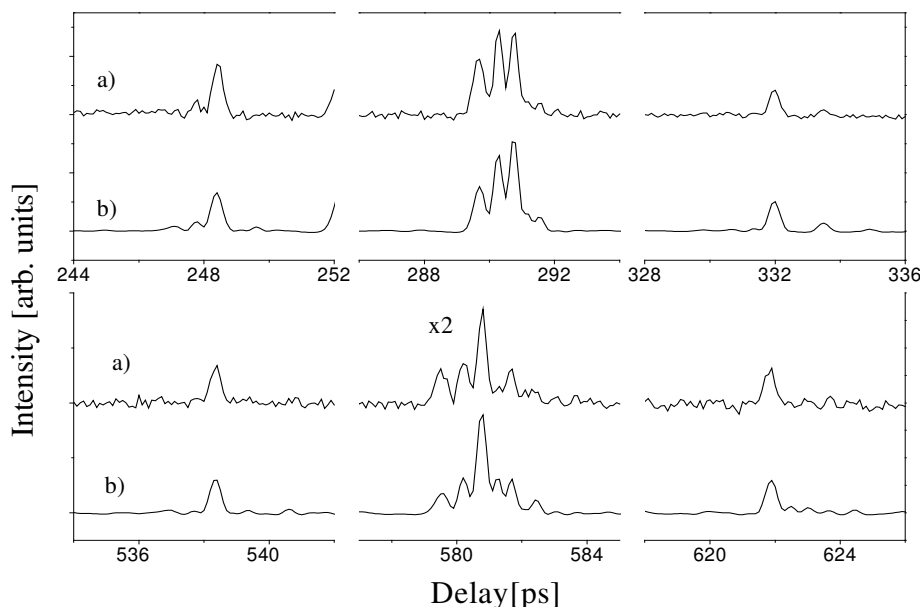


Fig. 5.5 Selected magnified A-type transients of pyridine from fs DFWM spectroscopy in a gas cell:

- a) Experimental spectra. The A-type transients were measured at energies 140 $\mu\text{J}/\text{pulse}$ for each of the three laser beams.
- b) Fitted simulation with additional parameter k .

Additionally, in the gas cell and in the supersonic jet experiment weak A-type recurrences were found (Fig. 5.5) at a spacing of $41.4 \text{ ps} \approx 1/(4A)$. These transients show a modulation in intensity, with a maximum for every 7th transient. It originates from the fact that, normally, an asymmetric top possesses two rotational frequencies, ω_1 and ω_2 [FelZ95, GTB00]. RRs occur when, e.g., $\omega_2 \ll \omega_1$ and ω_1 is proportional to the rotational quantum number, in case of A-type transients $\omega_1^A \sim A * J$. But if $\omega_2^A \sim \sqrt{(A-C)(A-B)}N$ (N is an approximate asymmetric top quantum number) is small but not zero, this small frequency causes the modulation of the RRs intensity, with a period proportional to the ratio of ω_1^A / ω_2^A [GTB00]. Using the values of rotational constants from the Tab. 5.1 one can get $\omega_1^A / \omega_2^A \approx 7.1$ it is exactly what was obtained from the experiment. In order to exemplify the

internal structure of the rotational recurrences and its interesting delay time dependence, several selected transients of pyridine are depicted magnified in Figures 5.4 and 5.5. Each set of data is given in comparison to a simulation, which was calculated from a fit to the experimental spectrum using the procedures described in the section 2.4.3.2 and 2.4.4.

Table 5.1: Results for fs DFWM experiments of pyridine (C_5H_5N) for the ground state: rotational constants and CD constants, fitting parameters, recurrence times and data from the literature.

	Fs-DFWM (this work)			FT Microwave Ref. [WMD88]
	Gas cell		Supersonic jet	
	Non-linear fitting: J- and A- type ^{a)}		Non-linear fitting: With variable k ^{c)} (With $k = 0$) ^{d)}	
A [MHz]	6037.7 ± 0.5	6038.9 ± 0.3	6037.9 ± 1.2 (6038.2 ± 1.3)	6039.24716 ± 0.00090
B [MHz]	5804.0 ± 0.4	5804.8 ± 1.7	5804.8 ± 1.1 (5804.9 ± 1.4)	5804.90738 ± 0.00088
C [MHz]	2960 ± 70	3000 ± 20	3200 ± 340 (3200 ± 450)	2959.21027 ± 0.00086
$C_{\text{calc}}^{\text{e)}$ [MHz]	2959.3 ± 0.2	2959.8 ± 0.5	2959.5 ± 0.7 (2959.6 ± 0.7)	2959.87952 ± 0.00044
Δ_J [kHz]	0.86 ± 0.04	0.86 ± 0.05	$1.34674^{\text{f)}$	1.34674 ± 0.00060
Δ_{JK} [kHz]	-1.7 ± 0.2	-2.0 ± 1.5	$-2.24809^{\text{f)}$	-2.24809 ± 0.00044
Temp. [K]	$298^{\text{f)}$	$298^{\text{f)}$	23 ± 3 (23 ± 3)	

^{a)} Fitting of the complete cell spectra (J- and A-type recurrences) with $k=0$.

^{b)} Fitting of A-type recurrences only, with variable parameter k .

^{c)} Fitting with variable parameter k .

^{d)} Fitting with $k=0$.

^{e)} Calculated from A and B with the assumption of planarity, i.e., $I_C = I_A + I_B$.

^{f)} Fixed.

The following parameters for the fitting procedure were used: the three rotational A , B , C , and two CD constants Δ_J , Δ_{JK} , an external dephasing time τ , a time shift offset for all transients and a scaling factor for the total intensity of the fs DFWM signal. A parametrized polarizability $\varphi = -0.464$ i.e. $\tilde{\beta}_{AA} > \tilde{\beta}_{BB} = \tilde{\beta}_{CC}$ (see Fig 2.12) was assumed. Also, for a detailed analysis the laser intensity dependence of the modulation of the recurrence peaks has to be taken into account. In particular, for the supersonic jet spectra relatively high laser intensity had to be used in order to compensate for the low sample concentration, so that in

these cases the parameter k was used for the fitting. Thus, a better reproduction of the experimental spectra was achieved with χ^2 , the ‘merit function’ by 60% (see Fig. 5.4b). This procedure has nearly no influence on the resulting rotational constants, but allows to improve their precision (see Table 5.1).

The rotational recurrences of the gas cell spectrum of pyridine show a time-dependent structural modulation, which is reproduced well by the fitted simulation for a nonrigid asymmetric top. The position, intensity and structure of the J- and A-type transients (Figs. 5.4 and 5.5) were reproduced in the simulated spectra.

It has to be noted, that the A-type transients are relatively weak (see inset of Fig. 5.2) and were therefore recorded separately with high laser energy. Hence, the simulation and fitting of their structure was only possible by inclusion of the parameter k as discussed above. The resulting parameters are listed in Table 5.1. They agree with the data from microwave spectroscopy [WMD88]. The largest uncertainty was obtained for the rotational constant C , since pyridine can be considered as a near-oblate symmetric rotor, and therefore the fs DFWM spectrum is not sensitive to this rotational constant. However, if one assumes a planar structure for pyridine, C can be calculated from the sum of the moments-of-inertia $I_C = I_A + I_B$ (see Tab. 5.1). The values for C obtained in this way agree well with the literature data [WMD88].

For the spectrum taken in the seeded supersonic jet similar effects as for the nonrigid symmetric rotor molecules are found. Due to the low temperature (≈ 20 K) the structural modulation of the recurrences is strongly reduced. However, there is an intrinsic asymmetry in the intensity pattern of the ‘double peaks’, which is increasing with time delay. Moreover, the decay time of the recurrences is, even under supersonic jet conditions, relatively short with 1.2 ns. The asymmetry in the ‘double peaks’ is mainly caused by the influence of the laser intensity (compare solid and dotted lines in Fig. 5.4b) and could be accounted by the extra parameter k . The decay was attributed to geometrical asymmetry of pyridine and also found from the simulation of the fs DFWM spectrum. The positions and shapes of J- and A-type transients have been reproduced by the fitted simulations. The resulting parameters are summarized in Tab. 5.1. Although the uncertainties of the supersonic jet results are slightly larger than those of the gas cell results the former can be considered as more reliable, since the influence of collisions and CD is minimized. The corresponding ‘final values’ for the rotational constants are emphasized in Table 5.1 [JMR02].

5.3 *para*-Difluorobenzene.

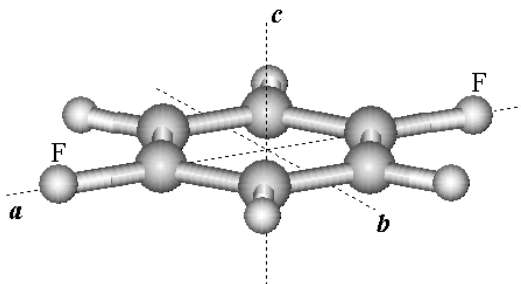


Fig. 5.6 *para*-Difluorobenzene ($C_6H_4F_2$) structure with principal axes of inertia.

RCS has been applied to the investigation of the asymmetric top molecule *para*-Difluorobenzene (*p*DFB) in the ground electronic state S_0 and in the first electronically excited state S_1 . Since this molecule (see Fig. 5.6) has no permanent dipole moment the study of *p*DFB is not possible by microwave spectroscopy. Neusser and coworkers studied *p*DFB and *p*DFB • Ar by

high-resolution resonant two-photon ionization (R2PI) spectroscopy in the UV frequency domain [SNN94a,b]. Parmenter and coworkers studied the vibronic and dispersed emission spectra of *p*DFB and *p*DFB • Ar in order to investigate internal vibrational redistribution (IVR) and cluster predissociation [BCE86, OPS88, SOP91, GPO95]. The high-resolution UV spectroscopy of the *p*DFB monomer was performed by Cvitaš and Hollas applying a rotational contour fit for analysis [CHK70]. A detailed study of the $S_1 \leftarrow S_0$ transition including the assignment of many vibronic bands has been reported by Knight and Kable [KnK88]. However, in the time-resolved investigations of *p*DFB • Ar cluster [WRM02] the rotational constants of the *p*DFB monomer was still a subject of discussion, because no experimental data for the *p*DFB molecule in the ground electronic state S_0 was not available at this time. Only recently, the rotational constants of *p*DFB in the ground electronic state were received using rotationally resolved UV laser induced fluorescence excitation spectroscopy [Sch04]. Thus, the fs DFWM technique was applied in order to obtain experimental ground state data for this molecule.

5.3.1 fs DFWM of *para*-Difluorobenzene, ground electronic state (S_0)

The structure of *p*DFB in the electronic ground state (S_0) was examined by time-resolved fs DFWM both in a gas cell (20mbar) at room temperature and in a supersonic expansion. The experimental conditions used for the measurements were similar as for the pyridine experiments (see section 5.2.2). For the supersonic jet experiments the time delay was

scanned continuously in the region 0–1000ps with step of 0.2ps. Additionally, the two intense spectroscopic features at time delays 1950 and 2930 ps were recorded.

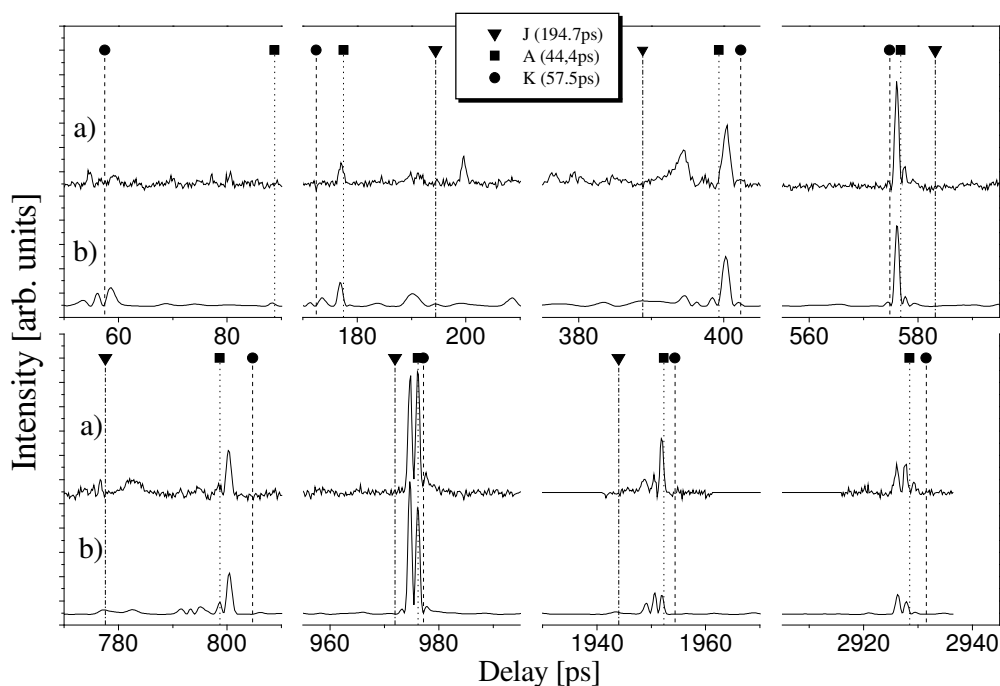


Fig. 5.7 Magnified selected region of the fs DFWM spectrum of *p*DFB in a seeded supersonic jet (33K).

a) Experimental spectrum.

b) Fitted simulation of the spectrum. Extracted constants are given in Table 5.2.

Transient positions are marked by vertical lines: J dash dotted, A dotted, K dashed line.

Fig. 5.7a shows selected regions of the fs DFWM spectrum from *p*DFB in a seeded supersonic jet. Three types of RRs can be assigned in this spectrum. First, A-type transients with a time separation $t_A = 1/4A \approx 44.4$ ps have the strongest intensity. Second, with low intensity and slightly longer period $t_K = [4A - 2(B+C)]^{-1} \approx 57.5$ ps K-type transients, which decay within the first 200ps. In the regions where A- and K- transients are overlapped, the intensity of the peaks (see the regions around 578ps and 977ps) is strongly increased due to the constructive interference between the quantum beats of these transients. Thus the K-type transients can be marginally observed at longer delay times. J-type transients are presented in the spectrum as broad, less intense spectral features at approximate delay times $t_J \approx 194.5$ ps. The assignment was achieved with the help of computer simulation of the spectrum. A fitted simulation obtained by variation of the rotational constants, the parameterized polarizability φ (see section 2.4.4), temperature, and the additional parameter k (section

4.2.4) is plotted in Fig. 5.7b. Results of the fitting procedure are collected in Table 5.2 and compared with the data obtained by electron diffraction [DSH82], an empirical model system constructed by Cvitaš *et al.* [CHK70], high-resolution UV spectroscopy [Sch04] and *ab-initio* calculations. The values from the UV spectroscopy agree with the ones from the model system and show also a good agreement with the results obtained by fs DFWM, whereas the electron diffraction data leads to an A rotational constant which is 1.3 % less than the other values of the A rotational constants. The strong deviation for the A rotational constant might originate from the fact that it is difficult to determine exactly the positions of hydrogen atoms in an electron diffraction experiment, which play a significant role on the rotation motion around a -axis (see Fig. 5.6). The rotation around the b and c axes is influenced by the heavy fluorine atoms, position of which can be determined with high precision in an electron diffraction experiment. Thus, the values of the B and C rotational constants are in good agreement with the values obtained from our measurements.

Fs DFWM experiments on p DFB vapor in the gas cell at room temperature have also been carried out (Fig. 5.8). A preliminary evaluation of peak positions in the spectrum based on rotational constants taken from the fitting results of the p DFB spectrum from a seeded supersonic expansion demonstrates that most of the features can be assigned (see Fig. 5.8). The spectrum exhibits the following peculiarities which originate to the asymmetry of p DFB and the high laser intensity perturbation. First, there is a constant background on top of which the transients are measured. Due to this background also negative features are seen, i. e., some of the transients exhibit a dispersive character. Second, the amplitudes of the transients are not monotonously decaying. Third, some transients are strongly modulated (K-type), others like J(2) extremely broad or single peaks (A-type). Additionally, to the RRs obtained in a supersonic jet expansion (Fig. 5.7), the C-transients with a time separation $t_C = 1/4C \approx 220$ ps can be seen in the room temperature spectrum.

Figure 5.8b shows the simulated spectrum fitted simultaneously to the experimental trace in the region 0 – 500 ps. The extracted constants are given in the Table 5.2, and are in good agreement with the constants extracted from supersonic jet experiments. The CD constants are reported here tentatively and with relatively large error bars. Additionally, the value of the parametrized polarizability tensor (for definition see section 2.4.4) can be inferred from the fitting of experimental data from the gas cell measurements and from measurements in seeded supersonic jet expansion. The values of φ are in reasonable agreements with the

results of *ab-initio* calculations at MP2/aug-cc-PVTZ(5d) level of theory and reported ($\varphi = 0.8$) in Ref. [JÅO02].

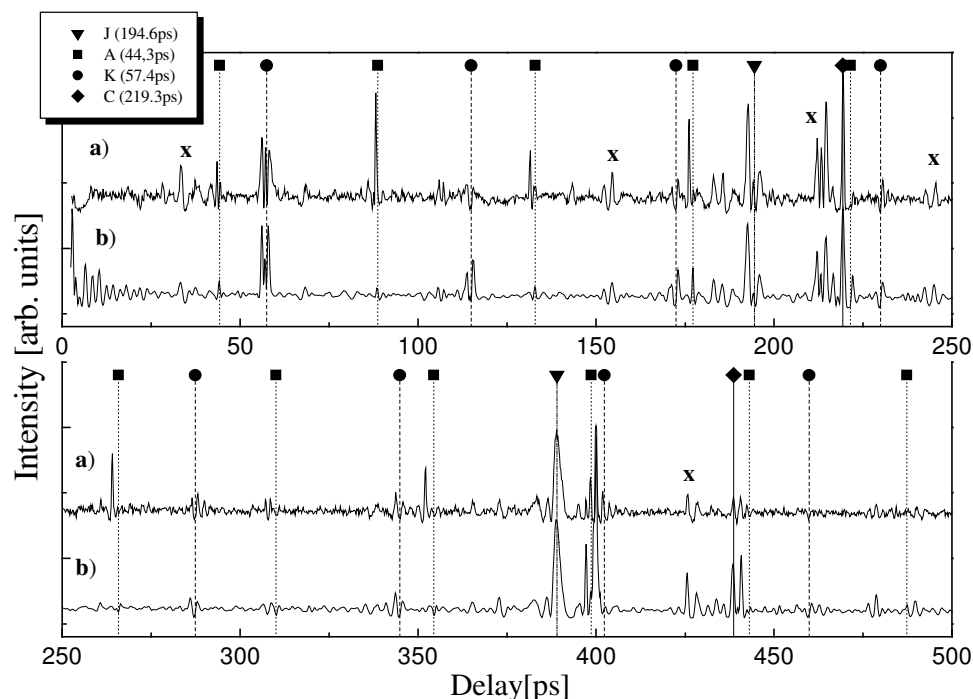


Fig. 5.8 fs DFWM of *p*DFB vapor at 20mbar in a gas cell.

a) Experimental spectrum.

b) Fitted simulation of the spectrum. Extracted constants are given in Table 5.2.

Transient positions are marked by vertical lines: J dash dotted, A dotted, K dashed, C solid line. Signs “x” mark not assigned but reproduced by the simulation spectral features.

The simulation reproduces positions and shapes of most of the transients reasonably well. The simulation failed to reproduce the spectral features, which were preliminary assigned as A-type transients. After careful examination, they were rationalized as J-recurrences of benzene, it was in the experimental system as a contamination. Thus, these features were later excluded from the fitting procedure. Additionally, there are several quite intense features (marked by “x” in Fig.5.8) in the experimental spectrum, which are reproduced by the simulation, but cannot be rationalised as any known type of rotational recurrences. The question of the assignment of these features is still open.

It is useful to analyse the inertial defect ($\Delta = I_C - I_A - I_B$, with I_X being the moment-of-inertia along the axis X) for *p*DFB. It is calculated to $0.05 \pm 0.32 \text{ Amu}\text{\AA}^2$ from the results obtained in the gas cell and 0.35 ± 1.4 from the supersonic jet experiments, respectively (Tab. 5.2). This relatively large inertial defect, in comparison with results of calculations, can be rationalized by the contribution of vibrations [Wol67], which is not included in the calculations.

Table 5.2: Results of the time-resolved fs DFWM and (1+2') PPI experiments on *para*-Difluorobenzene for the ground and the excited states respectively: rotational constants A , B , C in MHz, CD constants D_J , D_{JK} in kHz, recurrence times, temperature $Temp.$, and Ray's asymmetry parameter κ

	Fs DFWM (<i>ground state</i> S_0).		Electron diffraction (S_0) [DSH82]	Model (S_0) [CHK70]	UV spectrosc. (S_0) [Sch04]	<i>ab initio</i> ^{c)} (S_0)	(1+2') PPI (<i>excited state</i> S_1).		UV spectrosc. (S_1) ^{e)} [SNN94a]	RCS (TRFD) (S_1) [Wie00]
	Non-linear fitting:						Lin. Regression	Non-linear fitting		
	Gas cell	Supersonic jet ^{b)}								
A	5638±4	5634.5±0.7	5560.0	5639.1	5637.6(2)	5664.0		5282 ^{a)}	5282(3)	
B	1429.3±0.6	1429±3	1431.8	1428.2	1428.0(1)	1426.6	1449	1435±3	1435.1(6)	1438 ± 29
C	1140.1±0.7	1139±3	1138.6	1139.5	1139.4(1)	1139.6	1126±8	1125±2	1128.6(3)	1131 ± 11
B+C	2569.4	2568	2570.4	2567.7	2567.4	2566.2	2575±7	2560.5	2563.7	2569
Δ_J	0.04±0.4									
Δ_{JK}	0.95±0.33									
Δ_K	-0.7±0.9									
t_j [ps]							194.2±0.5			193.5±2
t_c [ps]							222.0±1.5			221±2
TM or φ ^{d)}	0.56±0.14	0.71±0.12				0.65		(\perp^a), H)		(\perp , \parallel) ^{a)}
Temp. [K]	298 ^{a)}	33±7						18±3		
$\Delta^d)$ [$\text{Amu}\text{\AA}^2$]	0.05±0.32	0.35±1.4	-3×10^{-3}	0.03	-0.006±0.09	-1×10^{-2}			-0.04±0.4	
κ	-0.871	-0.871	-0.867	-0.872	-0.872	-0.873		-0.851	-0.852	

^{a)} Assumed and/or fixed.

^{b)} Fitting of the (1+1') PPI spectra was performed with the assumption that *p*DFB is a rigid asymmetric top (i.e. $D_J = D_{JK} = 0$).

^{c)} *ab-initio* calculations were performed at MP2/aug-cc-PVTZ(5d) level of theory for the ground state (S_0).

^{d)} Alignment of the transition dipole moments (TM) for the (1+1') PPI and parameterised PT φ for the fs DFWM experiments.

^{e)} The rotational constants based on the S_0 values of the model [CHK70]. The uncertainties represent only the difference to the S_0 state.

^{d)} Inertial defect $\Delta = I_C - I_A - I_B$

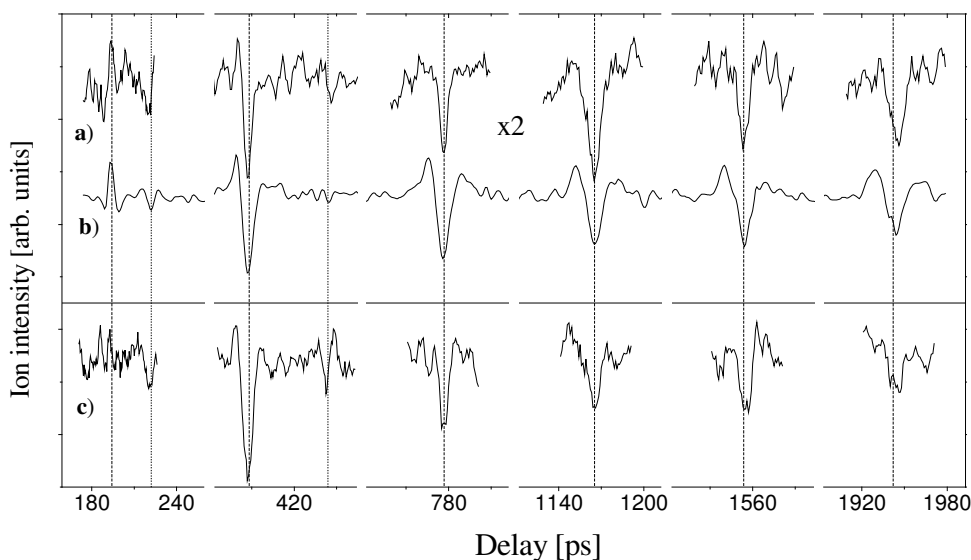
5.3.2 (1+2') pump-probe photoionization of *para*-Difluorobenzene, electronically excited state (S_1)

Fig. 5.9 RCS spectra of *para*-difluorobenzene obtained by pump-probe photoionization.

- a) Experimental spectrum from (1+2') PPI experiment with the pump pulse tuned to the 0_0^0 transition, probe was redshifted by 360 cm^{-1} .
- b) Fitted simulation of the experimental spectrum of pDFB. Parameters are given in Table 5.2.
- c) Experimental spectrum from (1+2') PPI experiment with the pump pulse tuned to the 6_0^1 vibration level of the first excited S_1 state, probe was redshifted by 3350 cm^{-1} .

Note: the transient intensity has been reduced by a factor 2 in order to show the data on one scale.

Transient positions are marked by vertical lines: C dotted, J dashed line.

In order to evaluate precise values for the rotational constants of *p*DFB in the first electronically excited state (S_1), (1+2') pump-probe photoionization (PPI) experiments have been performed. In this experiment the pump laser wavelength was set to the 0_0^0 transition of *p*DFB (36839 cm^{-1}) [CHK70, KnK88], and the energy of the pump pulse was reduced up to few μJ per pulse. The probe laser wavelength (full energy $\sim 30\text{ }\mu\text{J/pulse}$) was redshifted by 360 cm^{-1} in order to avoid direct (1+1') two-photon ionisation. The total energy was below the ionization potential (73871 cm^{-1}) [LeB98]. Since an ion signal could be recorded, it must be due to (1+2') three-photon ionization [GiS74].

In order to prepare a mixture of *p*DFB (Acros, >99% purity) with the carrier gas for the supersonic jet expansion, helium (stagnation pressure 1–2 bar) was bubbled through container with the liquid sample held at room temperature and a continuous supersonic jet was formed after expansion from the nozzle (diameter 80 μ m) to the vacuum chamber. The shot-to-shot polarization switching technique based on an UV Pockels cell was applied in order to improve the signal-to-noise ratio of the measurements [WRB01b]. The ion-current of mass 114 amu was recorded with a boxcar integrator as a function of time delay between pump and probe pulse.

Fig 5.9a shows the measurements of the RCS spectra around of the five even J-type rotational recurrences (marked by a vertical dashed line). Additionally two C-type transients (marked by a dotted line) were obtained with the delay time separation $t_C \approx 1/4C'$. The regions of the spectrum presented on Fig. 5.9a were scanned with a step size of 1 ps. Each scan was repeated five times in alternating directions. Smoothing of the raw data with 5 ps adjacent averaging was employed.

Since correction of the periods of rotational recurrences of asymmetric top molecules is not necessary for A- and C-type transients [FeZ95a], a simple linear regression analysis of the peaks positions vs recurrence number gives a value of the rotational constant C' with quite high precision (Tab. 5.2). The value of the $C' = 1126 \pm 8$ MHz constant is in good agreement with the one reported in the literature [SNN94a]. The precision is reduced since only two C-type transients were obtained. The periodicity of J-type rotational recurrences t_J (see Tab. 5.2) could be evaluated better, since five J transients were measured with higher signal-to-

noise ratio. However, calculated from the equation $B' = \frac{1}{2t_J} - C' = 1449 \text{ MHz}$ the value of

rotational constant B' is 14 MHz larger than the ones obtained by UV spectroscopy [SNN94a]. This effect can be explained by the fact that the simple formula for the RRs periods of J-, K-, H- type of transients for symmetric top species (see Table 2.1 in the Chapter 2) are not correct for asymmetric top molecules (κ (*p*DFB, S_1) = - 0.851 [SNN94a]).

The fitting parameters were: B' , C' rotational constants, the temperature T and scaling parameter for the total intensity. Changes of the A' rotational constant on the order of a few percent do not change the RCS spectrum significantly. Therefore, the value of A' derived by Sussmann et al. [SNN94a] was fixed during fitting procedure. For the simulation a

perpendicular, i.e. b-type, (Fig. 5.6) pump transition dipole moment (TM) has been assumed, while the alignment of the probe TM was fitted. The best reproduction of the experimental spectrum was achieved with the probe TM in the *b,c*- plane, forming an angle $\sim 50^\circ$ with the aromatic ring plane. The fitted simulation of the PPI spectrum of *p*DFB is shown in Fig.5.9b for comparison. It is in very good agreement with the experimental trace. The results of the fitting as well as linear regression analysis are listed in Table 5.2 in comparison with data from rotationally resolved UV spectroscopy [SNN94a], and time-resolved fluorescence depletion [Wie00].

An improvement of the signal-to-noise ratio was achieved by detection of a fragment ion (mass = 63 amu) instead of the monomer ion in the TOF mass spectrometer. The mass spectrum of *p*DFB obtained by electron-impact (70 eV) also exhibits an intense line for the mass 63 amu. [NIST], which is rationalized as a signal from the $C_5H_3^+$ structure. It should be noted that the intensity of the first even J-transients on Fig. 5.9c is about twice larger in comparison to counterpart in trace a. In this experiment the pump laser wavelength was tuned to the 6_0^1 vibrational level of the first electronically excited state of *p*DFB ($0_0^0 + 394\text{ cm}^{-1}$) [CHK70, KnK88]. The probe laser wavelength was redshifted (-3350 cm^{-1}) in order to keep the (1+2') ionisation scheme. The fitted simulation of this spectrum was done with the same input parameters as described before. The evaluated values of the rotational constant B' , and C' are nearly the same as for the vibrationless state, inside of the reported error bars.

5.4 Conclusions.

- (i) fs DFWM spectra have been successfully recorded for asymmetric medium-sized molecules both, under gas cell (298 K) and seeded supersonic jet (20-40 K) conditions.
- (ii) The comparison of an oblate symmetric (C_6H_6) and a slightly asymmetric (C_6H_5N) rotor molecule allows to ascertain the influence of molecular symmetry onto the spectra.
- (iii) Asymmetry A-type transients have been observed for pyridine and very well reproduced using computer simulations.
- (iv) fs DFWM spectra of p DFB obtained both in a supersonic jet expansion and in a gas cell exhibit all to date known types of rotational recurrences. The rich spectrum of p DFB can be rationalized by the combination of the molecular asymmetry (*near-prolate* [$A > B \approx C$] asymmetric top $\kappa = -0.87$) and a *near-oblate* polarizability tensor ($\tilde{\beta}_{AA} = \tilde{\beta}_{BB} > \tilde{\beta}_{CC}$) with components perpendicular to the figure axis (*a-axis*).
- (v) The fs DFWM experimental spectrum of p DFB was successfully simulated. Therefore, the accurate values of the rotational constants, centrifugal distortion constants and the parametrized polarizability for p DFB in the ground electronic state have been obtained.
- (vi) It was shown that fs DFWM measurements could be invoked not only for obtaining high precision structural parameters, but also for achieving information on the diagonal components of the polarizability tensor through the value of the parametrized PT angle φ (see section 2.4.4).
- (vii) Additionally to the fs DFWM measurements the structure of p DFB in the first electronically excited state S_1 was examined by the (1+2') PPI method. The extracted rotational constants are in very good agreement with data from rotationally resolved UV spectroscopy [SNN94a].

Chapter 6

6 Molecular Clusters Studied by fs DFWM: Carboxylic Acid Dimers

6.1 Introduction

In this chapter, the results of time-resolved fs DFWM measurements for the first two members of the homologous group of carboxylic acids in the gas phase will be presented.

The main intention of this investigation was the structural study of dimeric species with hydrogen bonds. The structure of complexes dominated by hydrogen bonding plays a central role in the structural chemistry and biochemistry. Carboxylic acid dimers are often chosen as model systems for studying double hydrogen bonds, which are abundant in nucleic acid base pairs. Both structural and energetical studies of these systems help to provide an accurate quantitative basis for understanding and modeling complex biopolymeric systems. The aggregates of carboxylic acids can be produced in high concentration at room temperature in a gas cell or under supersonic expansion conditions, due to their high binding energy. The formic and acetic acid dimers of the O-H...O/O...H-O type are one of the most stable molecular aggregates with an enthalpy of dimerization of $\approx 62 \text{ kJ mol}^{-1}$ [ChZ78, CHM86]. These dimers were the subject of spectroscopic interest for a long time and were studied in the gas phase experimentally [PaB34, KaB44, ABM69, Der71, Mar87, GHS00, PKB00, MRG03] and theoretically by *ab-initio* calculations [TuD93, BBH95, CVH02, CVH03]. However, due to their symmetry (center of inversion) they do not possess a permanent dipole moment. It is thus not possible to study the dimers by microwave spectroscopy. Only recently, the first completely analyzed high-resolution IR band in the region of the C–O stretch ($1241.7\text{-}1250.7 \text{ cm}^{-1}$) of $(\text{DCOOH})_2$ in the gas phase has been published [MaH02].

Several groups performed IR measurements in the OH stretching region of the carboxylic acid systems (like formic, acetic and benzoic acid dimer) under supersonic jet conditions [ItN02, HSE01, FSZ01]. In all cases, the OH stretching band is strongly broadened, ~ 500 cm^{-1} , and thus, no rotationally resolved and assigned spectrum was obtained in this wavelength region up to now. Different theoretical schemes have been put forward in order to rationalize this broadening in terms of strong anharmonic coupling for formic acid [FZM03] or a monomers-in-dimers model for acetic acid [ESL03]. However these calculations are model studies, which do not allow for an assignment of rovibrational lines. The determination of rotational constants and the structural analysis is thus not possible from these investigations. On the other hand, highly resolved UV spectroscopy, although with overlapping lines, was successfully performed for the benzoic acid dimer and the corresponding rotational constants for the S_0 and S_1 electronic states as well as the tunneling splitting have been determined [RMO00].

The theoretical interest in this type of dimers also stems from the fact that it represents the simplest system for double proton transfer. A summary and discussion of the various theoretical attempts to model this elementary process in terms of barrier height, tunneling splitting and tunneling path is given in Ref. [MaH02]. Another more structural question for formic and acetic acid pertains to their intermolecular potential, which should determine their peculiar crystallization behavior. Contrary to higher homologueous carboxylic acids that form cyclic dimers in the crystalline state, formic and acetic acid form long chains in the crystal with of O-H...O and C-H...O bonds. The question arises whether a theoretical treatment of the dimerization and possible open-chain isomers can be extended towards a description of the structure of the crystalline state and possible cooperative effects [TuD93]. Since there are no rotationally resolved spectra of the hydrogenated formic and acetic acid dimers available, these species have been investigated by fs DFWM in a gas cell (298 K) and in a supersonic jet expansion [MRG03, MGR04].

6.2 Formic acid monomer (HCOOH)

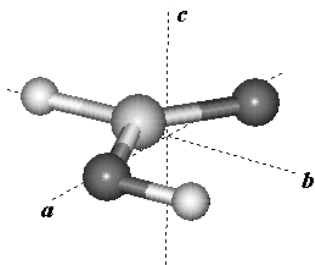


Fig.6.1 *trans* conformer of formic acid (HCOOH) structure with principal axes of inertia.

Figure 6.1 shows a schematic view of the most stable *trans* conformer of formic acid, which is 4.0 kcal/mol more stable than the *cis* conformer [Hoc76]. Since the intensity in DFWM is dependent on the square of the number density, the experimental spectra of formic acid vapor at room temperature exhibits only contribution from the *trans* conformer.

The following parameters for the measurements have been used. Laser intensities were $\approx 3.5 \cdot 10^{12}$ W/cm² for each beam. The intensity of the laser beams had to be limited, otherwise photolysis of the sample takes place, which can be clearly identified by a strong fs DFWM signal of CO₂ as one of the photolysis products. A continuous scan up to 400 ps time delay was measured twice in this way and averaged. For the fitting the first 200 ps of this scan have been used. Formic acid (purity 99%, ACROS Organics) was introduced as vapor into the apparatus at a pressure of 10 mbar and a temperature of 298 K.

Figure 6.2a shows the first 200 ps of the time resolved fs DFWM spectrum of formic acid vapor in the gas cell. Three major sets of rotational recurrences (RRs) are identified in the experimental fs DFWM spectrum. First, one can assign pronounced J-type recurrences with a periodicity of $t_J \approx 22.2$ ps, that persists up to several hundred picoseconds. Second, K-type recurrences with smaller intensity and smaller period $t_K \approx 3.8$ ps are found in the beginning of the spectrum. Also, recurrences of C-type appear, due to the near-prolate top symmetry of the formic acid monomer. The period $t_C \approx 24.1$ ps is slightly longer than that of the J-type recurrences. Since formic acid is a near-prolate top (Ray's asymmetry parameters $\kappa = -0.951$) with non-negligible polarizability perpendicular to the figure axis (*a* axis), A-type recurrences should also be allowed. However, they could neither be observed in the experimental nor the simulated spectrum.

The assignment of the experimental spectrum was achieved with the help of fitted computer simulations. The fitting parameters were the rotational constants *A*, *B*, *C*, three centrifugal distortion (CD) constants $\Delta_J, \Delta_K, \Delta_{JK}$, the parametrized polarizability ϕ , the external

dephasing time τ , the time shift offset for all transients and the scaling factor for the total intensity.

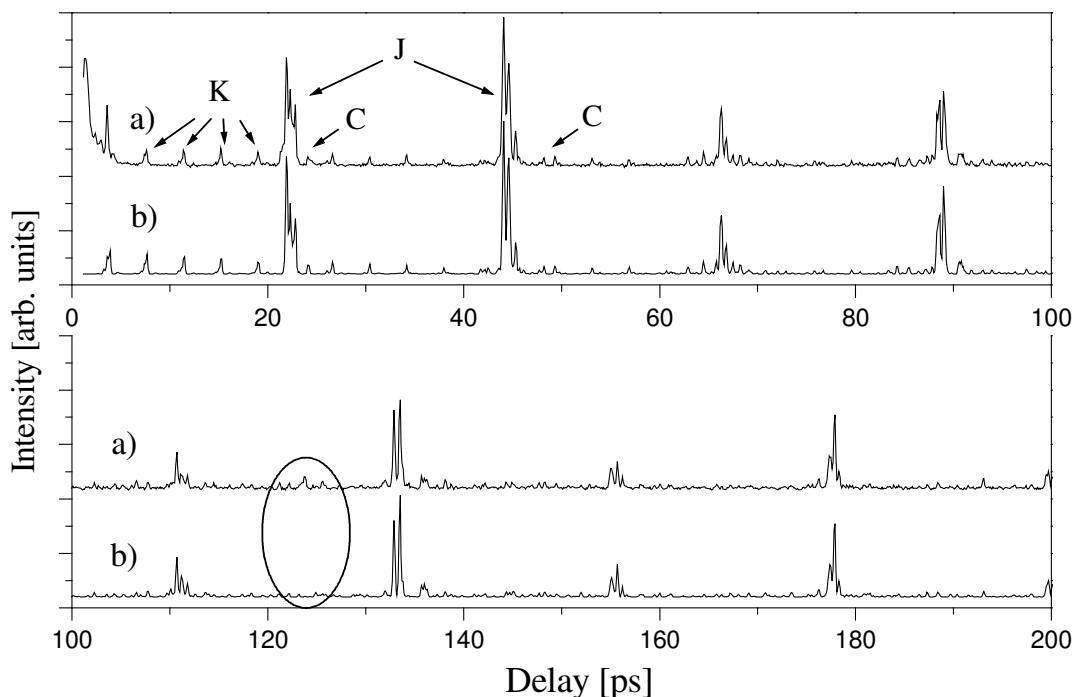


Fig. 6.2 a) Experimental fs DFWM spectrum of formic acid vapor at 10 mbar.

b) Fitted simulation of the spectrum based on a nonrigid asymmetric rotor model.

Extracted constants are given in Table 6.1.

Note, that in the marked region at ≈ 124 ps a J-type recurrence of the formic acid dimer appears in the experimental spectrum.

The simulated spectrum is in excellent agreement with the experimental spectrum (cf. Fig. 6.2b). In only one region around 125 ps time delay (marked in Fig. 6.2) a clear deviation between the experimental and simulated trace is noticeable. The spectral features in this region originate from the formic acid dimer and will be discussed in the following section. For the spectral fitting, the region from 120-130 ps was not considered. The best-fit parameters are listed in Table 6.1 and compared with data from microwave spectroscopy, electron diffraction experiments and DFT calculations. Obtained constants are in good agreement with the reference values from Fourier-Transform microwave experiments [WDB87].

The result for the parametrized polarizability $\varphi = 0.26 \pm 0.06$ can be compared to the results from *ab initio* calculations at (i) the SCF level with an optimized basis set for polarizability

(see details in Ref. [JÅO02]), at (ii) the MP2/cc-pVTZ level [CVH02] and at (iii) the B3LYP/6-311+G(2d,p) level (results of this calculation given in Tab. 6.1 for comparison) giving $\varphi = 0.20$ and $\varphi = 0.35$, and $\varphi = 0.27$, respectively. The φ value obtained by DFT calculation is in the best agreement with the experimental result. Unfortunately, there is no experimental value of PT available from literature. From Fig. 2.12 one can see, that the obtained values for φ correspond to $\tilde{\beta}_{AA} \approx \tilde{\beta}_{BB} > \tilde{\beta}_{CC}$, i. e., an oblate type anisotropy of the polarizability, where the in-plane components are similar. Since there is appreciable polarizability perpendicular to the figure axis (a -axis) of the molecular top, one can expect a similar spectral behaviour as for perpendicular dipole transitions in resonant RCS experiments, which are known to give rise to K-type recurrences in rotational coherence spectroscopy (see Table 2.1 in Section 2.2.3 and Chapter 5).

Table 6.1: Fitting results for fs DFWM experiments of the formic acid monomer (HCOOH) for the ground state: rotational constants, CD constants and parametrized polarizability parameter φ . For comparison, data from microwave spectroscopy, electron diffraction experiments and DFT calculations are listed.

	fs DFWM (this work)	Fourier Transform Microwave [WDB87]	Gas Electron Diffraction [ABM69]	Calculation B3LYP/6- 311+G(2d,p)
A [MHz]	77528 ± 22	77512.213 ± 0.012	73629.8	77870
B [MHz]	12050 ± 5	12055.1045 ± 0.0016	11933.9	12056
C [MHz]	10417 ± 6	10416.145 ± 0.0016	10269.4	10440
Δ_J [kHz]	7.9 ± 1.7	9.989 ± 0.002		
Δ_{JK} [kHz]	-82 ± 22	-86.25 ± 0.04		
Δ_K [kHz]	1703 ± 102	1702.3 ± 0.4		
δ_J [kHz]	fixed: 1.9492	1.9492 ± 0.0004		
δ_K [kHz]	fixed: 42.6	42.60 ± 0.06		
φ / radian	0.26 ± 0.06			0.27
Δ^a [AmuÅ ²]	0.06 ± 0.03	0.076	3×10^{-4}	-1×10^{-3}
κ^b	-0.951	-0.951	-0.947	-0.952

^{a)} Inertial defect $\Delta = I_C - I_A - I_B$

^{b)} Ray's asymmetry parameter is calculated from $\kappa = (2B - A - C)/(A - C)$.

Uncertainties represent 2σ standard deviation (see section 4.2.1).

In order to learn about the influence of molecular asymmetry and CD on the periods of the different types RRs, one can invoke the available theoretical approaches [FeZ95a, GTB00,

GRM03], which are outlined in Sections 2.2.4 and 2.2.5. Formic acid is a prolate, slightly asymmetric top ($\kappa = -0.951$). The difference between the symmetric top value of the period $t_{Sym}^K = 3.77118$ ps (see Table 2.1 Chapter 2) and its counterpart calculated with an inclusion of asymmetric corrections by Eq. 2.21 $t_{As}^K = 3.77132$ ps is as small as 0.14 fs and, of course, can not be detected. It totally justifies the application of the Eq. 2.30 for CD correction on the periods of K-type transients in the RCS spectra.

Performing the linear regression analysis for the first clearly seen fifteen K-type transients in the experimental fs DFWM spectrum (Fig. 6.2), one gets a period $t_{exp}^K = 3.796$ ps, which is ~ 26 fs bigger than t_{Sym}^K obtained from the simple formulas for the prolate symmetric top as outlined in Table 2.1. By taking the best-fit values of the rotational and CD constants from the Table 6.1, and using Eq. 2.30 one gets $t_{Sym,CD}^K = 3.791$ ps. Thus, the calculated values for period of K-type transients are in good agreement with the experimental value of t_{exp}^K . So, one can conclude, that the theoretical approach described in section 2.2.5 works well and the fact that the CD increases the period of the K-type transients is reliably established.

As distinct from the case of K-transients, the asymmetry induced correction (~ 10 fs) for the J-type transients is no longer negligible, and, thus, Eq. 2.28 can not be used in order to calculate CD induced shifts.

6.3 Formic acid dimer (HCOOH)₂

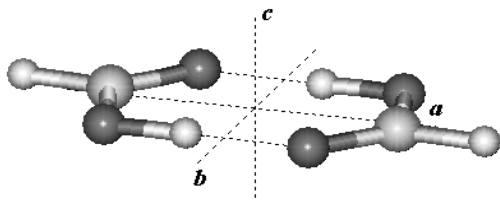


Fig. 6.3 Schematic view of the cyclic formic acid dimer (HCOOH)₂ structure of the O-H...O/O...H-O type with principal axes of inertia.

As was demonstrated in the preceding paragraph the region of the fs DFWM spectral trace for formic acid vapor between 120-130 ps is not reproduced by a spectral simulation employing the monomer parameters. Thus, the signal in this region has been assigned to the formic acid dimer (HCOOH)₂ (see Fig. 6.3). In order to support this assignment, fs DFWM spectra in the region 105-145 ps were measured for different

total pressures of formic acid vapor (Fig. 6.4).

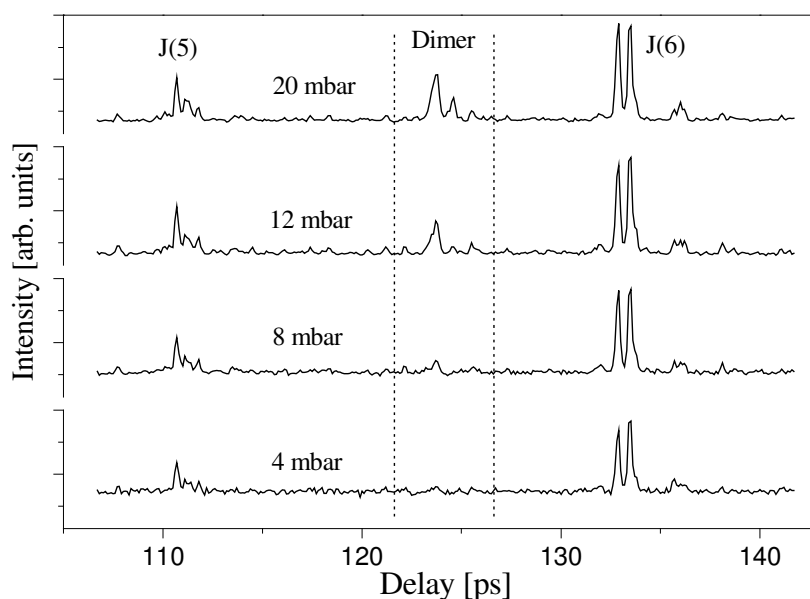


Fig. 6.4 Pressure dependence of the fs DFWM trace of formic acid vapor (298K) in the region of the first J-type recurrence of the formic acid dimer, $t_J \approx 124$ ps. J(5) and J(6) are recurrences of the formic acid monomer.

Note, that the spectra are normalized to the intensities of the formic acid monomer recurrences J(5) and J(6).

In this region between two prominent J-type recurrences of the formic acid monomer, i.e., J(5) and J(6) as marked in Fig. 6.4, are features associated with the dimer. From Fig. 6.4 it is

obvious that, with increasing pressure an additional recurrence is appearing at ≈ 124 ps. The equilibrium of dimerization for formic acid in the gas phase is thermodynamically well-characterized and thus the partial pressures of the monomer and dimer can be calculated from the equilibrium constant:

$$K_p = \exp\left(-\frac{\Delta G_r^0}{RT}\right) \quad (6.1)$$

Here the Gibbs free energy can be expressed through the enthalpy and entropy of the dimer formation.

$$\Delta G_r^0 = \Delta H_r^0 + T\Delta S_r^0 \quad (6.2)$$

The dimerization enthalpy and entropy ($\Delta H_r^0 = -63.8$ kJ/mol $\Delta S_r^0 = -165.1$ J/(K·mol)) from Ref. [ChZ78] were used in order to obtain the free enthalpy and thus the dimer to monomer ratio as a function of the total pressure. As a result, 45% of dimer for an equilibrium mixture with a total pressure of 4 mbar and 69% for 20 mbar were calculated. Given the uncertainty in the pressure measurements (± 1 mbar) and the nonlinear (theoretically: square) dependence of the four-wave mixing signal on the number density, the experimental pressure dependence for the rotational recurrence at 124 ps can be considered as substantial evidence for the proposed assignment. In the following sections supersonic jet experiments and *ab initio* calculations will show that the spectral features can be understood as a J-type recurrence of the formic acid dimer (HCOOH)₂.

6.3.1 Early time response

Before discussing the supersonic jet experiments and the extracted rotational constants, it is instructive to inspect the early time response of the fs DFWM spectra, since it also contains information on both, the structure of the species and the rotational temperature of the sample.

Fig. 6.5 depicts the fs DFWM signal of pure helium (dotted line), formic acid vapor at room temperature and formic acid vapor in a seeded supersonic expansion (dashed and solid line, respectively) near time zero. The signal obtained from pure helium consists of a single peak which can be fitted to a Gaussian function with full-width at half maximum (fwhm) of 230 fs, and a maximum at time zero. The fwhm corresponds to the third-order autocorrelation of

the employed laser pulses. Similar spectra at zero time for argon and xenon have been obtained by Dantus and co-workers [BZD99]. This type of signal appears in the case of temporal overlapping of three pulses in the medium and is often referred to as the coherence coupling artefact or coherence spike (see Refs. in [BZD99]).

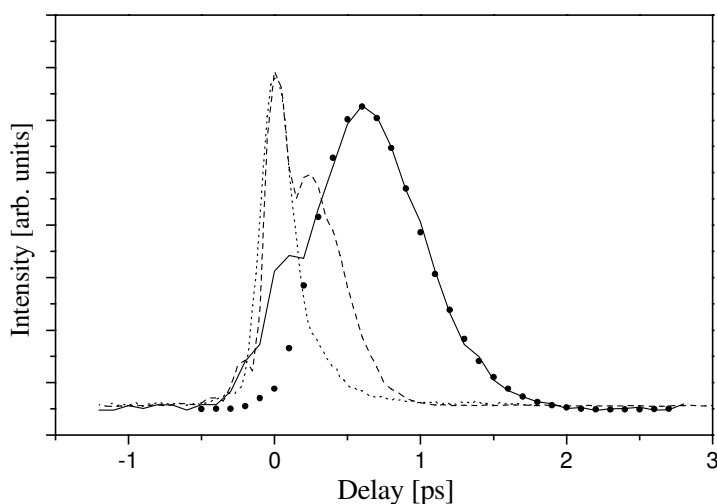


Fig. 6.5 Early time fs DFWM response from atomic helium (dotted line); formic acid vapor at 298K (dashed line); formic acid seeded in a supersonic expansion at ≈ 58 K (solid line); and fitted simulation for the dimer $(\text{HCOOH})_2$ (full circles).

The early time fs DFWM signal from formic acid vapor contains, both in the cell and supersonic jet spectra, the coherence spike followed by a rotational coherence feature. Since the width of a rotational recurrence is proportional to $(I/T)^{1/2}$, where I is the corresponding moment of inertia and T the rotational temperature the fs DFWM spectrum from the jet experiment is broader than that from the experiment at room temperature. This broadening can be attributed to the reduced temperature as well as to the larger moment-of-inertia, due to dimerization. It was possible to fit the early time fs DFWM signal of the supersonic jet experiment by invoking parameters for the formic acid dimer only Table 6.2, (see Fig. 6.5 (full circles)). As fitting parameters, a scaling factor for the total intensity of the fs DFWM signal and the temperature were used. Obtained temperature 58 K is in good agreement with the results from the analysis of the RRs measured under supersonic expansion (Sec. 6.3.2.). It was not possible to fit the fs DFWM early time response from formic acid vapor in the cell by the parameters of the monomer or by those of the dimer or a simple superposition of both spectra. In all cases, it was necessary to invoke a temperature, which is much lower than that used in the experiment in order to account for the width of the transient. This broadening might be attributed to the vibrational modification of the PT correlation function (Eqs. 2.34; 2.35) on the short time scale [MPL95, CDS93].

6.3.2 Supersonic jet experiments

The supersonic jet measurements of formic acid have been performed in a continuous supersonic expansion regime (nozzle diameter: 0.5 mm). The vacuum chamber was evacuated by a 270 m³/h roots pump (Balzers, WKP 250A), which was backed by a second roots pump (Leybold, Ruvac WAU501, 500 m³/h) in combination with a rotary pump (Leybold, Trivac D60A, 60m³/h). The background pressure during the jet experiment was up to $\approx 10^{-1}$ mbar. helium at a stagnation pressure of 0.6 bar was bubbled through the liquid sample (formic acid at room temperature, 298 K) before the nozzle expansion. The laser beams crossed the supersonic expansion ca. 5 mm downstream from the nozzle.

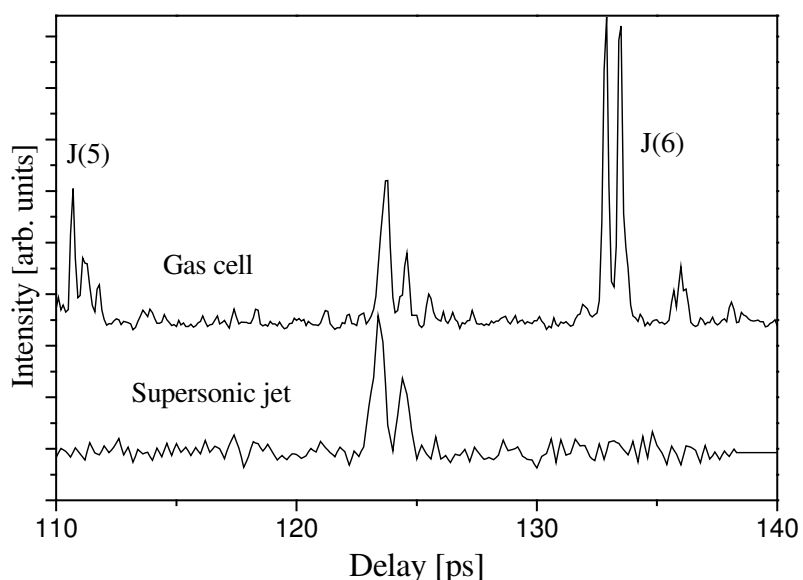


Fig. 6.6 Comparison of the fs-DFWM spectrum of formic acid in a gas cell at 298 K, 20 mbar and in a seeded supersonic jet expansion (≈ 64 K). The recurrences J(5) and J(6) ascribed to the formic acid monomer are missing in the supersonic jet spectrum.

The rotational temperature under this condition, estimated from the fitting of the experimental data, was ≈ 60 K (see Table 6.2). This relatively high temperature is a result of the high concentration of formic acid in the gas mixture used for the supersonic expansion (6-10%).

In order to support the assignment of the rotational recurrence at ≈ 124 ps given in the preceding section the experiment in a seeded supersonic expansion was performed for the time delay region 110-140 ps. The resulting spectrum is plotted in Fig. 6.6 in comparison to

the gas cell spectrum (20 mbar, 298 K). Under supersonic jet conditions the signal from the monomer (J(5) and J(6) in Fig. 6.6) disappeared completely and only the dimer recurrence was observed. This is clear experimental evidence for the proposed assignment.

Table 6.2: Fitting results for fs DFWM experiments of the formic acid dimer (HCOOH)₂ for the ground state: rotational constants (in MHz), CD constants (in kHz), parametrized polarizability parameter ϕ and temperature. Comparison with high-level *ab-initio* calculations and results from electron diffraction experiments. For additional information, the rotational constants of the isomeric dimer structure (C-H...O/O...H-O type) resulting from an *ab initio* calculation are reported.

	Fs DFWM (jet exper.) [This work]	Electron diffraction [Ref. ABM69]	Calculation B3LYP/6- 311+G(2d,p) ^{a)}	Calculation MP2/ cc-pVTZ [Ref. CVH02]	Calculation (Isom. Struct., Fig 6.8) MP2/ cc-pVTZ [Ref. CVH02]
A	6064 ± 1	6010	6056	6034	8172
B	2302 ± 3	2251	2306	2327	1553
C	1665 ± 3	1638	1670	1679	1305
Δ_J	0.1 ± 2				
Δ_{JK}	-6.3 ± 0.6				
Δ_K	6.9 ± 0.8				
ϕ [rad]	0.38 ± 0.05		0.36	0.43	0.28
Δ [AmuÅ ²]	0.65 ± 0.62	-0.069	0.013	0.064	3×10 ⁻⁴
κ	-0.71	-0.72	-0.71	-0.71	-0.93
T [K]	64 ± 5				

^{a)} Calculation performed by D. Kosov (University Frankfurt/M.).

For a fitted rotational temperature of 64 K, the thermodynamic data of the dimerization equilibrium [ChZ78] give nearly 100% concentration of the dimer. It cannot be ruled out that higher aggregates of HCOOH are formed in the supersonic expansion but no other RRs of appreciable intensity that point towards these clusters have been observed.

In order to study the formic acid dimer exclusively, the fs DFWM spectrum under supersonic jet conditions has been measured up to a time delay of 380 ps (Fig. 6.7a). The signal was averaged over 500 laser pulses per delay line setting and a step size 0.2ps was chosen. To improve the quality of the final spectra the scans around the transients were repeated 5 times in alternating directions.

Three consecutive RRs for the dimeric structure were registered and assigned to J-type recurrences with $t_J \approx 1/2(B+C)$. The linear regression analysis of the peak position gave a period of $t_J = 123.8 \pm 0.1$ ps and thus the sum of the rotational constants $(B+C) = 4039 \pm 3$ MHz was obtained. Since the formic acid dimer is an asymmetric rotor with $\kappa = +0.71$

(Ray's asymmetry parameter Eq. 2.3), the above simple symmetric top based formula for t_J is not justified for the extraction of high-precision data.

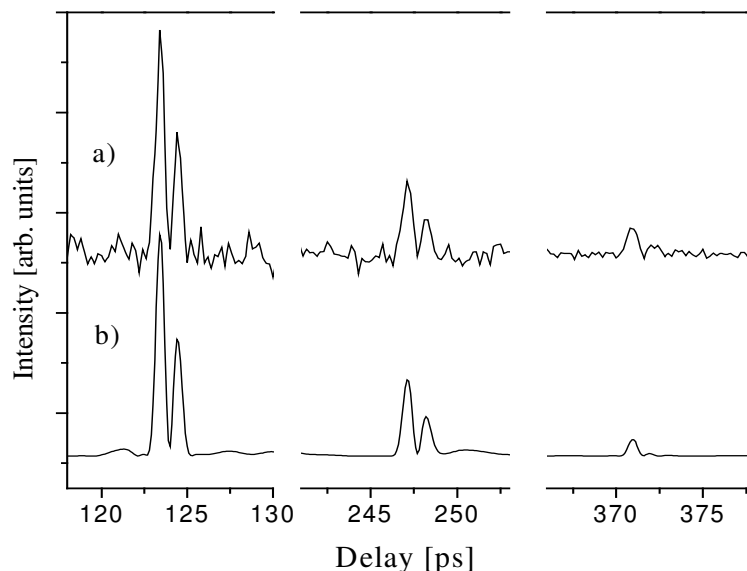


Fig. 6.7 Fs DFWM spectrum of the formic acid dimer (O-H...O/O...H-O type).

Magnified regions around J-type recurrences obtained under supersonic jet conditions ($\approx 64\text{K}$).

- a) Experimental spectrum.
- b) Fitted simulation of the spectrum. Extracted constants are given in Table 6.2.

In order to obtain correct and precise rotational constants, the fitted simulation of the complete fs DFWM spectrum was performed. The simulated spectrum obtained by variation of the rotational and CD constants and the parametrized polarizability φ is plotted in Fig. 6.7b for comparison.

In order to compensate for the low concentration of formic acid in the seeded supersonic expansion it was necessary to use a relatively high laser intensity ($\approx 9 \cdot 10^{12} \text{ W/cm}^2$). In the simulation of the fs DFWM spectra, the laser intensity dependence was accounted for by the time independent weighting parameter κ ($\kappa \approx 0 \dots 1.0$), as described and discussed before (see Section 4.2.4 and Refs [MJR02, JMR03, RMJ03]). In Table 6.2 the fitted parameters for the formic acid dimer structure are listed.

The rotational constants A , B , and C are in reasonable agreement with results from *ab initio* calculations (Table 6.2). The results from the DFT calculation are in slightly better agreement than those obtained at the MP2 level of theory. However, a systematic study of different basis sets and levels of theory have not been performed, so that the chosen

examples are rather selective. For example, the zero-point vibrational averaging with inclusion of anharmonicity is not taken into account like for cyclohexane (see Section 4.3.2.2) and benzene molecules [GaS00]. These corrections (towards smaller rotational constants from the computational point of view) have to be invoked on the highest computational level possible, i. e. CCSD(T) or a comparable level. It cannot be ruled out that good agreement between experiment and theory on a lower level could be found, but this is more likely a result of error compensation.

The sum of the rotational constants $(B+C) = 3967$ MHz from Table 6.2 is noticeably smaller than that estimated from the experimental value of the J-transient period $(B+C) = 4039 \pm 3$ MHz (see above). As mentioned before, this discrepancy stems from the asymmetry of $(\text{HCOOH})_2$.

In Table 6.2 the data from gas electron diffraction [ABM69] are presented for comparison. The rotational constants calculated from the r_a structure from this experiment are systematically smaller by 1-2%, similar to the results for the HCOOH monomer. As a result of the spectral fitting of the fs DFWM data values for the CD constants have also been received. Unfortunately, there is no data available in the literature for comparison*.

The value for the parametrized polarizability φ was received, the meaning of which was in general discussed in the theoretical chapter (Section 2.4.4). Its value is in good agreement with the ones calculated by the *ab initio* methods (see Table 6.2). As can be seen from Fig. 2.12, a value $\varphi = 0.38$ can be related to a near-oblate symmetry of the traceless polarizability tensor (PT) ($\beta_{AA}, \beta_{BB} > 0, \beta_{CC} < 0$) where β_{AA} and β_{BB} are the in-plane components of the PT. There are no experimental values for comparison in the literature. Interestingly, the opposite symmetry for the moments-of-inertia and PT (prolate vs. oblate), which induced the K-type transients in case of the formic acid monomer spectrum (Section 6.2), seems to be not effective for the dimer. This can be rationalized in terms of the larger overall asymmetry of the dimer, which results in a strong damping of K recurrences.

A rotationally resolved IR spectrum in the region of the CO stretch ($1241.7\text{-}1250.7$ cm^{-1}) has been recorded and assigned recently for $(\text{DCOOH})_2$ by F. Madeja et al. [MaH02]. The

* For the interpretation of experimental data on $(\text{DCOOH})_2$, Madeja et al. [MaH02] have employed the so-called S-reduced Watson Hamiltonian, while the A-reduced one was used in this work. Therefore, the rotational constants obtained within the two procedures can be compared, but the centrifugal distortion constants cannot be directly compared.

data was fitted to a rigid rotor Watson S-reduced Hamiltonian. The reported rotational constants are listed in Table 6.3.

Table 6.3: Comparison of the molecular parameters from fs DFWM experiments (present work) with the high resolution IR spectroscopy results for (DCOOH)₂ from Ref. [MaH02] via model structures taken from results of electron diffraction experiments and *ab initio* calculations. Where is $\delta_x = \frac{X_H - X_D}{X_D} * 100\%$, X=A, B, C; X_H, X_D - rotational constants of (HCOOH)₂ and (DCOOH)₂ respectively.

	fs DFWM (This work)	IR spectrosc. [Ref. MaH02]	Electron diffraction [Ref. ABM69]		Calculation MP2/cc-pVTZ [Ref. CVH02]	
	(HCOOH) ₂	(DCOOH) ₂	(HCOOH) ₂	(DCOOH) ₂	(HCOOH) ₂	(DCOOH) ₂
A [MHz]	6064 ± 1	6057.3 ± 0.6	6010	5990	6034	6026
B [MHz]	2302 ± 3	2116.1 ± 0.3	2251	2085	2327	2150
C [MHz]	1665 ± 3	1570.1 ± 0.2	1638	1547	1679	1585
δ _A %		0.11		0.33		0.13
δ _B %		8.79		7.96		8.23
δ _C %		6.04		5.88		5.93

Before comparison of the data to our fs DFWM results, the following remarks should be made. First, the formic acid dimers, both (HCOOH)₂ and (DCOOH)₂, experience a double proton transfer resulting in the tunneling splitting (doubling) of the ro-vibrational states as observed in the frequency domain. The measured fs DFWM signal corresponds, therefore, to a “mixture” of the corresponding two species. From the time domain perspective one can also argue, that, since a time constant for the proton transfer of ≈ 5.8 ns was found [MaH02], the fs DFWM spectra (obtained within the time delay of 380 ps) should reflect the structure of (HCOOH)₂ *before* proton transfer or tunneling. This is equivalent to the coherent excitation and thus linear combination of both tunneling states. However, since the difference in rotational constants for the two (DCOOH)₂ modifications reported in Ref. [MaH02] was as small as 2 MHz, one can take any of both sets of the rotational constants as a reference one. The lowest tunneling state E_l [MaH02] have been used in the following.

Second, to bring into a correspondence the rotational constants of (HCOOH)₂ and (DCOOH)₂ aggregates, the following analysis was employed. Since the molecular structure should not change with exchange of hydrogen (H) by deuterium (D), the rotational constants for (DCOOH)₂ for two model structures were calculated. The first one was taken from the electron diffraction experiment [ABM69], the second one from the *ab initio* calculation at

the MP2 level of theory (the DFT calculation gives similar values, see Table 6.2). The relative changes of the rotational constants δ_X are now calculated for the two hydrogenated/deuterated model pairs and compared to the corresponding changes of the fs DFWM and high-resolution IR results (Table 6.3).

The outcome of this comparison is that the underlying structure reported in Ref. [MaH02] seems to be in agreement with the result of this work, if the MP2 structure is taken as a reference. The relative changes of the rotational constants upon deuteration agree within 0.1-0.6%. Again, the results from the electron diffraction experiment are giving larger deviations. In particular, the strong deviation in δ_A points towards a clear different structural arrangement, since the substituted atoms should be lying on or very close to the *a*-axis (Fig. 6.3). This deviation might originate from the fact that it is difficult to determine exactly the positions of hydrogen atoms in electron diffraction experiments due to the lack of electron density.

6.3.3 Geometry of the formic acid dimer (HCOOH)₂

In the following the brief description of the formic acid dimer molecular structure as a result of the DFT calculation are given, which is consistent with our spectroscopic results. Furthermore, the rotational constants can be used to determine another structural parameter, i. e., the center-of-mass distance *R* of the monomers in the dimer.

The structural results of the DFT calculation (see Table 6.2) can be taken as a good geometric representation for the dimer (HCOOH)₂. The exact bond lengths and angles have to be treated cautiously since no zero-point averaging has been taken into account (see section 4.3.2, and refs. in [RMJ03]). However, a planar structure of the dimer (*C*_{2h} symmetry) was found with two OH...O hydrogen bonds as a minimum energy structure. A sketch of the structure is given in Fig. 6.3 together with the principle axis system. The *a*-axis connects the two centers-of-mass of the monomers and lies in the molecular plane. The inertial defect Δ for the DFT optimized structure is 0.013 amuÅ², whereas from the experiment 0.65±0.62 amuÅ² was obtained (Tab. 6.2). The small positive values are supporting the result of a planar structure [Wol67, GoC84]. The OH...O distance was found from the calculation to 2.665 Å, which underlines the presence of strong hydrogen bonding.

Since, the geometrical parameters for monomeric and dimeric species are available from electron diffraction experiments [ABM69], it is possible to investigate the influence of dimerization onto the monomers structures. The comparison of the structural changes of the geometrical parameters of formic acid upon dimer formation from electron diffraction experiments [ABM69] and DFT calculations is presented in Table 6.4.

Table 6.4: Comparison of monomer/dimer formic acid geometrical changes from electron diffraction [ABM69] and DFT calculations. Bond lengths are in Ångströms, angles are in degrees.

Parameter	Electron diffraction			Calculation B3LYP/6-311+G(2d,p)		
	Monomer	Dimer	Difference	Monomer	Dimer	Difference
C–H	1.106(24)	1.082(21)	-0.024	1.097	1.096	-0.001
C–O	1.361(3)	1.323(3)	-0.038	1.345	1.310	-0.035
C=O	1.217(3)	1.220(3)	+0.003	1.198	1.219	+0.021
O–H	0.984(24)	1.036(17)	+0.052	0.97	1.004	+0.034
∠C–O–H	107.3(44)	108.5(4)	+1.2	107.6	110.7	+3.1
∠O–C=O	123.4(5)	126.2(5)	+2.8	125.1	126.3	+1.2

One can see that changes predicted by DFT calculation are in reasonably good agreement with experimental results, except the lengths changes of C–H and C=O bonds. From the electron diffraction a shortening (-0.024Å) of the C–H bond was obtained due to the formation of the dimer. This is not predicted by the DFT calculations. However, the shortening is within the large experimental error. The computed lengthening of the C=O bond ($+0.021\text{Å}$) is more pronounced than obtained from the experiments ($+0.003\text{Å}$). Similar discrepancies have also been found by Borisenko et al. [BBH95] from comparison of experimental data [ABM69] with *ab-initio* calculations at the MP2/6-31G* level of theory. Following the analysis of Felker and co-workers [COJ92] the distance R between the centers-of-mass of two rigid identical monomers in an aggregate can be expressed as:

$$R^2 = \frac{1}{m} \sum_x (I_x^{(D)} - 2I_x^{(M)}) \quad (6.3)$$

where m is the mass of the monomer, $I_x^{(D)}$ and $I_x^{(M)}$ are the principle moments-of-inertia of the dimer and monomer, respectively.

In order to calculate the intermolecular distance R , the assumption has to be made that the structure of the monomers does not change upon complexation. One can then use the

rotational constants of the monomer and the dimer (see Tables 6.1 and 6.2) in order to calculate the intermolecular (center-of-mass) distance of $R = 2.990 \pm 0.001 \text{ \AA}$.

In fact, from the results of the electron diffraction experiments one can conclude that the structures of the formic acid monomers are changed in the dimer compared to the isolated species. This is corroborated by the results of the *ab initio* calculations (see Tab. 6.4). In order to compensate for this error the following procedure was used. Since from the electron diffraction results [ABM69] the molecular structures are reported for both, the monomeric and dimeric species, one can use this data for calculation of R without ($R^- = 3.024 \text{ \AA}$), and with ($R^+ = 3.018 \text{ \AA}$) the assumption of rigid monomers. From this data a scaling factor $f = R^-/R^+ = 1.001988$ was derived, which compensates for the assumption of rigidity. Although the absolute values of the rotational constants from the electron diffraction experiment deviate considerably from our and the microwave results, it is supposed that the relative changes of the monomeric structure upon dimerization are comparable. Thus, one achieves a scaled value of the intermolecular distance in the formic acid dimer equal to $R = 2.996 \pm 0.001 \text{ \AA}$. This analysis suggests that the distance between the monomeric centers-of-mass calculated from our fs DFWM experiment is 0.028 \AA smaller than from the electron diffraction data reported in Ref. [ABM69]. The center-of-mass distance is the main points of disagreement between the results of the fs DFWM and electron diffraction experiments. This interpretation is also supported by the relative small deviation in the A constant, because the a -axis connects the two centers-of-mass.

6.3.4 Isomeric structure of C-H...O/O...H-O type

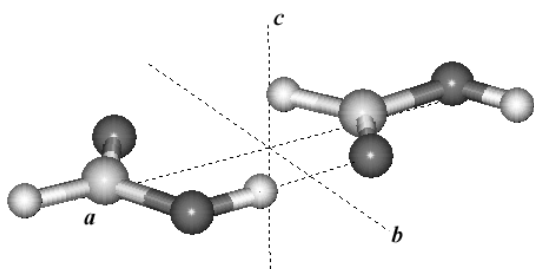


Fig. 6.8 Schematic view of the isomeric structure of the formic acid dimer $(\text{HCOOH})_2$ structure [CVH02] with principal axes of inertia.

The regular structure of the cyclic formic acid dimer is dominated by two strong hydrogen bonds of the O-H...O type (Fig. 6.3). This geometry was obtained as the energy minimum from the *ab initio* calculations discussed in the preceding section and its rotational constants are consistent with experimental data from the fs DFWM measurements.

Another dimeric structure of C-H...O/O...H-O type (see Fig. 6.8) was found for formic acid from the assignment of weak features in the IR spectrum of HCOOH deposited in an argon matrix at low temperature ($< 40\text{K}$). It was stated, that this structure is formed preferentially as the primary product of the formic acid dimerization [GHS00]. Furthermore, from a theoretical population analysis by a molecular dynamics/quenching (MD/Q) technique it was predicted for a microcanonical ensemble that the concentration of the isomeric structure should be even higher than that of the regular structure at room temperature [CVH02].

One advantage of the fs DFWM technique over rotationally-resolved frequency-based methods is that it can be employed under highly congested spectral conditions such as in a gas cell experiment at room temperature. Therefore, the fs DFWM spectra measured at room temperature and high vapor pressure were scrutinized for spectral features that point towards the isomeric formic acid dimer structure.

In order to perform a systematic search, the fs DFWM trace for the isomeric structure was simulated in the rigid rotor approximation (Fig. 6.9b) based on results of *ab initio* calculations (rotational constants and PT, Table 6.2) from Ref. [CVH02]. In the simulated spectrum three types of recurrences are found: J- (≈ 174 ps), K- (≈ 37 ps) and C- (≈ 191 ps) type. Fig. 6.9 shows a comparison of the simulated spectrum for the isomeric structure with the experimental fs DFWM trace in the region of the most intense RRs.

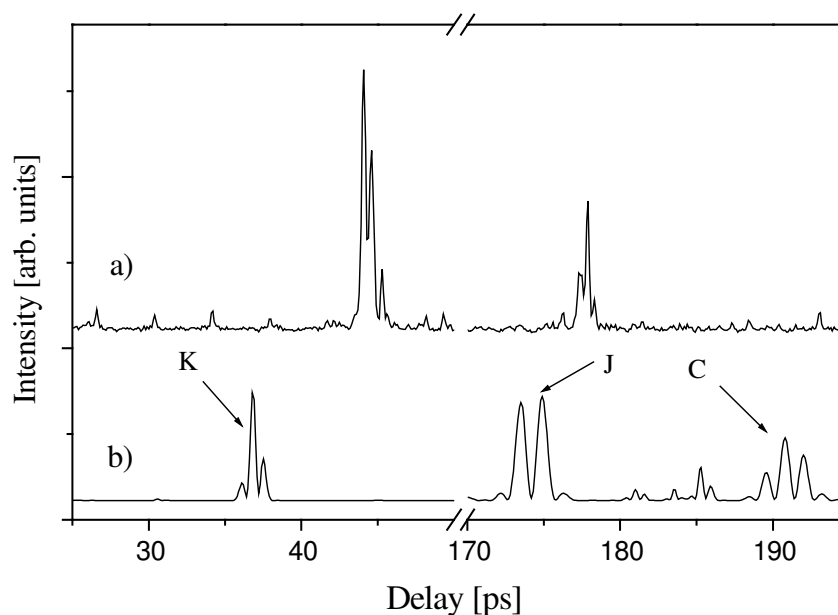


Fig. 6.9 Detailed comparison of the experimental fs DFWM spectrum of formic acid vapor and a simulated spectrum in search of the isomeric dimer structure of C-H...O/O...H-O type.

- a)** Magnified regions of the experimental fs DFWM spectrum of formic acid vapor (298 K, 10 mbar).
- b)** Magnified regions around the main rotational recurrences from a *simulated* fs DFWM trace of the isomeric dimer structure (C-H...O/O...H-O) in the rigid rotor approximation.

Obviously, there is no agreement between the simulated and experimental trace. Even more, all small, undefined structures of the experimental spectrum in these regions were reproduced by a simulation based solely on the monomer data. Additionally, pressure dependent studies have been performed in order to distinguish peaks assigned to the monomer from possible isomeric dimer signals in the region 170-180 ps (region of the first J-recurrence). However, it was not possible to identify any feature as signals originating from the isomeric dimer form. Thus, no experimental support for the existence of the isomeric form at room temperature can be given. A rationalization for this fact could be that this structure might still exist at room temperature, but due to its shallow intermolecular potential, represents a very floppy aggregate so that rotational constants are difficult to derive.

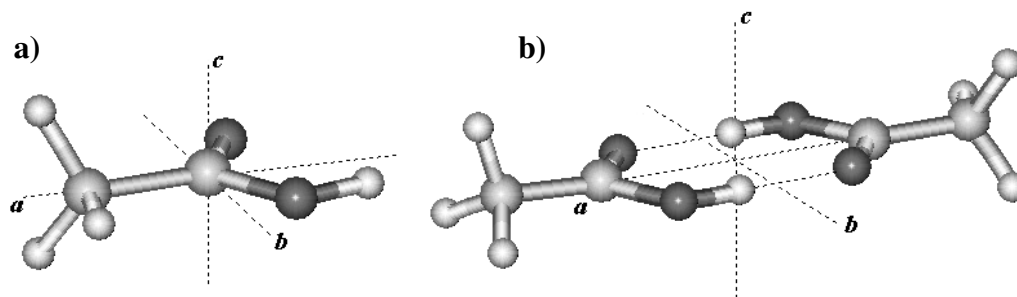
6.4 Acetic acid (CH_3COOH)

Fig. 6.10 **a)** *cis* conformer of acetic acid monomer (CH_3COOH) and **b)** acetic acid dimer (CH_3COOH)₂ structures with principal axes of inertia.

Acetic acid (CH_3COOH) is the second member of the homologous group of carboxylic acids and can exist in either *cis* or *trans* conformation. The *cis* form (Fig. 6.10a) was predicted to be more stable by ~ 6 kcal/mol [TuD93] and this structure was observed in the gas phase in microwave [CSC79, EOS81, EiD83] and electron diffraction [Der71] experiments.

Fs DFWM spectroscopy was applied for the investigation of acetic acid in the gas phase. Figure 6.11a shows the first 200ps of the fs DFWM trace of the acetic acid vapor at room temperature (298K). The signal was very weak due to the strong asymmetry of the monomeric species ($\kappa = 0.386$). Therefore, high laser intensity ($\approx 4.5 \cdot 10^{12}$ W/cm²) for each beam and high pressure of acetic acid vapor (≈ 20 mbar) were used. The parameter k was thus employed for the fitting procedure. The step size of the time delay line was 0.1 ps and 500 laser shots were averaged per delay line setting. The average of three scans in alternating directions was used for the further analysis.

The spectral features in trace 6.11a can be assigned to J and A transients of a near-oblate species. The one with the highest intensity and a period $t_j \approx 24.4$ ps $\geq 1/[2(A+B)]$ was ascribed to J-type recurrences. The sign “ \geq ” is used because the RRs for oblate asymmetric top molecules are slightly shifted to longer time delays [JCO92, GTB00]. The fast decay of the RRs intensity, especially for the odd-numbered recurrences, can be also considered as the indication of the asymmetry of the species under study. Additionally, a weak A(3) rotational recurrence was founded at a time $t_A \approx 66$ ps = $3/(4A)$. From the value of t_A one can

directly estimate the rotational constant A , because the period of A-type recurrences does not depend on molecular asymmetry.

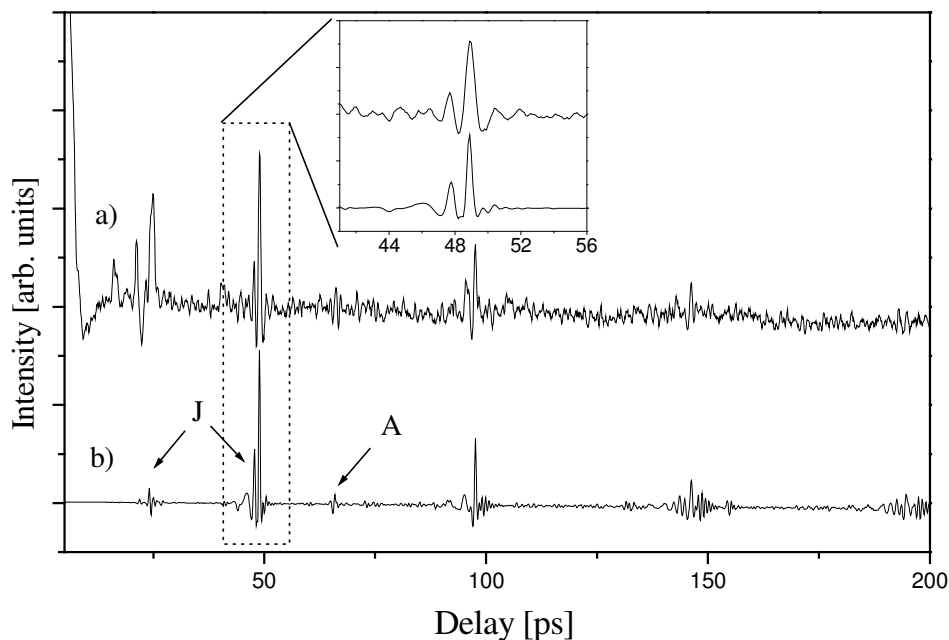


Fig. 6.11 a) Experimental fs DFWM spectrum of acetic acid vapor at 20 mbar.
b) Fitted simulation of the spectrum based on a nonrigid asymmetric rotor model. Molecular constants are taken from Ref. [EiD83].

The assignment was proved by computer simulations of the spectrum. The experimental spectrum was fitted without changing the molecular parameters of the acetic acid monomer taken from Ref. [EiD83]. The parametrized polarizability $\varphi = 0.642$ was taken from an *ab-initio* calculation at the MP2/cc-pVDZ level of theory and kept fixed [Choch]. Thus, the fitting parameters were the dephasing time τ , the scaling factor for the total intensity of the fs DFWM signal and the parameter k ($k \approx 0 \dots 1$). The result of the fitting is plotted in Fig. 6.11b. The simulated spectrum is in good agreement with the experimental one and can be used as a support of the assignment of RRs.

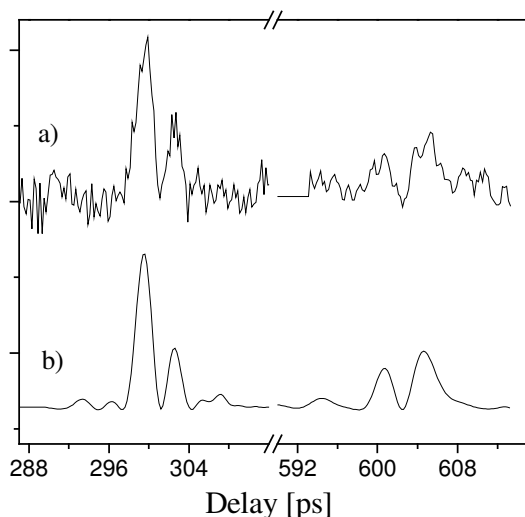
6.4.1 Acetic acid (CH₃COOH)₂ acid dimer in a supersonic jet

Fig. 6.12 Fs DFWM spectrum of the acetic acid dimer (O-H...O/O...H-O type). Magnified regions around J-type recurrences obtained under supersonic jet conditions ($\approx 90\text{K}$).

a) Experimental spectrum.

b) Fitted simulation of the spectrum. Extracted constants are given in Table 6.5a.

Acetic acid forms a cyclic dimeric structure in the gas phase (Fig. 6.10b) with two strong O-H...O hydrogen bonds. The dimerization energy, dimerization entropy, and free energy of dimerization at room temperature (298K) were theoretically and experimentally determined -63 kJ/mol, -153 J/(K·mol), and -18 kJ/mol respectively [ChZ78, FCB80, WiH94, MaS69]. Although, aggregation of acetic acid has been a subject of numerous theoretical [TuD93, CVH03] and experimental studies [Der71, Mar87, PKB00], there is no accurate spectroscopic structural information for the O-H...O/O...H-O dimeric structure of acetic acid available in the literature. Previously, the experimental values were deduced from gas electron diffraction experiments [Der71]. However, the rotational constants calculated from this experiment differ from the experimental values obtained by other high-resolution spectroscopic methods (see also the results for formic acid), due to the number of assumptions concerning the geometry of acetic acid dimer. For example, all C-H bond lengths were assumed equal and all bond angles involving methyl hydrogen atoms to be tetrahedral angles. The O-H bond length in the monomer was assumed to be equal 0.97 Å, in the dimer 1.03Å (as in formic acid [ABM69]), and the \angle H-O-C angles in the monomer and dimer were taken to be 107° (as in the formic acid monomer [ABM69]) and 110° (arbitrarily), respectively. All H-H distances longer than 2Å were omitted in the fitting. Finally, all atoms except the methyl hydrogens were located in one plane [Der71]. It also should be noted here, that all distances given in Ref. [Der71], which were used for

calculating the rotational constants, are distances averaged over thermal vibrations $r_g(1)$ -values [Bar55].

The fs DFWM measurements of acetic acid vapor in a seeded supersonic jet have been performed up to a time delay of 610 ps (Fig. 6.12a). The experimental conditions for these measurements were similar to those for formic acid jet experiments (Sect. 6.3.2). Two J-type transients were obtained with a periodic spacing $t_J \approx 301.4$ ps., and thus the sum of the rotational constants $(B+C) = 1/2t_J = 1659$ MHz can be inferred.

Additionally, the non-linear fitting of the experimental spectrum has been performed. The fitting parameters were the sum of the rotational constants $B+C$, CD constants Δ_J , Δ_{JK} , the temperature T , the scaling parameter for the total intensity, the time shift parameter for the whole spectrum and the decay time τ . The laser intensity dependence was accounted for by the parameter k . The best-fit parameters are compared with available experimental data and selected *ab-initio* calculations in Table 6.5a.

Note, that only the sum of the rotational constants $B+C$ can be fitted because the acetic acid dimer is a nearly symmetric top ($k \approx -0.965$). Thus, it was not possible to determine the rotational constants B and C independently from the fitting of the J-type transients. Due to the same reason, the simulated spectrum is not sensitive to the centrifugal distortion constant Δ_K . The sum of rotational constant $B+C$ is in reasonable agreement with *ab-initio* calculations (Table 6.5a). As for formic acid dimer (see Tab. 6.2), the results of DFT calculations with B3LYP/6-311+G(2d,p) basis set are in slightly better agreement than those obtained at MP2/cc-pVDZ level of theory. The difference between the results of the linear regression and nonlinear fitting can be explained by imprecise determination of the value t_J in the former method of analysis, because only two J rotational recurrences are available from our experiment. Since only J transients are presented in the experimental spectrum and due to the fact that the acetic acid dimer is very symmetric, the rotational constant A cannot be obtained with high precision, and is reported here with a large error ± 300 MHz. The values of two CD constants have also been received. Unfortunately, these values cannot be compared with experimental ones due to the lack of high-resolution data for the acetic acid dimer. The rotational temperature (90 ± 14 K) of the acetic acid dimer was estimated from the spectral fitting analysis. A relatively high rotational temperature has also been obtained for the formic acid dimer (section 6.3.2) in the supersonic expansion. It can be explained by

the high concentration of the substance in the gas mixture and high background pressure $\approx 10^{-1}$ mbar.

Table 6.5a: Fitting results for *fs* DFWM experiments of the acetic acid dimer (CH_3COOH)₂ for the ground state: rotational constants, CD constants (in kHz), parametrized polarizability parameter φ , asymmetry parameter and temperature. Comparison with high-level *ab-initio* calculations and results from electron diffraction experiments.

	fs DFWM experiment (this work)				Electron diffraction [Ref. Der71]	<i>ab initio</i> ^{b)}	<i>ab initio</i> ^{c)}
	Gas cell		Supersonic jet				
	Fitting data	Lin. Regression	Fitting data	Lin. Regression			
A [GHz]	5.6 ± 0.3		5.7 ± 0.3		5578	5651	5557
B [MHz]	871.4				867	883	879
C [MHz]	785.8				758	771	767
(B+C) [MHz]	1657.2 ± 1.3	1655	1657 ± 2	1659	1625	1654	1646
t _j [ps]		302.1		301.4			
Δ _j	-0.09 ± 0.03		-0.09 ± 0.05				
Δ _{JK}	3.0 ± 0.7		3.2 ± 1.2				
κ	-0.965				-0.955	-0.954	-0.953
φ [rad]	-0.276 ^{a)}		-0.276 ^{a)}			-0.023	0.013
T [K]	298 ^{a)}		90 ± 14				

Table 6.5b: Fitting results for *fs* DFWM experiments of the per-deuterated acetic acid dimer (CD_3COOD)₂.

	fs DFWM (this work)		Electron diffraction [Ref. Der71]	<i>ab initio</i> ^{b)}	<i>ab initio</i> ^{c)}
	Gas cell				
	Fitting data	Lin. Regression			
A [GHz]	5.3 ± 0.4		5066	5134	5052
B [MHz]	760.4		749	763	760
C [MHz]	684.8		664	675	671
(B+C) [MHz]	1445.2 ± 1.1	1444	1413	1438	1431
t _j [ps]		346.2			
Δ _j	-0.07 ± 0.04				
Δ _{JK}	2.9 ± 0.6				
κ	-0.967		-0.961	-0.961	-0.959
φ [rad]	-0.276 ^{a)}			-0.023	0.013
T [K]	298 ^{a)}				

^{a)} Fixed.

^{b)} DFT calculations at B3LYP/6-311+G(2d,p) performed by D. Kosov (University Frankfurt/M.).

^{c)} Calculations at MP2/cc-pVDZ performed by J. Chocholoušová (J. Heyrovsky Inst. Prague)

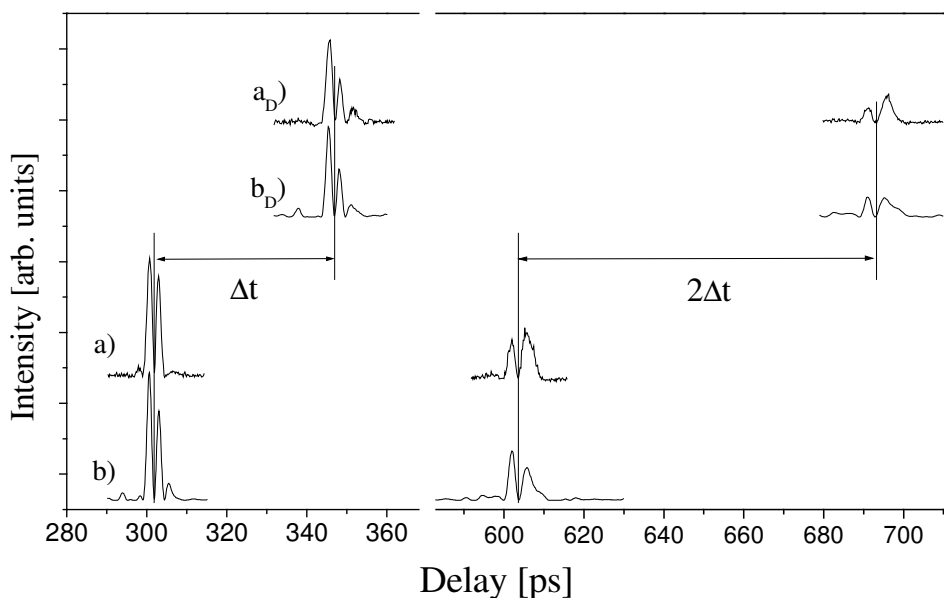
6.4.2 Acetic acid $(\text{CH}_3\text{COOH})_2$ and per-deuterated acetic acid $(\text{CD}_3\text{COOD})_2$ dimer in a gas cell

Fig. 6.13. fs DFWM spectrum of the acetic (**a**, **b**) and per-deuterated acetic (**a_D**, **b_D**) acid dimer. Magnified regions around J-type recurrences obtained at room temperature (300K). **a**) and **a_D**) are the experimental spectra; **b**) and **b_D**) are the fitted simulation of the spectra. Extracted constants are given in Tables 6.5 a,b.

Figures 6.13a and 6.13a_D show the fs DFWM spectra of acetic acid (CH_3COOH) and per-deuterated acetic acid (CD_3COOD) vapor (~ 10 mbar) from a gas cell experiment (298K) in the region of the J-type transients of the dimer structure. The step size for the delay line was 0.1 ps. The obtained signal in these regions was assigned to the acetic acid dimer of the O-H \cdots O/O \cdots H-O type. In contrast to formic acid, acetic acid shows strong J transients from dimeric species in comparison with the fs DFWM signal of the monomer (compare with Fig. 6.11). The intensity of the spectral features presented in Fig. 6.11 is about twenty times smaller than those for the acetic acid dimer (Fig. 6.13). This effect can be explained by the difference in the molecular symmetry of the monomeric ($k = 0.386$) and dimeric ($k = -0.955$) species. It is well known [FeZ95a, JCO92] that the intensity of the rotational coherence signal is higher for symmetric top molecules than from asymmetric ones. However, careful analysis of the time-resolved fs DFWM trace up to 910 ps shows that

there is no other spectral features, except J rotational recurrences (Fig. 6.13), which can be attributed to the cyclic acetic acid dimer. This fact plays a significant role in the estimation of molecular parameters obtained from the non-linear fitting of the experimental trace.

Three J-type transients of the acetic acid dimer $(\text{CH}_3\text{COOH})_2$ (the third J transients is not shown in Fig. 6.13a) and two of the per-deuterated acetic acid dimer $(\text{CD}_3\text{COOD})_2$ have been measured. The transients occur at a time period of ~ 302.1 ps for the $(\text{CH}_3\text{COOH})_2$ and ~ 346.2 ps for the $(\text{CD}_3\text{COOD})_2$ species. The difference of ~ 44 ps (see Fig. 6.13) between the position in time of the recurrences is determined by the smaller rotational constants B and C of the latter one. From the linear regression analysis the rotational constants $B+C=1655$ MHz of the acetic acid dimer $(\text{CH}_3\text{COOH})_2$ and $B+C=1444$ MHz of the per-deuterated acetic acid dimer $(\text{CD}_3\text{COOD})_2$ were extracted. The fitted simulation (Figs. 6.13b, 6.13b_D) gives the sum of the rotational constants $B+C=1657.2\pm 1.3$ MHz and $B+C=1445.2\pm 1.1$ MHz for acetic acid and per-deuterated acetic acid dimer respectively (see Tables 6.5 a,b). In order to account for all thermally populated rotational levels of these dimeric structures, transition frequencies of 200 J rotational levels were calculated. The shift of the sum of the rotational constants obtained from the linear regression analysis towards smaller values can be rationalized by the influence of the centrifugal distortion on RR periods (see section 2.2.5 and ref. [GRM03]) as well as by the asymmetry of the species under study (see section 2.2.4 and refs. [BaZ89, GTB00]). As in case of supersonic jet, the experiment in the gas cell is not very sensitive to the rotational constant A . Nevertheless, the molecular parameters obtained from the fitting of the time-resolved fs DFWM spectrum of the dimeric species $(\text{CH}_3\text{COOH})_2$ are in good agreement with data obtained from the supersonic jet experiments and *ab-initio* calculations. The electron diffraction experiment [Der71] gives rotational constants, which are smaller by 1% - 2%, similar to the results for the formic acid monomeric and dimeric species (Tabs. 6.1, 6.2, 6.5a).

The structural results of the DFT calculation (see Table 6.5a) can be taken as a good geometric representation for the dimer $(\text{CH}_3\text{COOH})_2$. As was mentioned in Section 6.3.3, the exact bond length and angles from *ab-initio* calculations have to be considered carefully, since zero-point averaging must taken into account. However, the difference in hydrogen bond length O-H...O 2.680 (0.010) Å obtained from experiment [Der71] and 2.658 Å from DFT calculations is notable and can be considered as the main point of disagreement between the results of time-resolved fs DFWM and electron diffraction [Der71]

experiments. The changes of the acetic acid geometrical parameters upon dimer formation (Tab. 6.6) were also analyzed like in Section 6.3.3 for formic acid.

Table 6.6: Comparison of monomer/dimer formic acid geometrical changes from electron diffraction [Der71] and DFT calculations. Bond lengths are in Ångströms, angles are in degrees.

Parameter	Electron diffraction			Calculation B3LYP/6-311+G(2d,p)		
	Monomer	Dimer	Difference	Monomer	Dimer	Difference
C–C	1.520(5)	1.506(5)	-0.014	1.503	1.501	-0.002
C–O	1.364(3)	1.334(4)	-0.030	1.358	1.320	-0.038
C=O	1.214(3)	1.231(3)	+0.017	1.204	1.225	+0.021
O–H	0.97 ^{a)}	1.03 ^{a)}	+0.06	0.97	1.003	+0.033
∠C–O–H	107.0 ^{a)}	110.0 ^{a)}	+3.0	106.8	110.7	+3.1
∠O–C=O	122.8(6)	123.4(8)	+0.6	122.3	126.3	+1.2

^{a)} Assumed in the electron diffraction experimental data analysis [Der71].

The *ab-initio* calculations fail to predict the C–C bond shortening upon dimer formation, similar to the situation for the C–H bond of formic acid. But in general, the results of DFT calculations for acetic acid are in good agreement with experiment [Der71] and give even slightly better predictions in comparison with those for formic acid.

In order to analyze the experimental data obtained for the per-deuterated acetic acid dimer it was assumed that the molecular structure is not changed upon exchange of hydrogen (H) by deuterium (D). Hence, rotational constants for the structures reported in the electron diffraction study [Der71] and from the *ab-initio* calculations at the MP2 and DFT level of theory were calculated. The parametrized PT value φ have been also kept fixed. The fitting results for the O–D...O/O...D–O type of per-deuterated acetic acid dimer are collected and compared with other available data in Table 6.5b.

There is a difference between the experimentally obtained value of parametrized polarizability φ and those calculated by the *ab-initio* methods (see Tabs. 6.5a,b). Although, the positions and shapes of J- recurrences of near-symmetric tops do not depend on φ , one nonetheless can estimate this parameter. Indeed, any deviation of the traceless PT from a near-prolate symmetry ($\beta_{AA} > \beta_{BB} \approx \beta_{CC}$) will cause the appearance of K-type transients at $t_K^{(H)} \cong (4A-2(B+C))^{-1} = 52.4$ ps for the $(\text{CH}_3\text{COOH})_2$ and at $t_K^{(D)} \cong 54.6$ ps for the $(\text{CD}_3\text{COOD})_2$. However, no spectral features at these times were observed and all the structures of the experimental spectrum in this region were reproduced by a simulation based solely on the monomer data (see, e.g., Fig. 6.11). Therefore, the value $\varphi = -0.276$ was fixed in the fitting procedure, which corresponds to the near-prolate PT (see Fig. 2.12), as

distinct from the predictions of *ab-initio* calculations. This disagreement is most likely related to the fact that the PT is actually frequency-dependent and should be taken at the frequency ω of the degenerate laser pulses. This frequency dependence was ignored in the calculations. Thus, it is desirable to perform more accurate calculations of the PT.

The RCS spectrum of a prolatelike symmetric top ($-1 < \kappa < 0$) can exhibit C-type recurrences, the intensity of which increases with molecular asymmetry. That is exactly what was obtained from simulations for the acetic acid dimer. Using the symmetry predicted by *ab-initio* calculation, the simulated spectrum always shows pronounced C transients with a time separation $t_C = 1/4C = 324.7$ ps. Therefore, it was necessary to change the symmetry of the molecule keeping $B+C$ fixed. As a result, rotational constants B and C have been obtained and the asymmetry parameter κ was calculated (see Tabs. 6.5a,b). The obtained values of κ are systematically shifted towards more symmetrical structures, both for $(\text{CH}_3\text{COOH})_2$ and $(\text{CD}_3\text{COOD})_2$. Tentatively this can be attributed to the dependence of the fs DFWM signal from internal rotations of the methyl groups, which are not included in our simulations. A similar effect was observed for *para*-Xylene (C_8H_{10}) - an aromatic ring with two methyl substitutions in *para* position. The simulated fs DFWM spectrum for this molecule also exhibits strong C-type RRs with intensity comparable to the J-type transients, while in the experimental spectrum they are nearly not observed. In addition, the dependence of the collision energy transfer on the J quantum number must, in principle, also be considered in the simulation. Currently the collisions are taken into account only phenomenologically by an exponential decay fitted to the experimental spectrum. But even without these details, the obtained molecular constants for the cyclic dimeric structure of the acetic and per-deuterated acetic acid can be considered as the first accurate rotational data obtained by a spectroscopic technique.

6.5 Conclusions

Fs DFWM spectroscopy has been applied to the structural investigation of the first two members of the homologous group of carboxylic acid with rotational resolution. The spectrum of formic acid in the gas cell exhibits RRs of both monomeric and dimeric species. In contrast to formic acid, acetic acid shows strong recurrences from dimeric species even in the fs DFWM spectra at room temperature. This can be explained in terms of different symmetry of the moments-of-inertia tensor, which modulates the intensity of the RRs (the fs DFWM signal is stronger for symmetric species). On other hand, fs DFWM spectra obtained under supersonic jet conditions exhibit RRs only from dimeric structures for both formic and acetic acids.

A complete fitting of the spectrum of formic acid vapor in the gas cell provided information about rotational and CD constants and PT of formic acid monomer with high precision. A theoretical approach, developed in our group, for the calculation of CD induced shifts of RRs periods for symmetric top species (see section 2.2.5 and [GRM03]) has been tested for fs DFWM spectrum of the formic acid monomer. It has been shown that the formulas (2.28-2.30) derived for symmetric tops can be applied for the prolate slightly asymmetric species ($\kappa = -0.951$) in case when the pertinent asymmetric correction (for K-type transients ≈ 0.14 fs) is small enough.

For the first time, the rotational constants of the regular O-H...O/O...H-O isomer of (HCOOH)₂ and (CH₃COOH)₂ (Figs. 6.3, 6.10b) have been obtained by a spectroscopic technique. Values for the rotational constants and PT are in good agreement with the results of *ab initio* calculations. The experimental transients for the formic and acetic acid dimeric species have been reproduced slightly better by the DFT calculation with B3LYP/6-311+G(2d,p) basis set than by those obtained at the MP2/cc-pVDZ level of theory. Therefore, the DFT structural optimization was used in order to describe the molecular structure of the formic and acetic dimer and for comparison with the data from the electron diffraction experiments [ABM69, Der71]. The rotational constants estimated from the results of gas phase electron diffraction experiments are in general smaller than those from rotationally-resolved high-resolution spectroscopy (see Tabs 6.1, 6.2, 6.5a,b). The overestimated length of the O-H...O hydrogen bond was rationalized as the source of the

difference between the rotational constants of the dimeric species reported in Refs. [ABM69, Der71] and those obtained by fs DFWM experiments.

The structural changes of formic and acetic acids upon dimerization were exemplified from the results of DFT calculations. The obtained results are in good agreement with those reported in the literature [BBH95].

In summary, it have been shown that fs DFWM technique, as an experimental implementation of the rotational coherence spectroscopy, can be used for the high resolution structural study of molecular clusters without dipole moment and chromophore. For the first time, the fs DFWM technique has been successfully applied for the investigation of clusters.

Chapter 7

7 Two-Ring Molecules in RCS

7.1 Introduction

In this chapter the results obtained by fs DFWM and (1 + 1') pump-probe photoionization (PPI) on the rotationally-resolved spectroscopy of large two-ring (aryl-cycloalkyl) molecules in the gas phase will be presented. In particular cyclohexylbenzene (CHB), *para*-cyclohexylaniline (*p*CHA) and nicotine (3-(N-methyl-2-pyrrolidinyl)pyridine) were studied at elevated temperatures in a heat pipe oven by fs DFWM spectroscopy. In order to extract the structural changes upon electronic excitation, the (1 + 1') PPI spectrum of CHB under a supersonic jet expansion was obtained and analyzed.

These systems were chosen since they pose several interesting spectroscopic problems, like the question of the conformation of the cycloalkyl ring or the torsion between both rings. Moreover, two of the molecules (*p*CHA, nicotine) show a biological activity and thus, their accurate molecular structure is of importance.

All compounds of this study have a low vapor pressure at room temperature (<0.1 mbar) and therefore have to be heated in a gas cell for laser spectroscopic studies. Thus, the investigations in a heat pipe oven have been performed. This experimental technique allows for investigations of gaseous samples over a longer time without the problem of window contamination. The intention of the work presented in this chapter is to demonstrate that it is possible in this way to obtain rotationally resolved spectra for large two-ring molecules at elevated temperatures. From the analysis of the fs DFWM spectra the rotational and centrifugal distortion constants were obtained and by comparison with DFT calculations the inter-ring conformations have been proposed. From comparison of the CHB geometries in the ground and electronically excited state the structural changes upon excitation can be extracted.

7.2 Cyclohexylbenzene.

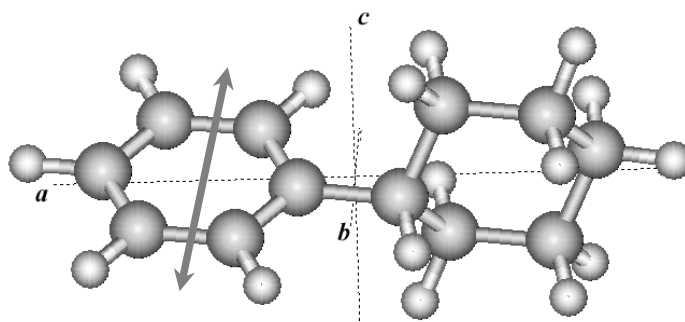


Fig.7.1 Cyclohexylbenzene (C₁₂H₁₆) structure with principal axes of inertia. Transition dipole moment (indicated by arrow) is aligned nearly perpendicular to the *a*-axis.

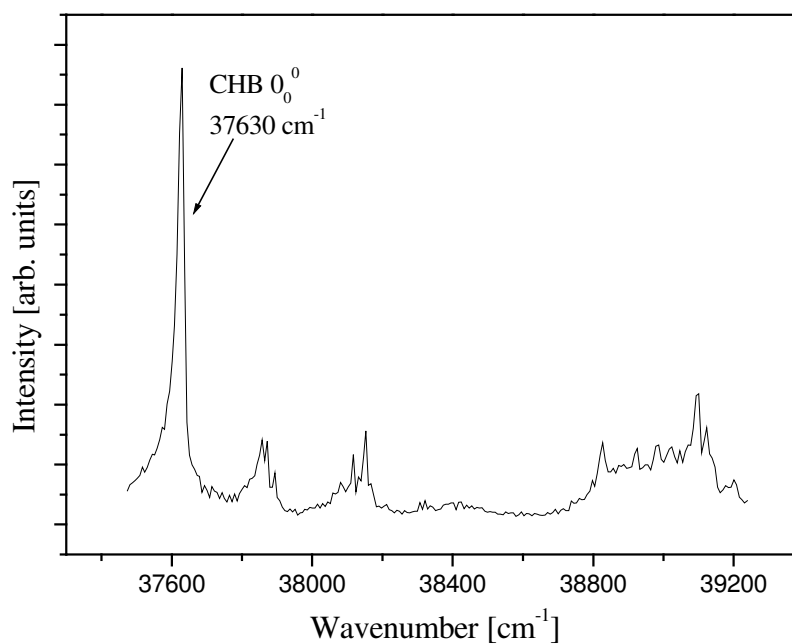


Fig. 7.2 Resonant two photon ionisation (R2PI) spectrum of a supersonic expansion of cyclohexylbenzene obtained with picosecond laser system (FWHM~10cm⁻¹). The 0₀⁰ transition is at 37630 cm⁻¹.

Since for cyclohexylbenzene no data about UV transitions is available in the literature, the UV spectrum of CHB in a seeded supersonic expansion was measured in our laboratory by resonant two-photon ionisation (R2PI) with a picosecond laser system. CHB exhibits a strong 0₀⁰ transition at 37630 cm⁻¹ (Fig. 7.2).

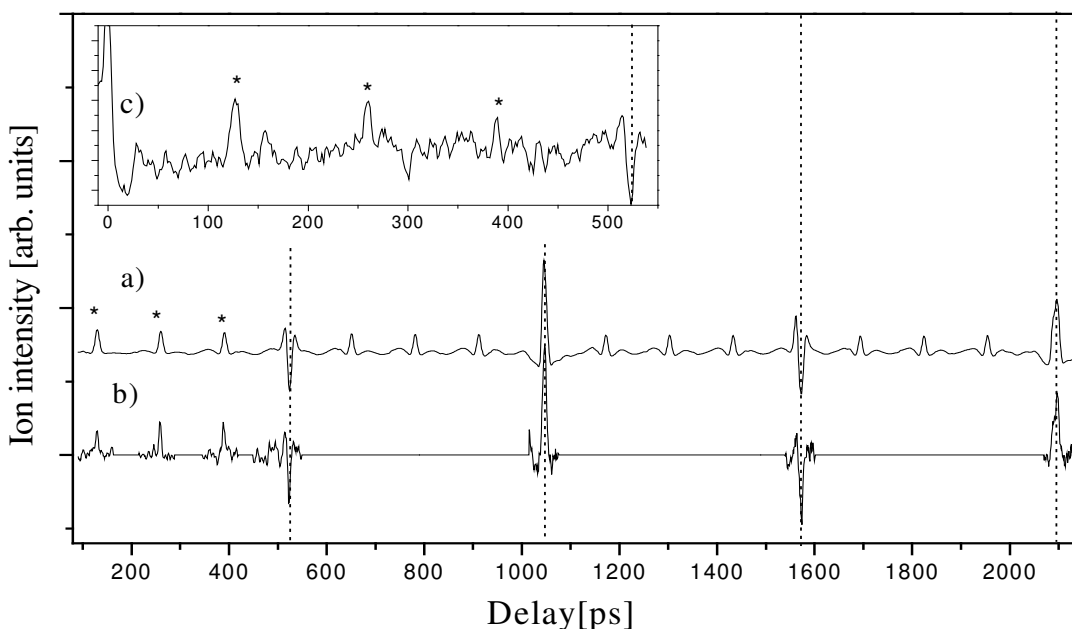
7.2.1 RCS by (1+1') PPI of cyclohexylbenzene, electronically excited state (S_1)

Fig. 7.3 RCS spectrum of cyclohexylbenzene (CHB) by pump-probe photoionization (PPI).
a) Fitted simulation to the the (1 + 1') PPI spectrum of CHB. Parameters for the simulation are given in Table 7.1.
b) Experimental data obtained by (1+1') PPI.
c) The inset shows a continuous scan up to the first J-type half-recurrence with strong K-type transients.

For the (1 + 1') pump-probe photoionization measurements (Fig. 7.3 b,c) the pump pulse was centered at the 0_0^0 transition (37630 cm^{-1}) and attenuated to a few μJ while the probe pulse with full energy ($\sim 30\mu\text{J}$) was redshifted (-150 cm^{-1}) in comparison to the 0_0^0 transition. The laser beams cross the molecular beam $\approx 10\text{ cm}$ downstream of the nozzle behind a skimmer in a differentially pumped chamber in the ionization region of a home-built Wiley-McLaren type TOF-MS. The ion-current of mass 160 amu is recorded with a boxcar integrator as a function of time delay between pump and probe pulse. The regions of the first four K- and J-type rotational recurrences (RRs) were scanned with a step size of 1 ps, and a delay range from 0 - 2.2 ns was chosen for the measurement. Each scan was repeated five times in alternating directions. The continuous scan (see inset on Fig. 7.3) in a

delay range from 0 – 540 ps was received with a step size of 1.5 ps. Smoothing of the raw data with 3 ps adjacent averaging was employed.

Two methods of analysis for the recorded (1 + 1') PPI RCS spectra were employed. The first was a linear regression analysis of transients' peak positions assuming that a nearly symmetric prolate top description is valid. For the second approach a complete fitting of the simulated spectra to the experimental data was applied. In the linear regression, the peak positions of the three K- and four J-type transients were determined. As a result of the analysis of peak positions as a function of recurrence number, one can obtain:

$$t_K = 1/[4A-2(B+C)] = 130.8 \pm 0.7 \text{ ps},$$

$$t_J = 1/2(B+C) = 524.3 \pm 0.5 \text{ ps.} \quad (7.1)$$

The error margins correspond to the statistical error of the linear regression procedure. From the experimental data the following rotational constants of the electronically excited state (S_1) configuration could be estimated: $A' = 2388 \pm 13$ MHz and $(B'+C') = 953.7 \pm 0.9$ MHz (see Tab. 7.1).

The appearance of two types of RRs in the (1 + 1') PPI RCS spectra can be understood from the perpendicular alignment of the $S_0 \rightarrow S_1$ transition dipole moment (TM) with respect to the figure axis (*a*-axis, see Fig. 7.1) similar to *p*CHA [SmM90, STT93, WRB00]. In the symmetric top notation, for a perpendicular transition the selection rules are: $\Delta K = \pm 1$ and $\Delta J = 0, \pm 1$ [Her45]. Therefore, it can be concluded that a near-prolate symmetric top such as CHB should exhibit two types of the RRs [Fel92]. The first ones are J-type transients, resulting from coherences $|\Delta J| = 1, 2$, $|\Delta K| = 0$ with the time spacing t_J (Eq. 7.1), they can also be observed for parallel cases of the TM. The second type of RRs (K-type) is induced by the perpendicular transition, resulting in coherences of $|\Delta J| = 0$, $|\Delta K| = 2$. The K-type transients appear with a time separation t_K , as given in equation 7.1.

The experimental data were also fitted by a simulation based on the assumption that CHB is a rigid asymmetric top (i.e. $D_J = D_{JK} = 0$). The input parameters for this simulation were the rotational constant A' and sum of the constant $(B'+C')$, the alignment of the transition dipole moments (for the $S_1 \leftarrow S_0$ and $X^+ \leftarrow S_1$ transitions) within the molecular frame and the temperature of the sample. Fig 7.3a shows the fitted simulation based on this procedure. The simulation reproduces the positions, shape and polarity of the transients very well.

Table 7.1: Results of the time-resolved fs DFWM and (1+1') PPI experiments on cyclohexylbenzene for the ground and the excited states respectively: rotational constants A , B , C in MHz, CD constants D_J , D_{JK} in Hz, recurrence times, temperature $Temp.$, and Ray's asymmetry parameter κ . Comparison with *ab-initio* calculation. *Ab-initio* calculations were performed at B3LYP/6-311+G(2d,p) level for the ground state (S_0) and at CIS/6-31G(d) for the electronically excited state (S_1).

	Fs DFWM (<i>ground state</i>).	Calculation B3LYP/6- 311+G(2d,p)	(1+1') PPI (<i>excited state</i>).		Calculation CIS/6-31G(d)
	Fitting data ^{b)}		Lin. Regression	Fitting data ^{c)}	
A	2453 ^{a)}	2453	2388±13	2396±2	2426
B	481.80 ± 0.02	479.1		479.2	477.7
C	--	478.6		474.9	477.1
(B+C)	963.6	957.7	953.7±0.9	954.1±1.5	953.8
D_J	15.4 ± 0.4				
D_{JK}	159 ± 18				
t_J [ps]		522.1	524.3±0.5		524.2
t_K [ps]		127.6	130.8±0.7		128.2
TM or φ ^{d)}	-0.464 ^{a)}	-0.218		(\perp ,H)	(\perp ,--)
Temp. [K]	310 ^{a)}			11	
κ	-1.0	-0.9995		-0.996	-0.998

^{a)} Fixed.

^{b)} Fitting of the fs DFWM spectra was performed with the assumption that CHB is a nonrigid prolate symmetric top (i.e. $B = C$, or $\kappa = -1$). This assumption has been used for acceleration of the fitting procedure.

^{c)} Fitting of the (1+1') PPI spectra was performed with the assumption that CHB is a rigid asymmetric top (i.e. $D_J = D_{JK} = 0$).

^{d)} Alignment of the transition dipole moments (TM) for the (1+1') PPI and parameterised PT φ for the fs DFWM experiments.

The sum ($B' + C'$) of the rotational constant has been used because it was not possible to determine the constants B' and C' independently due to the symmetric top nature of CHB. Thus only the ($B' + C'$) value is given with an error bar (see Tab. 7.1). The (1 + 1') PPI RCS experiment also provides information about the alignment of the transition dipole moments: (i) between ground and excited electronic ($S_1 \leftarrow S_0$) states and (ii) between $X^+ \leftarrow S_1$ states. The first electronic TM was assumed to be in the plane of the benzene ring along the b -axis. This assumption is in accordance with transition dipole moment of p -CHA $S_1 \leftarrow S_0$ [CHK69, RWL00] and also justified by the *ab-initio* calculation on CHB for the electronically excited state (see Tab. 7.1). In order to reproduce the polarity and the ratio of

intensities of the J- and K-types transients the alignment of the second $X^+ \leftarrow S_1$ transition dipole moment was used as a fitting parameter. As a result, of this procedure, the transition was obtained to be in the a, c plane, and assigned to a hybrid (H) transition. It must be emphasized, that since CHB is very close to the prolate symmetric top limit ($\kappa(S_1) = -0.996$, see Tab. 7.1) it is difficult to distinguish between the b and c axes, in particular, how they are related to the molecule structure. This can lead to an error in the definition of the TM orientation in relation to the molecular frame. The fitting results of the $(1 + 1')$ PPI RCS spectra and comparison with the *ab initio* calculations for the electronically excited state at CIS/6-31G(d) level of theory are summarized in Table 7.1.

7.2.2 RCS by fs DFWM of cyclohexylbenzene, ground electronic state

For cyclohexylbenzene no ground state RCS data could be obtained by TRFD due to inefficient cooling in the beam expansion. The recorded traces exhibited a strong and persistent ‘perturbation’ by vibrational quantum beats with a period of 9.2 ps corresponding to a splitting of 3.6 cm^{-1} , so that possible rotational coherence features could not be analyzed [Wei00, Rie02]. Therefore, fs DFWM was applied for the study of CHB structure in the electronic ground state.

CHB, as well as all molecules considered in this chapter, has a low vapor pressure at room temperature ($<0.1 \text{ mbar}$) and therefore have to be heated in a gas cell in order to compensate for the square dependence of the signal intensity in fs DFWM spectroscopy. Thus, the investigation of CHB in a heat pipe oven (section 3.3.2) at elevated temperature (310K) has been performed. As buffer gas argon (ca. 10 mbar) was used. CHB (ACROS Organics, purity 98%, heated to $\approx 310 \text{ K}$) was used without further purification. Scans around the first four J-type transients (ca. 20 ps wide) were recorded with the step size of 0.1 ps. Note that, there were no other spectral features detected in the fs DFWM spectrum of CHB, which could be assigned as RRs of the other types. The femtosecond laser pulse ($\sim 320 \text{ fs}$ [FWHM autocorrelation]) and energy 50-150 $\mu\text{J/pulse}$ has been used for RRs measurements

In Fig. 7.4a the RRs of J-type for CHB are depicted and compared to a fitted simulation (Fig. 7.4b) based on a nonrigid symmetric prolate rotor model (with assumption that PT possesses near-prolate symmetry $\tilde{\beta}_{AA} > \tilde{\beta}_{BB} \approx \tilde{\beta}_{CC}$), as described in the section 2.4.3.2. The

assumptions are made in order to accelerate the fitting procedure. Note that, in order to account for all thermally populated rotational levels, it was necessary to calculate up to 300 J levels. That significantly increased the computing time for the fitting procedure. These assumptions are totally justified by the following facts. First, CHB is very close to the prolate symmetric limit (Ray's parameter $\kappa = -0.9995$). Second the simulation shows independence of the J-recurrences positions and shapes from parametrized PT angle φ in case of the near-symmetric tops. Finally the value $\varphi = -0.22$ (Tab. 7.1) obtained from DFT calculation is very close to the assumed one.

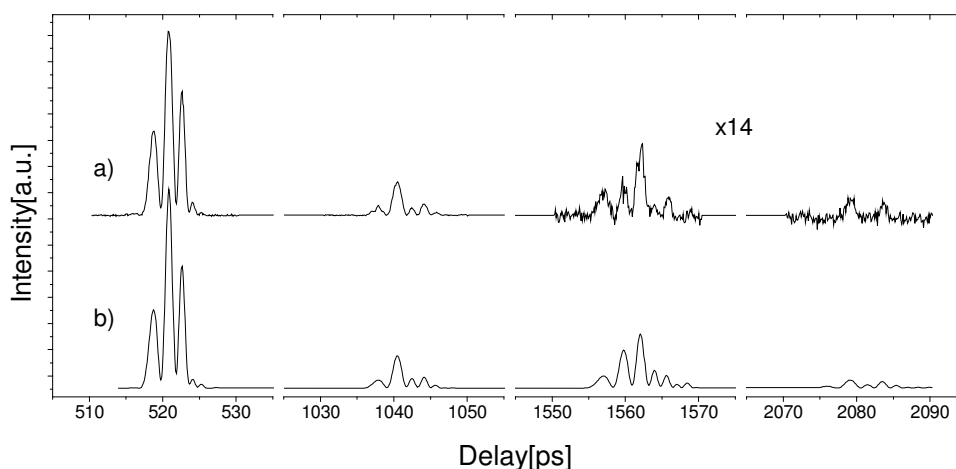


Fig. 7.4 The fs DFWM spectrum of cyclohexylbenzene (CHB) in the heated gas cell ($T \approx 305$ K).

- a) Experimental spectrum
- b) Fitted simulation based on a nonrigid symmetric rotor model (300 J levels).

It can be seen that all recurrences exhibit a modulated structure, which can be attributed to the influence of centrifugal distortion (CD) and is reproduced nicely in the spectral simulation. The fitting results are listed in Table 7.1 together with data from the DFT calculation.

The agreement of the rotational constants obtained from the experiment with the calculated ones is good and, thus, it can be inferred that the cyclohexyl group is found in the chair conformation and that the phenyl and the cyclohexyl ring are oriented perpendicularly (see also Fig. 7.1). From DFT calculation it was also obtained, that this structure is a global minimum structure, with energy $E = -467.062$ hartrees, which is ~ 26 kJ/mol smaller than the energy of the next possible conformer with the cyclohexyl ring in twisted form.

As a result, of the fitting procedure values for the CD constants D_J and D_{JK} were also obtained within assumption that CHB is prolate symmetric top. Since it is the first rotationally resolved spectrum of this molecule, there is no data on rotational and CD constants available in the literature for the comparison.

Moreover, from the comparison of the results of calculations for the ground and electronically excited states, the changes in the geometry upon electronic excitation can be extracted. The smaller, in general, rotational constants (i.e. bigger moments-of-inertia) in S_1 state are mainly result of the enlarged aromatic ring ($\sim 1\%$), while the geometrical parameters of the cyclohexyl ring are not changed upon excitation. The enlargement effect of aromatic molecules upon electronic excitation is a general effect, and can be explained by the transition of the π -electron from the highest occupied molecular orbital (HOMO) to the antibonding lowest unoccupied molecular orbital (LUMO). This transition typically weakens the bonding in the molecule, leading to an excited state with an expanded geometry. For example, benzene has approximately $\sim 4\%$ smaller rotational constant B' in electronically excited state ($S_1 6_0^1$) than in the ground state S_0 [OMH99].

7.3 *para*-Cyclohexylaniline

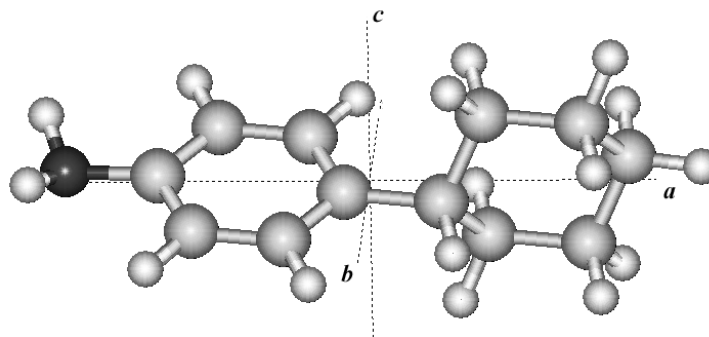


Fig. 7.5 *para*-Cyclohexylaniline ($C_{12}H_{17}N$) structure with principal axes of inertia.

Para-Cyclohexylaniline (*pCHA*), shown in Fig. 7.5, is a prolate near-symmetric top with the figure axis (*a*-axis) almost in line with the C–N bond. The transition dipole moment of this molecule is aligned nearly perpendicular to the *a*-axis, as in aniline itself [CHK69]. Due to these properties, *pCHA* has been considered as a very important species for RCS [STT93], and it served as a textbook example [Hol98]. McDonalds and co-workers have received the first RCS spectrum of *pCHA* by time-resolved fluorescence depletion (TRFD) [SmM90]. Three sets of RRs were assigned in the RCS trace. Two of them with time separation 697.5, and 122 picosecond were rationalized as J- and K-types transients of the *pCHA* in the electronically excited state. The origin of the peaks with a spacing 125.8 ps was not assigned in that study [SmM90]. This problem of assignment occurred because the authors did not take into account that the single-wavelength TRFD technique detects both ground and excited state coherences (see Section 2.3.1). This type of phenomenon has been analyzed by Hartland and co-workers for several pump-probe combinations [HCF91]. Later, these RRs with time spacing 125.8 ps were determined as K-type transients from the ground state coherence. The problem of assignment was solved using time-correlated single photon counting (TCSPC) technique, since this approach is sensitive only to the excited state [STT93]. The molecular parameters of *pCHA* were also measured for the ground and excited configurations separately with high resolution by Weichert et al. [WRB00]. For this purpose time-resolved stimulated Raman-induced fluorescence spectroscopy (TRSRFD) and time-resolved stimulated emission pumping (TRSEP) was used. The structure of *pCHA* in

crystalline phase has also been studied by X-ray diffraction [RDW00]. The authors compared their data with results of the gas phase study [WRB00] and *ab initio* calculations at MP2/6-31+G(d) level of theory. Thus, since the molecular parameters of *p*CHA are very well known and it exhibits a strong RCS signal, this molecule seems to be a good candidate for the testing the fs DFWM technique in the high temperature regime.

7.3.1 RCS by fs DFWM of *para*-Cyclohexylaniline

Similar experimental conditions as for CHB (section 7.2.2) were used. *p*CHA (Lancaster, purity 97%) was heated up to ≈ 420 K in the heat pipe oven and the first three J-type transients were recorded with the step size of 0.1 ps.

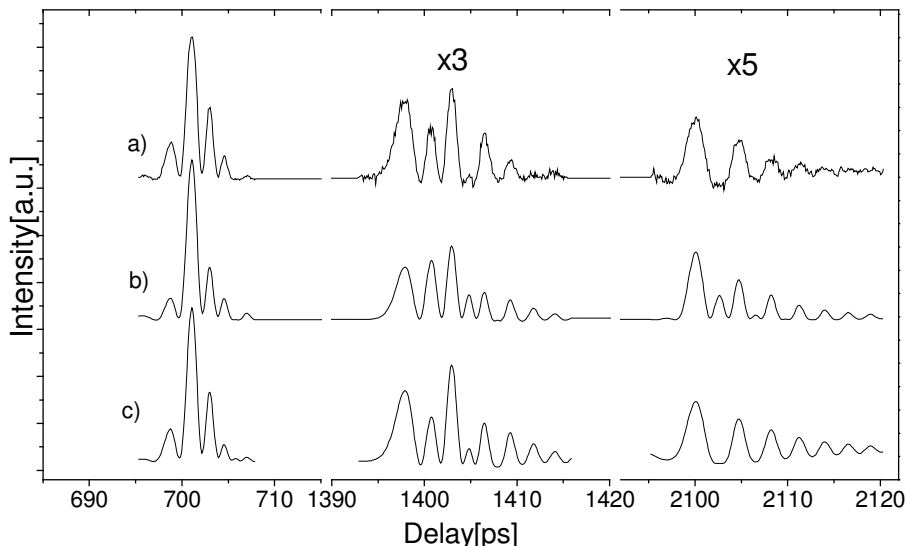


Fig. 7.6 The fs DFWM spectrum of *p*CHA in the heated gas cell ($T \approx 420$ K).

- a) Experimental spectrum.
- b) Fitted simulation of the spectrum based on a nonrigid symmetric model (400 J levels). The three recurrences have been fitted simultaneously.
- c) Fitted simulation (400 J levels). Every recurrence was fitted separately with respect to the background parameter k . Explanation, see text.

The experimental J-type transients for *p*CHA are plotted in Fig. 7.6a. In contrast, to the resonant TRFD measurements [SmM90, WRB00], the fs DFWM trace consists of only the J-type transients. This originates in the symmetry of the PT. In case of *p*CHA the PT with near prolate “symmetry” (i.e. $\tilde{\beta}_{AA} > \tilde{\beta}_{BB} \approx \tilde{\beta}_{CC}$, $\varphi = -0.28$ (Fig. 2.12)) was obtained from *ab-*

initio calculation at B3LYP/6-311+G(2d,p) level of theory. The RRs exhibit a rich modulated centrifugal distortion structure, which is reproduced in the fitted spectral simulations given in Figs. 7.6b and 7.6c. Simulation of the fs DFWM signal (Fig. 7.6a) was done with the assumption that *p*CHA is a nonrigid symmetric top. Up to 400 J levels were calculated in order to take in to account all thermally populated rotational states. The simulated recurrences depicted in Fig. 7.6b were all fitted simultaneously with one parameter set. Since the concentration of *p*CHA was not constant during the measurement of the different recurrences an improved simulation was obtained by fitting the recurrences separately (Fig. 7.6c). However, in this separate fitting only a background parameter *k* (cf. section 4.2.4) was varied, since an effect of the RRs shapes perturbation was also found to be concentration dependent. Note, that neither rotational nor CD constants are different between the simulated spectra in Figs. 7.6b and c.

Table 7.2: Fitting results for fs DFWM experiments of *p*CHA for the ground state: rotational constants *A*, *B*, *C* and CD constants *D_J*, *D_{JK}*. Comparison with *ab initio* calculation and TRFD measurements, Ref. [RWL00]. Fitting was performed with assumption that *p*CHA is a nonrigid prolate symmetric top (i.e. *B* = *C*).

	fs DFWM [This work]	TRFD ^{b)} , Ref.[RWL00]	Calculation B3LYP/6- 311+G(2d,p)
A [MHz]	2406 ^{a)}	2407.4 ± 0.6	2417
B [MHz]	357.73 ± 0.02	358.5 ± 0.3	355.6
C [MHz]	--	357.5 ± 0.3	354.6
B+C	715.46	714.8 ± 0.4	
D _J [Hz]	7.0 ± 0.3		
D _{JK} [Hz]	196 ± 30		
κ	-1.0	-0.998	-0.999

^{a)} Fixed.

^{b)} Time-resolved fluorescence depletion (TRFD) measurement in a supersonic expansion (*T* ≈ 8 K).

The extracted fitting parameters are listed in Table 7.2. The sum of the rotational constants (*B*+*C*) agrees very well with former results on this molecule obtained in a supersonic expansion experiment (*T* ≈ 8K) by time-resolved fluorescence depletion (TRFD) [RWL00]. It shows that in the high temperature (420K) fs DFWM measurements the global minimum structure of *p*CHA was registered, because this structure is usually the only populated one in a supersonic jet. The rotational constants are also compared with the results from a DFT calculation (see Table 7.2). Since rotational constants are in reasonable agreement with data

obtained from our experiment, the global minimum structure ($E = -522.439$ hartrees) from DFT calculation at B3LYP/6-311+G(2d,p) level of theory can be considered as a good representation of the *p*CHA molecule in the gas phase. Here the inter-ring conformation is the same as for CHB. Aromatic and cyclohexyl group are oriented perpendicularly, with the cyclohexyl group in the chair conformation.

In addition, the values of the CD constants D_J and D_{JK} have been obtained within the symmetric top approximation. As in case of CHB, there is no data for comparison available in literature, because the molecules with 26-30 atoms and rotational constants of ca. 300-600 MHz (0.01- 0.02 cm⁻¹), like cyclohexylbenzene and *para*-cyclohexylaniline, are on the border of feasibility for the traditional frequency-based spectroscopies.

7.4 Nicotine

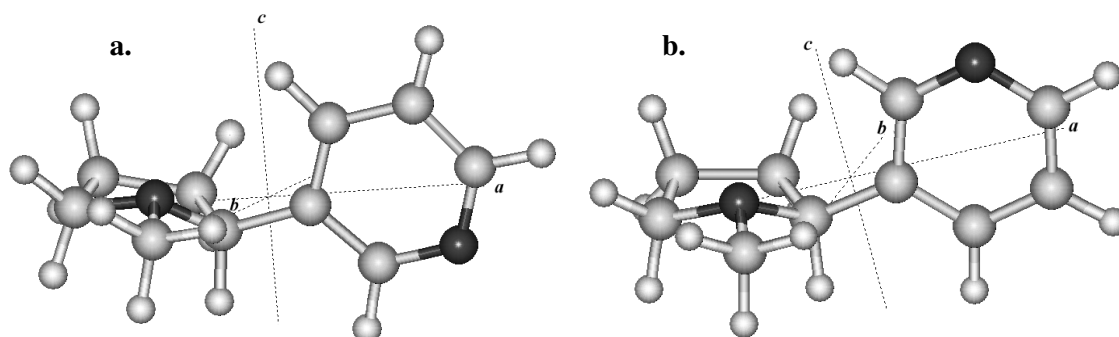


Fig.7.7 Nicotine ($C_{10}N_2H_{14}$) structure with the principal axes of inertia. Two rotamers: **a.** (eq,eq,syn); **b.** (eq,eq,anti). Explanation of nomenclature, see text.

There is only little experimental information available on the gas phase structure of nicotine (Fig.7.7). The investigation of the nicotine structure is complicated because it can have many stable conformers arising from the combination of the several sources of flexibility. First, the pseudorotation of the pyrrolidine ring that is responsible for the envelope and twisted forms of the ring, and the equatorial and axial positions of the pyridine ring. Second, inversion of the N atom in the pyrrolidine ring that is responsible for the equatorial and axial positions of the methyl group. And third, rotation around C–C bond between the rings. Only recently, nicotine was studied by means of electron diffraction and two rotamers with respect to the ring connecting bond have been assigned (see Fig. 7.7) [TFE02]. The rotamers were assigned to the (eq,eq,syn) (fig. 7.7a) and (eq,eq,anti) (fig. 7.7b) conformation, where the abbreviation stands for the equatorial position of the methyl group and the pyridine ring and the dihedral angle related to the inter-ring connection [TFE02]. The syn rotamer exhibits the larger N-N distance and is also the more stable form, by ca. 0.5 kcal/mol [TFE02]. Since for such a large molecule a complete analysis by electron diffraction is not possible, several constraints and assumptions had to be put forward. Thus, there is still a need for independent structural information on nicotine in the gas phase, which might help to elucidate its conformation.

7.4.1 RCS by fs DFWM of Nicotine

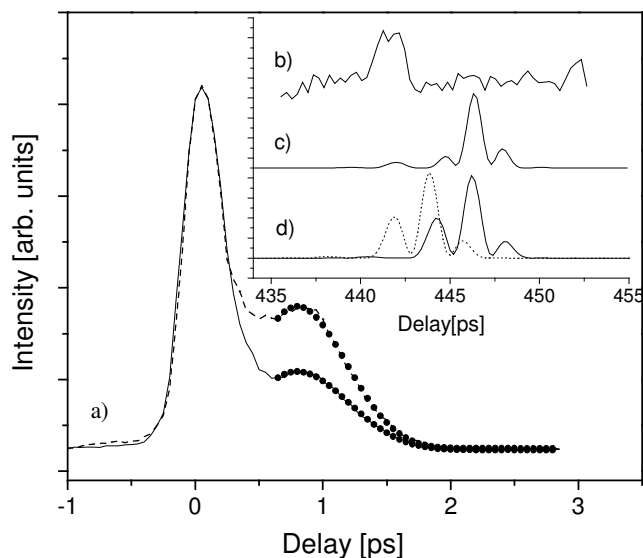


Fig. 7.8 Fs DFWM of nicotine.

a) Early time fs DFWM response from nicotine at different temperatures; solid line - T_1 , dashed line - T_2 . Fitted simulation (full circles), with assumption $\bar{B} = 1/2 (B+C) = 563$ MHz. Fitting results: $T_1 = 340$ K, $T_2 = 380$ K.

Inset: Comparison of the experimental and simulated trace for the first recurrence.

b) Experiment.

c) Overlap of the spectral features from both rotamers (eq, eq, syn) and (eq, eq, anti) with concentration ratio 2:1. Parameters for simulation from Table 7.3.

d) Simulation for the two rotamers of nicotine. Rotamer (eq, eq, syn) - solid line; rotamer (eq, eq, anti) - dotted line.

The fs DFWM measurements of nicotine ((3-((S)-N-methyl-2-pyrrolidinyl)pyridine, ALDRICH, purity 98%) have been done in the heat pipe oven, which was preliminary filled with 10 mbar of argon as a buffer gas. The substance was heated up to ~ 380 K. The region of the early time response from nicotine vapor was obtained with a step size 0.05 ps (Fig. 7.8), while the fs DFWM trace in the region of the first J-type rotational recurrence was scanned with 0.2 ps step. The result of the averaging over ten scans in alternative directions in region of delay time 435 – 455 ps is presented in Fig. 7.8b.

The four-wave mixing signal of nicotine was very weak and only one rotational recurrence was clearly obtained. A further complication of the nicotine measurement was, that after a short measurement time a strong background signal appeared that obscured the four-wave mixing experiments. This signal was attributed to some photochemical process and also to

concentration instabilities in the cell. It was difficult to reach a high-temperature equilibrium for this substance

The time zero transient is depicted in Fig. 7.8a for two different temperatures together with a fit of the inertial part of the transients (black dots in Fig. 7.8a). For the fit only the temperature was varied and the rotational constants have been fixed to the results of the DFT calculations (Tab. 7.3), which are in good agreement with the former calculations [ELD00, TFE02]. A good reproduction of the inertial feature with increasing temperature is observed. Thus, one can conclude that the observed spectral signal clearly stems from nicotine. However, there is not enough data to perform an extraction of the rotational constants.

Table 7.3: Results of DFT geometry optimization (B3LYP/6-311+G(2d,p)) for the two rotamers of nicotine. Calculations performed by D. Kosov (University Frankfurt/M.).

	(eq,eq,syn) ^{a)}	(eq,eq,anti) ^{a)}
A [MHz]	2048	2034
B [MHz]	577	580
C [MHz]	546	549
κ	-0.959	-0.958
ΔE [kJ mol ⁻¹] ^{b)}	0.0	2.1477
abundance [%] ^{c)}	67.4	33.6

^{a)} Rotamers with respect to ring connecting bond. Nomenclature see text and Ref. [TFE02].

^{b)} Absolute value of the energy is $E = -499.1279979$ hartrees for the (eq,eq,syn) conformer (Fig.7.7a).

^{c)} Estimated from the energy difference, ΔE assuming the Boltzmann distribution at 380K.

At a time delay of 442 ps another feature was found (Fig. 7.8b) which appears closely to a position where the first J-type recurrence of nicotine is expected. From recent electron diffraction experiments and *ab initio* calculations two rotamers with respect to the inter-ring axis, i.e., (eq,eq,syn) and (eq,eq,anti) with an abundance of approx. 2:1, were found [ELD00, TFE02]. A simulation of the J-type recurrences of both rotamers, based on the results of our DFT calculation, is given for comparison in Fig. 7.8d.

However, since a coherence spectroscopy is applied here, an overlap of the spectral features from both rotamers is not necessarily constructive. One has to overlap ‘wavefunctions’ of sinusoidal type before squaring (cf. Eq. 2.36), which can result in destructive interference,

i.e., damping of spectral features (Fig. 7.8c). This interference effects are possible between different types of molecules, as has been documented in the literature [Dan01, RSK98]. A tentative interpretation of the spectral feature at 442 ps is, that it stems from an interference between the signal ‘wavefunctions’ of the two rotamers of nicotine, probably it is related to the most abundant (eq, eq, syn) rotamer. This is supported by the similarity in shape of the simulated (Fig. 7.8c) and experimental trace (Fig. 7.8b). The shift in position is ascribed to the absolute accuracy of the DFT calculation, whereas the relative accuracy for both rotamers should be higher.

To prove this preliminary assignment more experimental data are necessary. Unfortunately, no features of the second J-type recurrence under the current experimental conditions were obtained. Probably, a shift in the experimental wavelength could be helpful in order to avoid the photochemical perturbations that are limiting the data acquisition time.

Additionally it has to be taken into account, that the asymmetry of nicotine is the largest among the molecules studied here. This fact together with the distribution of population over two rotamers might explain the low signal intensity for nicotine in comparison to CHB and *p*CHA.

7.5 Conclusions

From the results presented in this chapter, the following conclusions can be drawn.

(i) Rotationally resolved spectroscopy of large two-ring molecules at elevated temperatures is possible and rotational and CD constants can be obtained in this way. The RRs of CHB and *p*CHA received from fs DFWM experiments have been analyzed in the nonrigid symmetric prolate rotor approximation and the rotational and CD constants of the ground state have been extracted. For CHB and *p*CHA the obtained rotational constants are in good agreement with experimental results available in the literature. The theoretical results support a nearly perpendicular conformation of the aromatic vs. the cyclohexyl ring for both systems.

(ii) For nicotine the spectral intensity was too small for a detailed analysis. However, specific spectral features could be assigned and analyzed. The weak spectrum of nicotine is rationalized in terms of its asymmetry and the overlapping recurrences of two rotamers.

(iii) The combination of fs DFWM spectroscopy and a heat pipe oven for the sample preparation provides a general approach towards large molecular and in particular biomolecular systems. No window problems appeared, even at high laser intensities.

(iv) Cyclohexylbenzene was additionally studied by the (1 + 1') pump-probe photoionization. From the complete simulation of the measured spectra precise values of the rotational constants of CHB in the first electronically excited state (S_1) were extracted. In addition to the rotational constants of the molecule, the alignment of the $X^+ \leftarrow S_1$ transition dipole moment within the molecular frame can be estimated. This transition was found to be in the plane of the *a* and *c* axes-of-inertia, and assigned as a hybrid transition. Moreover, the change of the rotational constants upon electronic excitation was observed and rationalized by enlargement of the aromatic ring of CHB in the electronically excited state.

Chapter 8

8 Summary

A new experimental setup, for pump-probe fs DFWM measurements, which is based on a femtosecond laser system, has been constructed. It allows for the investigation of molecular species in the gas phase at different temperatures, from ~30 K in a seeded supersonic jet up to ~500 K in a heat-pipe oven. In comparison to other RCS methods the employed fs DFWM technique is less complicated and gives much higher signal-to-noise ratio [BFZ86, FeZ95a, CKS89, CCH90, HCF91, WRM02, Rie02].

A general computer code for the simulation of fs DFWM spectra of nonrigid asymmetric top molecules has been developed. This new DFWM code in combination with a non-linear fitting routine allows one to determine rotational and centrifugal distortion constants and obtain information on the polarizability tensor components from the experimental spectra.

Fs DFWM spectroscopy was successfully applied to the medium-sized molecules benzene and benzene-d₆ in a gas cell and in a supersonic jet. The spectrum from a seeded expansion has been measured up to delay time of 3.9 ns (restricted by the length of the delay stage) with excellent signal-to-noise ratio (10^2 - 10^3). In that way 87 and 72 J-type transients have been recorded for benzene and benzene-d₆, correspondingly. A relative accuracy on the order of 10^{-5} has been achieved for the rotational constant. From the room temperature experiments, precise values of centrifugal distortion constants D_J and D_{JK} have been extracted. The literature data for cyclohexane have been revised and a new precise rotational constant B_0 has been obtained, which is (+5.5 MHz) shifted from the one reported in the former Raman investigation by Peters et al. [PWW73].

Additionally, high-level *ab initio* calculations of cyclohexane have been carried out using a large number of basis sets at several levels of theory. In particular, the vibrational averaging effects have been examined in order to critically compare the experimentally determined and theoretically evaluated rotational constants. The contribution of highly symmetric vibrational modes to vibrational averaging effects was clarified.

More structural information could be obtained from fs DFWM measurements of asymmetric top species, since different type of rotational recurrences can appear, and all three rotational constants (A , B , C) can be extracted. On the other hand the analysis of the asymmetric top spectra is no longer trivial. In fact the simple formula for rotational recurrence periods of symmetric top species (Tab. 2.1) can not be applied to asymmetric top molecules. Thus, in order to extract high-resolution data for asymmetric species, a complete fitting of the experimental spectra is necessary. The fs DFWM and (1+2') PPI method have been applied to the asymmetric top molecules pyridine in the ground (S_0) and *p*DFB in the S_0 and electronically excited (S_1) states. By fitting the measured fs DFWM spectra the rotational and centrifugal distortion constants have been extracted with good precision and the value of the parametrized polarizability angle of *p*DFB was obtained.

In this work, the first application of fs DFWM spectroscopy to a molecular cluster has been reported. Also, the chemical equilibrium between monomeric and dimeric species was studied. In particular formic and acetic acid have been investigated in a gas cell and in a supersonic expansion. Many spectral features have been observed and analyzed in the fs DFWM spectrum of formic acid vapor in a gas cell at room temperature. Most of them were attributed to rotational recurrences of the formic acid monomer, but also spectral feature originating from the formic acid dimer of O-H...O/O...H-O type have been detected and analyzed. From the fitted simulation, the rotational and centrifugal distortion constants, and parametrized polarizability angle were extracted for the dimeric structure of O-H...O/O...H-O type. With the assumption of unperturbed monomers a center-of-mass distance of $R = 2.990 \pm 0.001 \text{ \AA}$ for the monomers within the dimer has been calculated from the spectroscopic results. This distance is 0.028 \AA smaller than that reported from electron diffraction [ABM69]. Thus, the centers-of-mass distance was assigned as the main point of disagreement between results of fs DFWM and electron diffraction experiments.

In contrast to formic acid, acetic acid shows strong recurrences from dimeric species even in the fs DFWM spectra at room temperature. This is explained in terms of different symmetry

of the moments-of-inertia tensor, which modulates the intensity of RRs (the fs DFWM signal is in general stronger from symmetric species). Due to the symmetric nature of the acetic acid dimer, only the sum ($B+C$) of the rotational constants has been extracted. The changes of geometrical parameters upon dimer formation have been analyzed for, both, formic and acetic acid.

A heat-pipe oven has been used in order to overcome the main drawback of fs DFWM spectroscopy – the square dependence of the signal intensity on the sample number density. Two-ring molecules (cyclohexylbenzene, *para*-cyclohexylaniline and nicotine) with low vapor pressure (<0.1 mbar) at room temperature have been investigated. From the analysis of the experimental and *ab-initio* results for CHB and *p*CHA a nearly perpendicular conformation of the aromatic vs. cyclohexane ring for both system is inferred. The enlargement of the benzene ring of CHB in the electronically excited state (S_1) has been found to cause the smaller rotational constants in S_1 . This conclusion has been drawn from the comparison of the ground and electronically excited state experimental rotational constants in combination with *ab-initio* calculations. The extraction of precise structural information for nicotine was not possible due to its weak fs DFWM signal. However, the fact that fs DFWM technique can be applied to conformational analysis of molecular species in an equilibrium mixture opens other applications for this kind of spectroscopy.

In general the results obtained in this work show that the fs DFWM technique, being an experimental implementation of RCS, provides one with an important tool for structural analysis of molecular species in the gas phase in particular for the species to which microwave spectroscopy can not be applied. It gives spectra with excellent signal-to-noise ratio even at low number density samples expanded in a seeded supersonic jet. It provides an alternative and innovative approach towards rotational Raman spectroscopy of large polyatomic molecules applicable under various experimental conditions (broad temperature and pressure range). With the introduction of femtosecond (10^{-15} s) laser pulses (usually picosecond (10^{-12} s) laser pulses were used in RCS) an improvement in time-resolution and therefore in precision for the rotational constants by more than one order of magnitude has been achieved. Molecular systems in the ground electronic state without permanent dipole moment and chromophore can be studied with high precision, providing thereby molecular benchmark systems for the electronic structure theory.

As has been shown, the study of molecular clusters by fs DFWM spectroscopy is possible, but its potential are restricted by the square dependence of the fs DFWM signal from the sample number density, which is even more important for supersonic jet expansions. Here, the application of near-resonant and resonant FWM schemes should help in order to compensate for the low sample concentration.

With the introduction of the heat pipe oven for fs DFWM experiments, the investigation of large nonvolatile molecules under equilibrium conditions is possible now. In our laboratory the first results on the structural analysis of different conformers of pyrrolidine in the gas phase have been obtained [MaR04]. This method can have even more prospects for the structural investigations of large molecular species in combination with new non-thermal gas phase sources for nonvolatile molecules, like laser desorption [CTL89], laser ablation [MHL83], electrospray [FMM90], laser induced liquid beam ion desorption [KAB96, Sob00] etc.

A very recent application of the fs DFWM technique is the investigation of the influence of strong laser fields on molecular gas phase sample, which could range from active alignment [PPB03] over molecular deformation to field ionization [CSD03].

In regards to future development in fs DFWM spectroscopy for more complex molecules one has to take into account, how large amplitude motions such as the van der Waals vibrations or internal rotation (see section 6.4.2) affect the rotational coherences.

In any case, femtosecond Degenerate Four-Wave Mixing as experimental implementation of Rotational Coherence Spectroscopy can be considered as an innovative, developing, and powerful method for the structural investigation of the molecular species, which are hard to study by classical frequency-resolved spectroscopy [FeZ95a, Dan01, Rie02].

Zusammenfassung

In der vorliegenden Arbeit wird nicht-lineare Femtosekunden pump-probe Laserspektroskopie zur strukturellen Untersuchung von mittelgroßen und großen Molekülen und molekularen Aggregaten benutzt. Die dabei verwendete Methode, nämlich das Femtosekunden zeitaufgelöste entartete Vierwellenmischen (*femtosecond degenerate four-wave mixing*, fs DFWM), liefert dabei Spektren, genauer: transiente Zeitspuren, aus denen präzise Rotationskonstanten, Zentrifugalverzerrungs-Konstanten sowie Informationen über den Tensor der Polarisierbarkeit des entsprechenden molekularen Systems erhalten werden. Zusätzlich sind diese Spektren abhängig von der Temperatur und dem Druck. Die verwendete Methodik stellt das Analogon zur Rotations-Raman-Spektroskopie in der Zeitdomäne dar und kann im größeren Rahmen der Rotationskohärenz-Spektroskopie (*rotational coherence spectroscopy*, RCS) zugeordnet werden. RCS-Methoden basieren auf der direkten Bestimmung von charakteristischen Rotationszeiten und sind insbesondere auf große und komplexe molekulare Systeme anwendbar, bei denen Methoden in der Frequenzdomäne, aufgrund der hohen spektralen Liniendichte, problematisch werden. Die RCS- und damit auch fs DFWM-Spektren sind durch periodische Peakstrukturen, sog. Rotations-Rekurrenzen oder Rotations-Transienten bestimmt. Letztere können von unterschiedlichem Typ (J-, K-, A-, C- etc.) sein, wobei entsprechend unterschiedliche algebraische Kombinationen von Rotationskonstanten zugrunde liegen. Da die somit ermittelten Rotationskonstanten als massegewichtete, gemittelte molekulare Koordinaten angesehen werden können, enthalten sie die wesentlichen Strukturinformationen. Durch den Vergleich mit *ab initio* Strukturoptimierungen können somit molekulare Geometrien abgeleitet werden. Weiterhin werden Benchmark-Systeme für einen harten Test der theoretischen Methoden bereitgestellt.

Für die Aufnahme der fs DFWM Spektren wurde ein neuer experimenteller Aufbau, basierend auf einem Femtosekunden-Lasersystem, installiert. Dieser erlaubt die Untersuchung molekularer Spezies in der Gasphase bei unterschiedlichen Temperaturen, variierbar von ca. 30 K in einer Überschalldüsenstrahlexpansion bis zu etwa 500 K in einem sog. *heat-pipe*-Ofen.

Im Vergleich zu anderen Rotationskohärenz-Methoden bietet die eingesetzte fs DFWM-Technik die Vorteile einer relativ einfachen Durchführbarkeit und eines hohen Signal-zu-Rausch-Verhältnisses [BFZ86, FeZ95a, CKS89, CCH90, HCF91, WRM02, Rie02].

Zur Simulation der fs DFWM Spektren wurde ein allgemein anwendbares Computerprogramm für nicht-starre asymmetrische Moleküle entwickelt. Dieser neue Computer-Code erlaubt es in Kombination mit einer nicht-linearen Fitroutine die Rotations- und Zentrifugalverzerrungs-Konstanten zu bestimmen sowie Informationen über den Polarisierbarkeitstensor aus dem Spektrum zu erhalten.

Die fs DFWM Spektroskopie wurde erfolgreich auf die mittelgroßen Moleküle Benzol und Benzol-d6 in einer Gaszelle und einer Überschalldüsenstrahlexpansion angewendet. Das Spektrum des verdünnten Düsenstrahles wurde bis zu einer Verzögerungszeit von 3.9 ns (lediglich begrenzt durch die Länge der Verzögerungsstrecke) mit einem exzellenten Signal-zu-Rausch-Verhältnis von 10^2 - 10^3 gemessen. Dadurch konnten 87 (72) sog. J-Typ Transienten für Benzol (Benzol-d6) aufgenommen werden. Die relative Genauigkeit der Rotationskonstanten lag dadurch bei ca. 10^{-5} . Aus den Experimenten bei Raumtemperatur wurden präzise Werte für die Zentrifugalverzerrungs-Konstanten D_J und D_{JK} extrahiert. Für Cyclohexan wurde eine neue präzise Rotationskonstante B_0 erhalten, so daß die Literaturdaten für dieses Molekül revidiert werden mußten. Der Wert der Konstanten war um +5.5 MHz gegenüber den älteren Raman-Untersuchungen von Peters et al. verschoben [PWW73], was deutlich außerhalb der experimentellen Fehlergrenzen liegt. Zusätzlich wurden für Cyclohexan *ab initio* Berechnungen auf hohem Niveau mit einer großen Zahl von Basis-Sätzen und theoretischen Methoden durchgeführt. Effekte der Schwingungsmittelung wurden im Detail untersucht, um die experimentell und theoretisch bestimmten Rotationskonstanten kritisch zu vergleichen. Hierbei wurde der Beitrag der hochsymmetrischen Schwingungsmoden zum Effekt der Nullpunkts-Schwingungsmittelung besonders deutlich.

Aus der Untersuchung asymmetrischer Kreisel-Spezies mit fs DFWM erhält man zusätzliche Informationen, da unterschiedliche Typen von Rotations-Rekurrenzen im Spektrum auftauchen können und damit die unabhängige Bestimmung aller drei Rotationskonstanten (A , B , C) möglich wird. Wie sich gezeigt hat, ist allerdings die Analyse der Spektren asymmetrischer Kreisel nicht trivial, da die einfachen Gleichungen für die Berechnung der Perioden der Rotations-Rekurrenzen (Tab. 2.1) nicht mehr angewendet

werden können. Deshalb ist für die Bestimmung hochaufgenauer Daten dieser Systeme eine komplette Simulation und ein Fit des experimentellen Spektrums notwendig. In dieser Arbeit wurde die fs DFWM- und die (1+1') PPI- (*pump-probe Photoionisation*) Methode auf die asymmetrischen Moleküle Pyridin im Grundzustand S_0 und para-Difluorbenzol (pDFB) im Grundzustand S_0 und elektronisch angeregten Zustand S_1 angewendet. Zum ersten Mal konnte dabei der Grundzustand von pDFB mit einer spektroskopischen Methode rotationsaufgelöst untersucht werden. Durch Anpassen (Fit) der fs DFWM Spektren wurden die ersten experimentellen Werte für die Rotations- und Zentrifugalverzerrungs-Konstanten sowie ein Wert für den parametrisierten Polarisierbarkeitswinkel für pDFB erhalten.

In dieser Arbeit wurden ebenfalls die ersten Untersuchungen an molekularen Aggregaten mittels fs DFWM Spektroskopie durchgeführt. Weiterhin wurde ein chemisches Dimerisierungs-Gleichgewicht untersucht. Dazu wurden Ameisen- und Essigsäure in einer Gaszelle studiert. In dem fs DFWM Spektrum von Ameisensäure-Dampf bei Raumtemperatur wurden verschiedene Typen von Rotations-Rekurrenzen identifiziert und zugeordnet. Die meisten davon konnten dem Ameisensäure-Monomer zugeordnet werden, allerdings wurden auch spezifische Transienten des Dimers mit zyklischer O-H...O/O..HO Struktur gefunden und analysiert. Aus der angepaßten Simulation konnten wiederum die entsprechenden Rotations- und Zentrifugalverzerrungs-Konstanten sowie der parametrisierte Polarisierbarkeitswinkel bestimmt werden. Unter der Annahme nicht gestörter Monomere in der Dimer-Struktur wurde aus diesen Daten ein Schwerpunktsabstand der Monomere von $2.990 \pm 0.001 \text{ \AA}$ berechnet. Dieser Abstand ist um 0.028 \AA kleiner als derjenige, der aus Elektronenbeugungs-Experimenten berichtet wurde [ABM69] und stellt den Hauptunterschied zwischen den Struktur-Ergebnissen des fs DFWM- und des Elektronenbeugungs-Experiments dar. Im Gegensatz zur Ameisensäure zeigt Essigsäure intensive Rekurrenzen der dimeren Spezies, sogar für die fs DFWM Spektren bei Raumtemperatur. Dieses wird durch die unterschiedliche Symmetrie des Trägheitstensors für beide Systeme erklärt (das fs DFWM Signal ist üblicherweise stärker je symmetrischer die entsprechende Spezies ist). Aufgrund der symmetrischen Natur des Essigsäure-Dimers, konnte allerdings nur die Summe der Rotationskonstanten ($B+C$) extrahiert werden. Schließlich wurde eine mögliche Änderung der geometrischen Parameter der Monomere aufgrund der Dimerisierung für beide Systeme (Ameisen- und Essigsäure) abgeschätzt.

In dieser Arbeit wurde der Einsatz eines *heat-pipe*-Ofens getestet, der die Überwindung eines Nachteils der fs DFWM Methode, nämlich die quadratische Abhängigkeit der Signalintensität von der Teilchenzahldichte, erlaubt. Zwei-Ring-Moleküle (Cyclohexylbenzol CHB, para-Cyclohexylanilin pCHA, Nicotin) mit niedrigen Dampfdrücken (<0.1 mbar bei Raumtemperatur) wurden untersucht. Aus der Analyse der experimentellen Daten und unter Berücksichtigung der Ergebnisse von *ab initio* Berechnungen wurde eine nahezu senkrechte Konformation des aromatischen Rings gegenüber dem Cyclohexyl-Rest für pCHA und CHB abgeleitet. Für CHB wurde eine Verkleinerung der Rotationskonstante B im elektronisch angeregten Zustand S_1 ermittelt und durch die Strukturberechnungen auf eine Vergößerung des aromatischen Ringes zurückgeführt. Für Nicotin konnten leider keine Strukturinformationen erhalten werden da das fs DFWM-Signal zu schwach war. Da aber die fs DFWM Spektroskopie zur Konformations-Analyse von Molekülen *im thermischen Gleichgewicht* einsetzbar ist, ergeben sich hierdurch mögliche neue interessante Anwendungen für diese Methodik, insbesondere im Hinblick auf die Untersuchung der konformationellen Präferenz biomolekularer Systeme.

Im Allgemeinen zeigen die Ergebnisse dieser Arbeit, dass die fs DFWM Methodik, als spezifische Realisierung von RCS, ein wichtiges spektroskopisches Werkzeug für die strukturelle Analyse isolierter molekularer Systeme darstellt, insbesondere für Spezies auf die die Mikrowellen-Spektroskopie nicht anwendbar ist. Es ergeben sich Spektren mit exzellentem Signal-zu-Rausch-Verhältnis, sogar unter den Bedingungen niedriger Teilchenzahldichte wie sie in einer Überschalldüsenstrahlexpansion vorliegen. Die Methodik stellt einen innovativen Zugang zur Rotations-Raman-Spektroskopie für große Moleküle dar und ist in einem breiten Temperatur- und Druck-Bereich einsetzbar. Durch den Einsatz von Femtosekunden-Laserpulsen (10^{-15} s), im Gegensatz zu Pikosekunden-Pulsen (10^{-12} s) für herkömmliche RCS-Messungen, ergibt sich eine erhöhte Zeitauflösung und es konnte eine Steigerung der Genauigkeit der Rotationskonstanten von mehr als einer Größenordnung erreicht werden. Molekulare Systeme ohne permanentes Dipolmoment oder Chromophor können mit hoher Genauigkeit untersucht werden und molekulare Benchmark-Systeme für die elektronische Struktur-Theorie werden dadurch bereitgestellt.

Es konnte in dieser Arbeit gezeigt werden, dass die Analyse molekularer Aggregate mittels fs DFWM möglich ist, allerdings ist das Potential durch die ungünstige Skalierung mit der

Teilchenzahldichte, die für Düsenstrahlexperimente von besonderer Wichtigkeit ist, stark eingeschränkt. Hier könnte sich für die Zukunft die Anwendung von nah-resonantem oder resonantem Vierwellenmischen mit veränderter, d. h. kürzerer Wellenlänge, als sehr hilfreich erweisen. Eine Steigerung der Empfindlichkeit um mehr als eine Größenordnung sollte möglich sein.

Durch die Einführung des *heat-pipe*-Ofens für fs DFWM Experimente ist die Untersuchung schwerflüchtiger Proben unter Gleichgewichtsbedingungen ermöglicht worden. Es konnten damit die ersten Experimente zur Analyse verschiedener Konformere des Pyrrolidins in der Gasphase durchgeführt werden [MaR04]. Diese Methodik bietet noch weitere Perspektiven für die Untersuchung großer Moleküle durch Kombination mit neuen, nicht-thermischen Quellen für schwerflüchtige Moleküle, wie Laserdesorption [CTL89], Laserablation [MHL83], Elektrospray [FMM90], oder LILBID (*laser induced liquid beam desorption* [KAB96, Sob00]).

In einer ganz neuen Anwendung der fs DFWM Technik wurde der Einfluß intensiver Laserfelder auf Moleküle in der Gasphase studiert und es wurden Effekte von der aktiven Ausrichtung [PPB03] über die feldinduzierte Verzerrung molekularer Geometrien bis zur Feldionisation [CSD03] nachgewiesen. Insbesondere die lasergesteuerte aktive Ausrichtung von Molekülen bietet neben der grundlegenden Untersuchung dieses Phänomens, die faszinierende Möglichkeit der gezielten Manipulation eines molekularen Ensembles mit extern kontrollierbaren, makroskopischen Eigenschaften, wie z. B. dem Brechungsindex etc. Im Hinblick auf eine weitere Entwicklung der fs DFWM Spektroskopie sollte für die Analyse von komplexeren Molekülen untersucht werden welchen Einfluß niederfrequente Moden (van der Waals Schwingungen, interne Rotationen) auf die Rotationskohärenz bzw. die fs DFWM Spektren haben. Erste phänomenologische Ansätze dazu traten bereits im Rahmen dieser Arbeit bei der Untersuchung der Essigsäure zutage.

Es lässt sich schließlich festhalten, daß Femtosekunden entartetes Vierwellenmischen als experimentelle Realisierung von Rotationskohärenz-Spektroskopie eine innovative, sich entwickelnde, leistungsstarke Methode für die strukturelle Untersuchung isolierter molekularer Spezies ist, welche mit den klassischen frequenz-basierten Methoden nicht oder nur schwer studiert werden können [FeZ95a, Dan01, Rie02].

Appendix: *Abbreviations and Symbols*

Acetic acid		CH ₃ COOH
Benzene		C ₆ H ₆
Benzene-d₆	perdeutero-benzene	C ₆ D ₆
CHB	Cyclohexylbenzene	C ₆ H ₅ -C ₆ H ₁₁
Cyclohexane		C ₆ H ₁₂
Formic acid		HCOOH
Nicotine	3-(N-methyl-2-pyrrolidinyl)pyridine	C ₅ H ₄ -C ₄ H ₇ N-CH ₃
<i>p</i>CHA	<i>para</i> -Cyclohexylaniline	H ₂ N-C ₆ H ₄ -C ₆ H ₁₁
<i>p</i>DFB	<i>para</i> -Difluorobenzene	C ₆ H ₄ -F ₂
Pyridine		C ₅ H ₅ N
CARS	Coherent anti-Stokes Raman Scattering	
CBS	Complete Basis Set	
CD	Centrifugal Distortion	
CPA	Chirped Pulse Amplification	
DFT	Density Functional Theory	
fs DFWM	femtosecond Degenerate Four-Wave Mixing	
FWHM	Full Width Half Maximum	
IVR	Intramolecular Vibrational Redistribution	
MP2	second order Møller-Plesset	
PPI	Pump-Probe Ionization	
PT	Polarizability Tensor	
QBs	Quantum Beats	
RCS	Rotational Coherence Spectroscopy	
RIPS	Raman-Induced Polarization Spectroscopy	
RRs	Rotational Recurrences	
TCSPC	Time-Correlated Single-Photon counting	
TM	Transition Dipole Moment	
TRFD	Time-Resolved Fluorescence Depletion	
TRID	Time-Resolved Ionization Depletion	
TRPES	Time-Resolved Photoelectron Spectroscopy	
TRSEP	Time-Resolved Stimulated Emission Pumping	
TRSRFD	Time-Resolved Stimulated Raman-induced Fluorescence Depletion	

Bibliography

- [ABM69] A. Almenningen, O. Bastiansen, and T. Motzfeld, *Acta Chem. Scand.*, **23**, 1969, 2848.
- [ACEII] J. F. Stanton, J. Gauss, J. D. Watts, M. Nooijen, N. Oliphant, S. A. Perera, P. G. Szalay, W. J. Lauderdale, S. R. Gwaltney, S. Beck, A. Balkova, D. E. Bernholdt, K.-K. Baeck, P. Tozyczko, H. Sekino, C. Huber, R. J. Bartlett, **ACES II**; Quantum Theory Project, University of Florida: Gainesville, FL. Integral packages included are VMOL (J. Almlof, P. R. Taylor); VPROPS (P. R. Taylor); and ABACUS (T. Helgaker, H. J. Aa. Jensen, P. Jorgensen, J. Olsen, P. R. Taylor).
- [AIK63] N. V. Alekseev, A. I. Kitaigorodskii, *Zh. Strukt. Khim.*, **4**, 1963, 163.
- [ÅRT00] P. -O. Åstrand, K. Ruud, P. R. Taylor, *J. Chem. Phys.*, **112**, 2000, 2655.
- [Atk94] P. W. Atkins, *Physical Chemistry*, Oxford University Press, New York, 1994.
- [Bar55] L. S. Bartell, *J. Chem. Phys.*, **23**, 1955, 1219.
- [Bar89] R. J. Bartlett, *J. Phys. Chem.*, **93**, 1989, 1697.
- [BaZ89] J. S. Baskin and A. H. Zewail, *J. Phys. Chem.*, **93**, 1989, 5701.
- [BBH95] K. B. Borisenko, C. W. Bock, I. Hargittai, *J. Mol. Structure (Theochem)*, **332**, 1995, 161.
- [BCE86] K. W. Butz, D. L. Catlett, Jr., G. E. Ewing, D. Krajnovich, C. S. Parmenter, *J. Phys. Chem.*, **90**, 1986, 3533.
- [Ber82] R. B. Bernstein, *Chemical Dynamics via Molecular Beam and Laser Techniques*, Oxford University Press: New York, 1982.
- [Ber95] P. F. Bernath, *Spectra of Atoms and Molecules*, Oxford University Press, New York, 1995.
- [BFS73] O. Bastiansen, L. Fernholt, H. M. Seip, H. Kambara, H. Kuchitsu, *J. Mol. Struct.*, **18**, 1973, 163.

BIBLIOGRAPHY

- [BFZ86] J. S. Baskin, P. M. Felker, A. H. Zewail, *J. Chem. Phys.* 84, **1986**, 4708.
- [BFZ87] J. S. Baskin, P. M. Felker and A. H. Zewail, *J. Chem. Phys.*, 86, **1987**, 2483.
- [BGF99] P. Benharash, M. J. Gleason, P. M. Felker, *J. Phys. Chem. A*, 103, **1999**, 1442.
- [BGJ01] K. L. Bak, J. Gauss, P. Jørgensen, J. Olsen, T. Helgaker, J. F. Stanton, *J. Chem. Phys.*, 114, **2001**, 6548.
- [BiH92] H. Bitto, J. R. Huber, *Acc. Chem. Res.*, 25, **1992**, 65.
- [BJK95] E. Bialkowska-Jaworska, M. Jaworski, Z. Kisiel, *J. Mol. Struct.*, 350, **1995**, 247.
- [BoS65] J. Bohdansky and H. E. J. Schins, *J. Appl. Phys.*, 36, **1965**, 3683.
- [BoS67] J. Bohdansky and H. E. J. Schins, *J. Phys. C*, 71, **1967**, 215.
- [BZD99] E. J. Brown, Q. Zhang, M. Dantus, *J. Chem. Phys.* 110, **1999**, 5772.
- [CAR88] D. A. Clabo, W. D. Allen, R. B. Remington, Y. Yamaguchi, H. F. Schaefer, *Chem. Phys.*, 123, **1988**, 187.
- [CCH90] T. C. Corcoran, L. L. Connell, G.V.Hartland, P. W. Joireman, R. A Hertz, P. M. Felker, *Chem. Phys. Lett.* 170, **1990**, 139.
- [CCJ90] L. L. Connell, T. C. Corcoran, P. W. Joireman, P. M. Felker, *J. Phys. Chem.*, 94, **1990**, 1229.
- [CDS93] M. Cho, M. Du, N. F. Scherer, G. R. Fleming and S. Mukamel. *J. Chem. Phys.* 94, **1993**, 2410.
- [CGM81] J. Chaiken, M. Gurnick, J. D. McDonald, *J. Chem. Phys.*, 74, **1981**, 106.
- [CHK69] J. Christoffersen, J. M. Hollas, G. H. Kirby, *Mol. Phys.*, 19, **1969**, 441.
- [CHK70] T. Cvitaš, J.M. Hollas, G.H. Kirby, *Mol. Phys.*, 19, **1970**, 305.
- [CHM86] J. Chao, K. R. Hall, K. N. Marsh, and R. C. Wilhoit, *J. Phys. Chem.*, Ref. Data 15, **1986**, 1369.
- [Choch] We are grateful to Jana Chocholoušová for supporting us with *ab-initio* calculations.
- [ChZ78] J. Chao, and B. J. Zwolinski, *J. Phys. Chem.*, Ref. Data7, **1978**, 363.

BIBLIOGRAPHY

- [CKS89] M. J. Côté, J. F. Kauffman, P. G. Smith, J. D. McDonald, *J. Chem. Phys.*, 90, **1989**, 2865.
- [COJ92] L. L. Connell, S. M. Ohline, P. W. Joireman, T. C. Corcoran, P. M. Felker, *J. Chem. Phys.*, 96, **1992**, 2585.
- [CPC90] R. R. B. Correia, G. Pichler, S. L. Cunha, P. Hering, *Chem. Phys. Lett.*, 175, 1990, 354.
- [CPD00] M. Comstock, I. Pastirk, M. Dantus, in *Ultrafast Phenomena XII*, Springer Verlag, Berlin, **2000**.
- [CSC79] W. Caminati, F. Scappini, G. Corbelli, *J. Mol. Spectrosc.*, 75, **1979**, 327.
- [CSD03] M. Comstock, V. Senekerimyan, M. Dantus, *J. Phys. Chem. A*, 119, **2003**, 6546.
- [CTL89] J. R. Cable, M. J. Tubergen, D. H. Levy, *J. Am. Chem. Soc.*, 111, **1989**, 9032.
- [CVH02] J. Chocholoušová, J. Vacek, and P. Hobza, *Phys. Chem. Chem. Phys.*, 4, **2002**; 2119.
- [CVH03] J. Chocholoušová, J. Vacek, and P. Hobza, *J. Phys. Chem.*, 107, **2003**, 3086.
- [DaH63] M. Davis, M. Hassel, *Acta Chem. Scand.*, 17, **1963**, 1181.
- [DAL01] T. Helgaker, H. J. Aa. Jensen, P. Jørgensen, J. Olsen, K. Ruud, H. Ågren, A. A. Auer, K. L. Bak, V. Bakken, O. Christiansen, S. Coriani, P. Dahle, E. K. Dalskov, T. Enevoldsen, B. Fernandez, C. Hättig, K. Hald, A. Halkier, H. Heiberg, H. Hettema, D. Jonsson, S. Kirpekar, R. Kobayashi, H. Koch, K. V. Mikkelsen, P. Norman, M. J. Packer, T. B. Pedersen, T. A. Ruden, A. Sanchez, T. Saue, S. P. A. Sauer, B. Schimmelpfennig, K. O. Sylvester-Hvid, P. R. Taylor, O. Vahtras, **DALTON**, an electronic structure program, release 1.2; **2001**; <http://www.kjemi.uio.no/software/dalton/dalton.html>.
- [Dan01] M. Dantus, *Ann. Rev. Phys. Chem.*, 52, **2001**, 639.
- [DBG90] J. Dommen, Th. Brupbacher, G. Grassi, A. Bauder, *J. Am. Chem. Soc.*, 112, **1990**, 953.
- [Dem96] W. Demtröder, *Laser Spectroscopy*, 2nd ed., Springer Verlag, Berlin, Heidelberg, **1996**.

BIBLIOGRAPHY

- [Der71] J. L. Derissen, *J. Mol. Structure*, 7, **1971**, 67.
- [DJP91] J. L. Domenech, M-L. Juntilla, A. S. Pine, *J. Mol. Spectrosc.*, 149, **1991**, 391.
- [DoH92] A. Domenicano, I. Hargittai, Eds., *Accurate Molecular Structures. Their Determination and Importance*, International Union of Crystallography and Oxford University Press: Oxford, **1992**.
- [DPP93] R. Danielius, A. Piskarskas, A. Persson, and S. Svanberg, *Lith. J. Phys.* 33, **1993**, 305.
- [DPT96] R. Danielius, A. Piskarskas, P. Di Trapani, A. Andreoni, C. Solcia, and P. Foggi, *Appl. Opt.*, 35, **1996**, 5336.
- [DSH82] A. Domenicano, G. Schultz, I. Hargittai, *J. Mol. Struct. (Theochem)*, 78, **1982**, 97.
- [EGP86] H. J. Eichler, P. Gunter, and D. W. Pohl, *Laser-Induced Dynamic Gratings*, Springer, Berlin, **1986**.
- [EiD83] B. P. van Eijck, and F. B. van Duijneveldt, *J. Mol. Spectrosc.*, 102, **1983**, 273.
- [EKS76] J. D. Ewbank, G. Kirsch, L. Schäfer, *J. Mol. Struct.*, 31, **1976**, 39.
- [EID00] D. E. Elmore, D. A. Dougherty, *J. Org. Chem.*, 65, **2000**, 742.
- [EOS81] B. P. van Eijck, J. van Opheusden, M. M. M. van Schaik and E. van Zoeren, *J. Mol. Spectrosc.*, 86, **1981**, 465.
- [ESL03] C. Emmeluth, M. A. Suhm, D. Luckhaus, *J. Chem. Phys.*, 118, **2003**, 2242.
- [Fay82] M. D. Fayer, *Annu. Rev. Phys. Chem.*, 33, **1982**, 63.
- [FBG00] H. M. Frey, P. Beaud, T. Gerber, B. Mischler, P.P. Radi and A.P. Tzannis, *J. Raman Spectrosc.*, 31, **2000**, 71.
- [FBG99] H. M. Frey, P. Beaud, T. Gerber, B. Mischler, P. P. Radi, A. P. Tzannis, *Appl. Phys. B*, 68, **1999**, 735.
- [FBZ86] P. M. Felker, J. S. Baskin, A. H. Zewail, *J. Phys. Chem.*, 90, **1986**, 724.
- [FCB80] D. J. Frurip, L. A. Curtiss, M. Blander, *J. Am. Chem. Soc.*, 102, **1980**, 2610.

BIBLIOGRAPHY

- [FeD01] D. Feller, D. A. Dixon, *J. Chem. Phys.*, 115, **2001**, 3484.
- [Fel92] P. M. Felker, *J. Phys. Chem.*, 96, **1992**, 7844.
- [FeZ87] P. M. Felker and A. H. Zewail, *J. Chem. Phys.*, 86, **1987**, 2460.
- [FeZ88] P. M. Felker and A. H. Zewail, *Adv. Chem. Phys.*, 70, **1988**, 265.
- [FeZ95a] P. M. Felker and A. H. Zewail, in *Femtochemistry*, edited by J. Manz and L. Wöste (Eds.), VCH, Weinheim, **1995**, Chap. 5, Vol. I.
- [FeZ95b,c] P. M. Felker and A. H. Zewail, in *Jet spectroscopy and Dynamics*, J.M. Hollas, D. Phillips (Eds.), Blackie Academic & Professional, New York, **1995**, (b) Chap. 6; (c) Chap. 7.
- [FML02] H. M. Frey, A. Müller and S. Leutwyler, *J. Raman Spectrosc.*, 33, 2002, 855.
- [FMM90] J. B. Fenn, M. Mann, C. K. Meng, S. F. Wong, C. M. Whitehouse, *Mass Spectr. Rev.*, 9, **1990**, 37.
- [FSZ01] G. M. Florio, E. L. Sibert III, T. S. Zwier, *Faraday Discuss.*, 118, **2001**, 315.
- [FZM03] G. M. Florio, T. S. Zwier, E. M. Myshakin, K. D. Jordan, E. L. Sibert III, *J. Chem. Phys.*, 118, **2003**, 1735.
- [GaS00] J. Gauss, J. F. Stanton, *J. Phys. Chem. A*, 104, **2000**, 2865.
- [Gau98] M. J. Frisch, G. W. Trucks, H. B. Schlegel, G. E. Scuseria, M. A. Robb, J. R. Cheeseman, V. G. Zakrzewski, J. A. Montgomery, R. E. Stratmann, J. C. Burant, S. Dapprich, J. M. Millam, R. E. Daniels, K. N. Kudin, M. C. Strain, O. Farkas, J. Tomasi, V. Barone, M. Cossi, R. Cammi, B. Mennucci, C. Pomelli, C. Adamo, S. Clifford, J. Ochterski, G. A. Petersson, P. Y. Ayala, Q. Cui, K. Morokuma, P. Salvador, J. J. Dannenberg, D. K. Malick, A. D. Rabuck, K. Raghavachari, J. B. Foresman, J. Cioslowski, J. V. Ortiz, A. G. Baboul, B. B. Stefanov, G. Liu, A. Liashenko, P. Piskorz, I. Komaromi, R. Gomperts, R. L. Martin, D. J. Fox, T. Keith, M. A. Al-Laham, C. Y. Peng, A. Nanayakkara, M. Challacombe, P. M. W. Gill, B. Johnson, W. Chen, M. W. Wong, J. L. Andres, C. Gonzalez, M. M. Head-Gordon, E. S. Replogle, J. A. Pople, **Gaussian 98** (Revision A.11); Gaussian, Inc.: Pittsburgh, PA, **2001**.
- [GBM71] H. J. Geise, H. R. Buys, F. C. Mijlhoff, *J. Mol. Struct.*, 9, **1971**, 447.

BIBLIOGRAPHY

- [GCS00] J. Gauss, D. Cremer, J. F. Stanton, *J. Phys. Chem. A*, 104, **2000**, 1319.
- [GHS00] M. Gantenberg, M. Halupka, and W. Sander, *Chem. Eur. J.* **6**, 1865 (2000).
- [GiS74] R. Gilbert, C. Sandorfy, *Chem. Phys. Lett.*, 27, **1974**, 457.
- [GoC84] W. Gordy, R. L. Cook, *Microwave Molecular Spectra*, 3rd Ed., Wiley Interscience, New York, **1984**, pp. 684 ff.
- [GPO95] B. D. Gilbert, C. S. Parmenter, H.-K. Oh, *J. Phys. Chem.*, 99, **1995**, 2444.
- [GRD90] M. Gruebele, G. Roberts, M. Dantus, R. M. Bowman, A. H. Zewail, *Chem. Phys. Lett.*, 166, **1990**, 459.
- [GRM03] M. F. Gelin, C. Riehn, V.V. Matylitsky, and B. Brutschy, *Chem. Phys.*, 290, **2003**, 307.
- [GrZ93] M. Gruebele, A. H. Zewail, *J. Chem. Phys.*, 98, **1993**, 883.
- [GTB00] M. F. Gelin, V. A. Tolkachev, A. P. Blokhin, *Chem. Phys.*, 255, **2000**, 111.
- [HaC95] C. C. Hayden and D. W. Chandler, *J. Chem. Phys.*, 103, **1995**, 10465.
- [Har76] S. Haroche, *High Resolution Laser spectroscopy*, Springer, New York, **1976**.
- [HCF91] G. V. Hartland, L.L. Connell, P. M. Felker, *J. Chem. Phys.* 94 (1991) 7649.
- [Her45] G. Herzberg, *Molecular Spectra and Molecular Structure*, Van Nostrand Reinhold, New York, 1945; Vol. I-III
- [HES81] E. Hirota, Y. Endo, S. Saito, J. L. Duncan, *J. Mol. Spectrosc.*, 89, **1981**, 285.
- [HGL75] J. P. Heritage, T. K. Gustafson, C. H. Lin, *Phys. Rev. Lett.* 34, **1975**, 1299
- [HKK97] T. Helgaker, W. Klopper, H. Koch, J. Noga, *J. Chem. Phys.*, 106, **1997**, 9639.
- [HNN96] R. M. Helm, R. Neuhauser and H. J. Neusser, *Chem. Phys. Lett.*, 249, **1996**, 365.
- [Hoc76] W. H. Hocking, *Z. Naturforsch. A*, 31, **1976**, 1113.

BIBLIOGRAPHY

- [Hol98] John Michael Hollas, *High Resolution Spectroscopy*, John Wiley & Sons, Baffins Lane, Chichester, **1998**
- [HoW78] A. B. Hollinger and H. L. Welsh, *Can. J. Phys.*, 56, **1978**, 974.
- [HSE01] T. Häber, U. Schmitt, C. Emmeluth, M. A. Suhm, *Faraday Discuss.*, 118, **2001**, 331.
- [ItN02] F. Ito, T. Nakanaga, *Chem. Phys.*, 277, **2002**, 163.
- [JÅO02] L. Jensen, P. O. Åstrand, A. Osted, J. Kongsted and K. V. Mikkelsen, *J. Chem. Phys.* 16, **2002**; 4001.
- [JCO92] P. W. Joireman, L. L. Connell, S. M. Ohline, P. M. Felker, *J. Chem. Phys.*, 96, **1992**, 4118.
- [JDF91] M-L. Juntilla, J. L. Domenech, G. T. Fraser, A. S. Pine, *J. Mol. Spectrosc.*, 147, **1991**, 513.
- [JMR03] W. Jarzeba, V. V. Matylitsky, C. Riehn, B. Brutschy, *Chem. Phys. Lett.*, 368, **2003**, 680.
- [JMW02] W. Jarzeba, V. V. Matylitsky, A. Weichert, C. Riehn, *Phys. Chem. Chem. Phys.*, 4, **2002**, 451.
- [JoL75] J. W. Johns, D. W. Lepard, *J. Mol. Spectrosc.*, 55, **1975**, 374.
- [KaB44] J. Karle, L. O. Broadway, *J. Am. Chem. Soc.* **66**, 574 (1944).
- [KAB96] W. Kleinekofort, J. Avdiev, B. Brutschy, *Int. J. Mass. Spectr. Ion Proc.*, 152, **1996**, 135.
- [KaG51] A. Kantrowitz, J. Grey, *J. Rev. Sci. Instrum.*, 22, **1951**, 328.
- [KaM85] F. Kajzar and J. Messier, *Phys. Rev. A*, 32, **1985**, 2352.
- [KCS89] J. F. Kauffman, M. J. Côté, P. G. Smith, J. D. McDonald, *J. Chem. Phys.* 90, **1989**, 2874.
- [KMC92] K. S. Kim, B. J. Mhin, U.-S. Choi, K. Lee, *J. Chem. Phys.*, 97, **1992**, 6649.
- [KnK88] A. E. W. Knight, S. H. Kable, *J. Chem. Phys.*, 89, **1988**, 7139.
- [LeB98] G. Lembach, B. Brutschy, *J. Phys. Chem. A*, 102, **1998**, 6068.

BIBLIOGRAPHY

- [LFM00] B. Lavorel, O. Faucher, M. Morgen and R. Chauv, *J. Raman Spectrosc.*, 31, **2000**, 77.
- [LHG71] C. H. Lin, J. P. Heritage and T. K. Gustafson, *Appl. Phys. Letters*, 19, **1971**, 397.
- [LMB94] M. K. Leong, V. S. Matryukov, J. E. Boggs, *J. Phys. Chem. A*, 98, **1994**, 6961.
- [LMF01] T. Lang, M. Motzkus, H. M. Frey, P. Beaud, *J. Chem. Phys.*, 115, **2001**, 5418.
- [MaH02] F. Madeja, and M. Havenith, *J. Chem. Phys.*, 117, **2002**, 7162.
- [MaR04] V. V. Matylitsky, C. Riehn, 103. Bunsentagung, **2004**, Conference proceedings, p. C121.
- [Mar87] Y. Marechal, *J. Chem. Phys.*, 87, **1987**, 6344.
- [MaS69] D. M. Mathews, B. N. Sheets, *J. Chem. Soc. A*, **1969**, 2203.
- [MBH83] G. R. Meredith, B. Buchalter, and C. Hanzlik, *J. Chem. Phys.*, 78, **1983**, 1533.
- [MGR04] V. V. Matylitsky, M. F. Gelin, C. Riehn, and B. Brutschy, *Proceedings of the International Conference Femtochemistry VI*, (to be published in **2004**).
- [MHL83] M. D. Morse, J. B. Hopkins, P. R. Langridge-Smith, R. E. Smalley, *J. Chem. Phys.*, 79, **1983**, 5316.
- [MJR02] V. V. Matylitsky, W. Jarzeba, C. Riehn, B. Brutschy, *J. Raman Spectrosc.*, 33, **2002**, 877.
- [MøP34] C. Møller, M. S. Plesset, *Phys. Rev.*, 46, **1934**, 618.
- [MPH93] M. Morgen, W. Price, L. Hunziker, P. Ludowise, M. Blackwell, Y. Chen, *Chem. Phys. Lett.*, 209, **1993**, 1.
- [MPK98] M. Motzkus, G. Pichler, K. L. Kompa, P. Hering, *J. Chem. Phys.*, 108, **1998**, 9291.
- [MPL95] M. Morgen, W. Price, P. Ludowise and Y. Chen, *J. Chem. Phys.* 102, **1995**, 8780.

BIBLIOGRAPHY

- [MPZ96] M. Motzkus, S. Pedersen, and A. H. Zewail, *J. Phys. Chem.* 100, **1996**, 5620
- [MQS77] F. Mata, M. J. Quintana, G. O. Sørensen, *J. Mol. Struct.*, 42, **1977**, 1.
- [MRG03] V. V. Matylitsky, C. Riehn, M. F. Gelin, B. Brutschy, *J. Chem. Phys.*, 119, **2003**, 10553.
- [Muk95] S. Mukamel, *Principles of Nonlinear Optical Spectroscopy*, Oxford, New York, **1995**.
- [MyH86] A. B. Myers and R. M. Hochstrasser, *IEEE J. Quantum Electron.*, 22, **1986**, 1482.
- [NIST] NIST Mass Spec Data Center, S.E. Stein, director, "Mass Spectra" in NIST Chemistry WebBook, NIST Standard Reference Database Number 69, Eds. P.J. Linstrom and W.G. Mallard, **March 2003**, National Institute of Standards and Technology, Gaithersburg MD, 20899 (<http://webbook.nist.gov>).
- [OMH99] M. Okruss, R. Müller and A. Hese, *J. Mol. Spectrosc.*, 193, **1999**, 293 and references therein.
- [OPS88] H.-K. Oh, C. S. Parmenter, M.-S. Su, *Ber. Bunsenges., Phys. Chem.*, 92, **1988**, 253.
- [ORF93] S. M. Ohline, J. Romascan, P. M. Felker, *Chem. Phys. Lett.*, 207, **1993**, 563.
- [PaB34] L. Pauling, L. O. Brockway, *Proc. Nat. Acad. Sci., U.S.A.*, 20, **1934**, 336.
- [PaG94] W. Paul, D. Gerlich, IXth International Symposium on Atomic, molecular cluster, ion and surface physics (SASP), **1994**, Conference proceedings, p.197.
- [PaT68] H. Pauly, J. P. Toennies, *Methods Exp. Phys.*, 7A, **1968**, 237.
- [PCC92] G. Pichler, R. R. B. Correia, S. L. Cunha, K. L. Kompa, P. Hering, *Opt. Commun.*, 92, **1992**, 346.
- [PJO02] F. Pawlowski, P. Jørgensen, J. Olsen, F. Hegelund, T. Helgaker, J. Gauss, K. L. Bak, J. F. Stanton, *J. Chem. Phys.*, 116, **2002**, 6482.
- [PKB00] D. Priem, T.-K. Ha, and A. Bauder, *J. Chem. Phys.*, 113, **2000**, 169.
- [PLB83] P. Pulay, J.-G. Lee, J. E. Boggs, *J. Chem. Phys.*, 79, **1983**, 3382.

BIBLIOGRAPHY

- [PIT33] Placzek G and Teller E. *Z. Physik*, 81, **1933**, 209.
- [Pol57] S. R. Polo, *Can. J. Phys.*, 35, **1957**, 880.
- [PPB03] E. Péronne, M. D. Poulsen, C. Z. Bisgaard, H. Stapelfeldt, T. Seideman, *Phys. Rev. Lett.*, 91, **2003**, 043003.
- [Pra98] D. W. Pratt, *Annu. Rev. Phys. Chem.*, 49, **1998**, 481.
- [PVC89] J. Pliva, A. Valentin, J. Chazelas, L. Henry., *J. Mol. Spectrosc.*, 134, **1989**, 220.
- [PWD94] K. A. Petersen, D. E. Woon, T. H. Dunning, *J. Chem. Phys.*, 100, **1994**, 7410.
- [PWW73] R. A. Peters, W. J. Walker, A. Weber, *J. Raman Spectrosc.*, 1, **1973**, 159.
- [RÅT00] K. Ruud, P.-O. Åstrand, P. R. Taylor, *J. Chem. Phys.*, 112, **2000**, 2668.
- [RDW00] C. Riehn, A. Degen, A. Weichert, M. Bolte, E. Egert, B. Brutschy, P. Tarakeshwar, K. S. Kim, *J. Phys. Chem. A*, 104, **2000**, 11593.
- [Rie02] C. Riehn, *Chem. Phys.*, 283, **2002**, 297.
- [RMG03] C. Riehn, V. V. Matylitsky and M. F. Gelin, *J. Raman Spectrosc.*, 34, **2003**, 1045.
- [RMJ03] C. Riehn, V. V. Matylitsky, W. Jarzeba, B. Brutschy, P. Tarakeshwar, K. S. Kim, *J. Am. Chem. Soc.*, 125, **2003**, 16455.
- [RMO00] K. Remmers, W. L. Meerts, I. Ozier, *J. Chem. Phys.*, 112, **2000**, 10890.
- [RSK98] O. Rubner, M. Schmitt, G. Knopp, A. Materny, W. Kiefer and V. Engel, *J. Phys. Chem. A*, 102, **1998**, 9734.
- [RTP89] K. Raghavachari, G. W. Trucks, J. A. Pople, M. Head-Gordon, *Chem. Phys. Lett.*, 157, **1989**, 479.
- [RWB00] C. Riehn, A. Weichert, B. Brutschy, *Phys. Chem. Chem. Phys.*, 2, **2000**, 1873.
- [RWB01] C. Riehn, A. Weichert and B. Brutschy, *J. Phys. Chem. A*, 105, **2001**, 5618.
- [RWL00] C. Riehn, A. Weichert, U. Lommatzsch, M. Zimmermann, B. Brutschy, *J. Chem. Phys.*, 112, **2000**, 3650.

BIBLIOGRAPHY

- [Sal69] L. Salem, *Chem. Phys. Lett.*, 3, **1969**, 99.
- [Sch04] M. Schäfer, *Phys. Chem. Chem. Phys.*, 6, **2004**, 3271.
- [She84] Y. R. Shen, *The Principle of Nonlinear Optics*, Wiley, New York, **1984**.
- [SiS01] Sinnokrot, M. O.; Sherrill, C. D. *J. Chem. Phys.*, 115, **2001**, 2439.
- [SKM97a] M. Schmitt, G. Knopp, A. Materny, W. Kiefer, *Chem. Phys. Lett.*, 270, **1997**, 9.
- [SKM97b] M. Schmitt, G. Knopp, A. Materny, W. Kiefer, *Chem. Phys. Lett.*, 280, **1997**, 339.
- [SKR87] N. F. Scherer, L. R. Khundkar, T. S. Rose, A. H. Zewail, *J. Phys. Chem.*, 91, **1987**, 6478.
- [SmM90] P. G. Smith, J. D. McDonald, *J. Chem. Phys.*, 92, **1990**, 3991.
- [SNN94a] R. Sussmann, R. Neuhauser, H. J. Neusser, *Can. J. Phys.*, 72, **1994**, 1179.
- [SNN94b] R. Sussmann, R. Neuhauser, H. J. Neusser, *Chem. Phys. Lett.*, 229, **1994**, 13.
- [Sob00] F. Sobott, *Charakterisierung und Anwendung der LILBID Laserdesorptions-Massenspektrometrie*, Dissertation, Frankfurt/M., **2000**, www.dissertation.de.
- [SOP91] M.-C. Su, H.-K. Oh, C. S. Parmenter, *Chem. Phys.*, 156, **1991**, 261.
- [Sør67] G. O. Sørensen, *J. Mol. Spectrosc.*, 22, **1967**, 325.
- [SSS01] K. W. Sattelmeyer, H. F. Schaefer, J. F. Stanton, *J. Chem. Phys.*, 114, **2001**, 9863.
- [Sto54] B. P. Stoicheff, *Can. J. Phys.*, 32, **1954**, 339.
- [STT93] P. G. Smith, T. Troxler, M. R. Topp, *J. Phys. Chem.*, 97, **1993**, 6983.
- [TFE02] T. Takeshima, R. Fukumoto, T. Egawa, S. Konaka, *J. Phys. Chem. A*, 106, **2002**, 8734.
- [Tri80] C. Trindle, *Isr. J. Chem.*, 19, **1980**, 47.
- [TuD93] L. Turi and J. J. Dannenberg, *J. Phys. Chem.*, 97, **1993**, 12197.
- [ViC69] C. R. Vidal, J. Cooper, *J. Appl. Phys.*, 40, **1969**, 3370.

BIBLIOGRAPHY

- [Vid96] C. R. Vidal, in *Experimental Methods in the Physical Sciences*, edited by F. B. Dunning and R. Hulet, Vol. 29B, Atomic, Molecular and Optical Physics, Atoms and Molecules, **1996**, Academic, New York. 67-83.
- [ViH71] C. R. Vidal, F. B. Haller, *Rev. Sci. Instrum.*, **42**, **1971**, 1779.
- [WDB87] E. Willemot, D. Dagnoise, and J. Bellet, *J. Mol. Spectrosc.*, **73**, **1987**, 96.
- [Web80] A. Weber, *J. Chem. Phys.*, **73**, **1980**, 3952.
- [Wei00] A. Weichert, *Pikosekunden-Laserpulse zur Strukturuntersuhung von Molekülen und molekularen Aggregaten: Rotationskohärenzspektroskopie*, Dissertation, Frankfurt/M., **2000**, www.dissertation.de.
- [Wib83] K. B. Wiberg, *J. Am. Chem. Soc.*, **105**, **1983**, 1227.
- [WiH94] A. Winkler, P. Hess, *J. Am. Chem. Soc.*, **116**, **1994**, 9223.
- [WMD88] G. Wlodarczak, L. Martinache, J. Demaison, B. P. Van Eijck, *J. Mol. Spectrosc.*, **127**, **1988**, 200.
- [Wol67] J. Wollrab, *Rotational Spectra and Molecular Structure*, Academic Press, New York, **1967**.
- [Woo78] R. G. Wooley, *J. Am. Chem. Soc.*, **100**, **1978**, 1073.
- [WRB00] A. Weichert, C. Riehn, B. Brutschy, *J. Chem. Phys.*, **113**, **2000**, 7830.
- [WRB01a] A. Weichert, C. Riehn, B. Brutschy, *J. Phys. Chem. A*, **105**, **2001**, 5679.
- [WRB01b] A. Weichert, C. Riehn, H.-D. Barth, G. Lembach, M. Zimmermann, B. Brutschy, D. Podenas, *Rev. Sci. Instrum.*, **72**, **2001**, 2697.
- [WRM02] A. Weichert, C. Riehn, V. V. Matylitsky, W. Jarzeba, B. Brutschy, *J. Mol. Struct.*, **612**, **2002**, 325.
- [Zar71] R. N. Zare, *Acc. Chem. Res.*, **4**, **1971**, 361.

Lebenslauf

Victor V. Matylitsky

Persönliche Angaben

Geburtsdatum und -ort: 03.07.1975 in Gresk, Weißrussland
Familienstand: verheiratet
Staatsangehörigkeit: weißrussisch

Ausbildung

Sep. 1982 – Jun. 1992 Schule in Gresk, Weißrussland

Sep. 1992 – Jun. 1997 Studium der Physik an der Belarus State University. Minsk, Weißrussland
Diplomarbeit in der Arbeitsgruppe von Prof. Dr. Komyak.
Thema: *“Development of synthesis methods for colour three-dimensional raster-type images”*

Nov. 1997 – Nov 2000 Junior-Wissenschaftler am Institut für Molekül und Atom Physik, Nationale Akademie der Wissenschaften von Weißrussland. Minsk, Weißrussland.

Dez. 2000 – Sep. 2004 Doktorand in der Arbeitsgruppe von Prof. Dr. Brutschy am Institut für Physikalische und Theoretische Chemie der Johann Wolfgang Goethe - Universität in Frankfurt am Main
Thema: *„Ultrafast non-linear time-resolved spectroscopy: Application to the structural study of polyatomic molecules and clusters“*

Lehrtätigkeit

ab April 2001 Mitarbeit in Übungsgruppen für Thermodynamik, Quantenmechanik, Spektroskopie und Mathematik.